UNIVERSITÀ DEGLI STUDI DI PAVIA
DOTTORATO DI RICERCA IN FISICA – XXI CICLO

Focusing on Dark Energy with Weak Gravitational Lensing

Giuseppe La Vacca

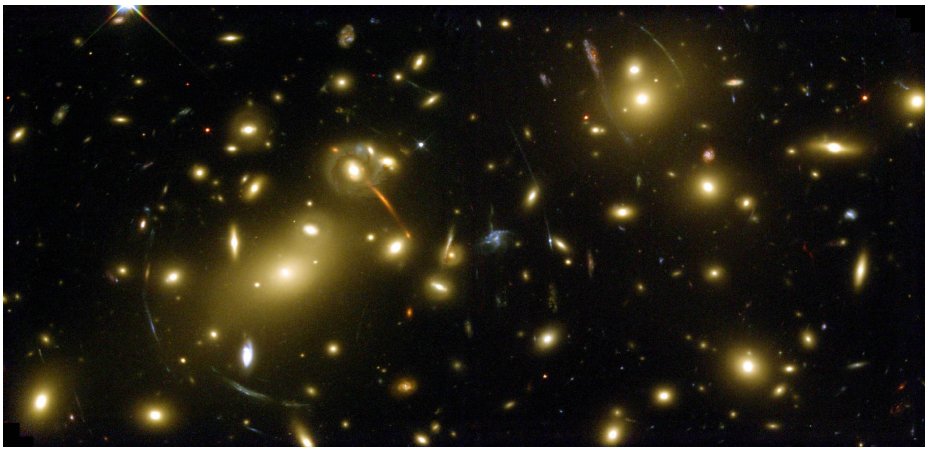

Supervisors: Prof. F. Miglietta
Prof. S. Bonometto

Tesi per il conseguimento del titolo

Università degli
Studi di Pavia

Dipartimento di Fisica
Nucleare e Teorica

Istituto Nazionale
di Fisica Nucleare

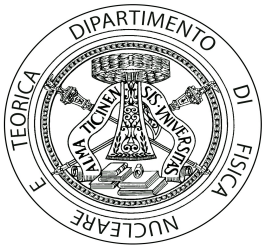

DOTTORATO DI RICERCA IN FISICA – XX CICLO

Focusing on Dark Energy with Weak Gravitational Lensing

dissertation submitted by

Giuseppe La Vacca

to obtain the degree of
DOTTORE DI RICERCA IN FISICA

Supervisors:	**Prof. F. Miglietta**
	Prof. S. Bonometto
Referee:	**Prof. M. Bruni**

Cover
NASA Hubble Space Telescope image of the galaxy cluster Abell *2218.*

Focusing on Dark Energy with Weak Gravitational Lensing
Giuseppe La Vacca
PhD thesis – University of Pavia
Printed in Pavia, Italy, November 2008
ISBN 978-88-95767-21-5

A Dominga

Sunt namque qui scire volunt eo fine tantum, ut sciant; et turpis curiositas est. Et sunt qui scire volunt, ut sciantur ipsi; et turpis vanitas est. [...] Et sunt item qui scire volunt ut scientiam suam vendant; verbi causa, pro pecunia, pro honoribus: et turpis quaestus est. Sed sunt quoque qui scire volunt, ut aedificent; et charitas est. Et item qui scire volunt, ut aedificenfur: et prudentia est.

Vi sono uomini che vogliono sapere per il solo gusto di sapere: è bassa curiosità. Altri cercano di conoscere per essere conosciuti: è pura vanità. Altri vogliono possedere la scienza per poterla rivendere e guadagnare denaro ed onori: il loro movente è meschino. Ma alcuni desiderano conoscere per edificare: e questo è carità. Altri per essere edificati: e questo è saggezza

Sancti Bernardi Abbatis Clarae-Vallensis (1090-1153)
SERMONES IN CANTICA CANTICORUM, Sermo XXXVI, 3
"Quod scientia litterarum sit bona ad instructionem, sed scientia propriae infirmitatis sit utilior ad salutem"

Preface

This thesis is devoted to the study of phaenomenology within the quest for Dark Energy (DE) nature. Nowadays, thanks to the accuracy with which cosmological parameters have been constrained, Cosmology has really turned into a high precision science. In spite of their accuracy, however, data are still far from really constraining DE nature, so that this keeps perhaps the main puzzle in today's cosmology.

Constraints on DE, until now, came from measurements of the Cosmic Microwave Background (CMB), from the Hubble diagram of SupernovæIa, from deep galaxy samples and from a few other observables, as Lyα clouds, galaxy cluster distribution, etc. Such measures will be certainly extended and improved in the next decade(s) leading to more stringent constraints. Even more effective are however expected to be future weak lensing (WL) data, namely in combination with the above *classical* observables, marking a real turning point to Cosmology.

This thesis wants to add a brick to the construction of this wide building, trying to study the impact of tomographic WL measurements on constraining dynamical and/or coupled DE models. Within this context, it will be outlined how massive neutrinos, added to the total cosmological energy balance, allow the consistency with present data of a higher DM–DE coupling.

This last issue outlines how tomographic WL observables will allow to shed new light over a problem as neutrino masses, so enriching the patterns through which large scale data influence microphysical issues.

The thesis is organized as follows. In Chapter 1 we introduce some elements of Cosmology with particular attention to its unsolved puzzles. In Chapter 2 we focus on the fundamental properties of dynamical DE models and on its phaenomenology. In Chapter 3, the simultaneous effect of a DM–DE coupling and massive neutrinos is taken into account, showing that cosmological limits on both neutrino masses and coupling are softened, by more than a factor 2. The subject of the Chapter 4 is the formulation of the gravitational lensing theory with a special attention to the weak lensing regime. In Chapter 5 we outline the main statistical and physical properties of CMB radiation. Chap-

ter 6 deals with constraints on cosmological parameters for dynamical and coupled DE models, using future weak lensing and CMB experiments. Finally, in Chapter 7 we draw our conclusions. Details on the methods used in the treatment of observables are discussed in Appendix A.

Part of the contents of this Thesis has already appeared in the following papers:

- G. La Vacca, S. A. Bonometto and L. P. L. Colombo, *Higher neutrino mass allowed if DM and DE are coupled*, submitted to New Astronomy [arXiv:0810.0127 [astro-ph]]
- L. Vergani, L. P. L. Colombo, G. La Vacca and S. A. Bonometto, *Dark Matter - Dark Energy coupling biasing parameter estimates from CMB data*, submitted to APJ [arXiv:0804.0285 [astro-ph]]
- G. La Vacca and L. P. L. Colombo, *Gravitational Lensing Constraints on Dynamical and Coupled Dark Energy*, JCAP 0804, 007 (2008) [arXiv:0803.1640 [astro-ph]].

Contents

Chapter 1

The Cosmological problem

1.1 Cosmology and Science: FRW metric and Friedmann equations

All cultures, since ever, made use of their most advanced techniques to face the challenge of cosmology, *i.e.* to formulate their views on the origin and fate of the world. Furthermore, since the emergence of historical memory, astronomy and cosmology appear strictly related: those very skies, felt as astonishingly beautiful, are soon related to Man's origin.

While we must then acknowledge the contiguity between ancestral admiration and modern cosmology, as well as the graduality of transition from *cultural* to *scientific* cosmology, it would be badly mistaken disregarding the deep mutation occurred in the last decades. As a matter of fact, our culture has created a cosmology which is no longer an expression of philosophical views, being rather a daugther of experimental and observational data.

It is however difficult to locate the transition. When the ancient made use of *scriptures* to fix the outcome of centuries of oral tradition, they were exploiting one of their most advanced techniques. In a time, as the present–day, when all people are trained to write and read and paper, ink and books are allowed to all, we hardly perceive the significance that *owing scriptures* could mean, for a primeval culture based on agricolture and animal breading, when kings could rule huge territories without being trained to write and read. This was not so different from what the fathers of cosmology did, when they fixed the orthodoxy of their though, by using one of the most advanced technique they could exploit, modern mathematics. It is also possible that, in a few centuries, if Man will succeed in achieving a technological control of terrestrial environment, the mathematics available and needed by all will include the analytical tools used by the fathers of modern cosmology.

Accordingly, the use of mathematics certainly indicates that human culture has made enourmous steps forwards, but, by itself, it is not a signal of mutation in the nature of cosmological thought.

We may then recall that Isaac Newton (1687) himself formulated what can be defined as *cosmological problem*: what is the evolution of a homogeneous isotropic self–gravitating matter distribution without boundaries. Newton's gravitational equations could not solve this problem. On the contrary, it was soon discovered that Einstein's General Relativity (1915, GR) had the power to face it. Even without entering into the detailed historical development of these early stages of modern cosmology, it is well known that the whole *cosmological problem* was solved by Friedmann (1922), Robertson–Walker(1938) and Lemaitre (1927).

Since then, modern cosmology uses the FRW (Friedmann, Robertson, Walker) GR metric

$$ds^2 = c^2dt^2 - a^2(t)d\lambda^2 \equiv g_{\mu\nu}dr^\mu dr^\nu$$

$$\text{where :} \quad d\lambda^2 = \frac{dr^2}{1-Kr^2} + r^2\left(d\theta^2 + \sin^2\theta\, d\phi^2\right) \qquad (1.1)$$

that we shall often use in the form

$$ds^2 = a^2(\tau)[d\tau^2 - d\lambda^2] \qquad (1.2)$$

where $d\tau = dt/a(t)$ yields the *conformal time*. Here $a(t)$ or $a(\tau)$ are the *scale factor* and K is dubbed *curvature constant*. (Notice that the use of the same symbol a for $a(t)$ and $a(\tau)$, although general, is mathematically incorrect: the laws by which a depends on t and τ being different.)

The very expression of the metric allows to draw a number of predictions; testing them will allow to test the metric itself. No such test was however reasonably possible when the metric was first written.

It was obviously clear, since then, that the expression (1.1) holds in a single frame of reference, once its origin O is set. As soon as a depends on time, any point, defined by a triplet r, θ, ϕ is in motion in respect to O, which is the only point at rest. For instance, if we set ourselves in a point P at distance $d = ar$ from O, we are in motion at a speed $v = \dot{a}\, r \equiv H\, d$ (here $H = \dot{a}/a$).

Accordingly, a reference frame centered in P can still have the form (1.1) only if it moves in respect to O. An observer set in P, in oder to feel at rest, will therefore have to move in respect to O.

Photons of energy ϵ, emitted in P towards O, will reach the latter point with an energy $\epsilon_o = \gamma\epsilon(1-\beta)$, obtained by performing a Lorentz transformation; here $\beta = v/c$ and $\gamma = (1-\beta^2)^{-1/2}$.

If O and P are set at infinitesimal distance, we then have

$$dv/c = H\, a\, dr/c = H\, dt = da/a, \qquad (1.3)$$

just because the photon moves on the light cone. In turn, for an infinitesimal Lorentz transformation, it is just

$$d\beta = dv/c = -d\epsilon/\epsilon = d\lambda/\lambda \qquad (1.4)$$

(here λ is the wavelength). Putting together eqs. (1.3) and (1.4) we obtain that $d\lambda/\lambda = da/a$ and, by integrating it, the relation

$$z \equiv 1 - \frac{\lambda}{\lambda_o} = \frac{a_o}{a} - 1 \tag{1.5}$$

telling us that a photon suffering a *redshift* z because of the cosmic expansion was emitted when the scale factor was

$$\frac{a}{a_o} = \frac{1}{z+1} \tag{1.6}$$

There is therefore a one–to–one correspondence between redshift and scale factor. Cosmic events can then be ordered by using z, a and, obviously, t; plus, as we shall see soon herebelow, the conformal time τ.

Two points should however be stressed:
(i) The proof given here assumes that the only motions are those strictly coherent with cosmic expansion. In the real world, corrections due to *peculiar velocities* of sources are to be expected.
(ii) All above discussion is purely geometrical, it does not require the knowledge of the source of expansion.

All above conclusions are drawn on a purely kinematical basis. Then, under the assumption that reference frames exist, where homogeneity and isotropy hold, it can be shown that the stress–energy tensor acquires the form

$$T_{\mu\nu} = (\rho + P)u_\mu u_\nu + P\, g_{\mu\nu} \ , \tag{1.7}$$

closely reminding the stress–energy tensor of a fluid, being ρ and P the energy density and the pressure of the fluid, respectively. This does not require, however, that the world contents are fluids.

Henceforth, ρ and P being defined through eq. (1.7), if it is

$$P = w\,\rho\,, \tag{1.8}$$

with constant w, the Friedmann eqs.

$$\left(\frac{\dot{a}}{a}\right)^2 = \frac{8\pi G}{3}\rho - \frac{K}{a^2}, \tag{1.9}$$

$$d(\rho a^3) = -P d(a^3) \tag{1.10}$$

hold, being just the form taken by Einstein eqs. if the metric is (1.1). (As a matter of fact, to derive the above first order equations from them, a few mathematical passages are needed.) Here dots indicate differentiation in respect to ordinary time. The quantities ρ and P will be dubbed (energy) density and pressure, all through this thesis.

When this set of mathematical problems were solved, however, cosmology had not yet changed its nature. It is clear that, over the planetary or even the

Milky Way scales, the Universe is anything but homogeneous and isotropic. When this mathematics was developed, nebulae were believed not to be extra-galactic, so that the Universe was identified with the Milky Way itself.

But, even when Hubble [1] measured the distance from the Andromeda Nebula (wrong by a factor ~ 3), so discovering the galaxies, there was no indication that, over very large scales, homogeneity and isotropy could be attained. A counter example, widely debated in the Eighties, was that the very large scale matter distribution was a fractal or a multifractal.

Assuming that the "cosmological problem" had something to do with the world cosmology was then pure ideology. It has also being debated whether such an ideological bias is somehow related to the unitarian views in philosophy and theology: Monotheism projected on the physical world.

It is then often suggested that the real turning point occurred when Hubble himself discovered the cosmic expansion, and that this was the first cosmological measure. It must then be outlined that those galaxies whose distance and velocity Hubble could evaluate, lay within 6 Mpc from the Milky Way and all belong to the *Local Group*, a minor *loose group* of galaxies centered on two massive objects, the Milky Way and M31 in Andromeda. This is a fully virialized system and all motions inside it, are unrelated to the overall cosmic expansion, as are the motions of the galaxies within galaxy groups or clusters of various masses.

On the contrary, in the very paper where Hubble formulates the hypothesis of cosmic expansion, there is a clear reference to the results of GR (although overdue quotations are omitted). Citing his paper on the Proc.Nat.Ac.Sci. (**15**, 169, 1929), we shall report that he first stated to have observed *...a roughly linear relation between velocities and distances*, adding then that *The outstanding feature... is... the possibility that numerical data may be introduced into discussions on the general curvature of space.* Besides of outlining that Hubble was fully aware that the constancy of the v/r ratio was *rough*, uncertain, the reference to GR ("curvature of space") is clear: we have a clear example of an experimental physicist outlining that his data do not disagree from the prevailing theoretical views. At this stage, all the fuss on the discovery of a cosmic expansion and a primeval explosion (dubbed "Big–Bang" by one of its main opposers, Fred Hoyle) was, at least, premature.

Cosmology had then started to translate from the ideological to the physical domain, but all discussions were still pure ideology.

The real discovery of cosmic expansion took place when, with much effort, distances of galaxies beyond $\sim 10\,\mathrm{Mpc}$ could be evaluated. DeVaucouleurs and his school (1976) gave then an estimate of the Hubble parameter

$$H_o = \dot{a}(t_o)/a(t_o) \tag{1.11}$$

ranging around 100 (km/s)/Mpc; Sandage and Tamman (1960-70), with analogous techniques estimated then about 50 (km/s)/Mpc (cf. [2]). The difference between these values is an indication of the difficulty to follow the so–called

Hubble flow even when distances of tens of Mpc could be explored. As distant galaxy distances were then being measured through their recession veleocity, in this epoch astronomers begin to express distances in h^{-1}Mpc, by setting

$$H_o = 100\,h \text{ (km/s)/Mpc} \tag{1.12}$$

and so hiding the residual ignorance on H_o. This is a common practice even today, when a large set of independent observations converge into setting [3]

$$H_o = 70.1 \pm 1.3 \text{ (km/s)/Mpc.} \tag{1.13}$$

But the real turning points, which made cosmology a science, occurred in the Sixties, when the Cosmic Microwave Background (CMB) was discovered, while radiogalaxy data were showing that the Universe is evolutionary.

1.2 Various forms of Friedmann equations

The eqs. (1.9) and (1.10) are evocative of Newtonian and thermodynamical properties. If we consider the scale factor as a radial coordinate, eq. (1.9) can be read as an expression of mechanical energy conservation for a test particle (mass μ) on the surface of an homogeneous sphere of radius a and density ρ.

In fact, from the equation

$$\frac{\mu}{2}\dot{a}^2 - G\frac{\mu(4\pi/3)a^3\rho}{a} = \kappa \tag{1.14}$$

by multiplying both sides by $2/\mu a^2$ and setting $-2\kappa/\mu = K$, eq. (1.9) is easily reobtained.

Quite in the same way, eq. (1.10) can be read as $dU = -p\,dV$, just assimilating a^3 with V and setting $U = \rho a^3$. It can then be related to the first principle of thermodynamics in the absence of heat exchanges.

Eq. (1.10) then easily yields

$$d\rho a^3 = -(P+\rho)d(a^3) \quad i.e. \quad d\rho = -3(da/a)(P+\rho) \tag{1.15}$$

and the latter equation if often used in the form

$$\dot{\rho} = -3(\dot{a}/a)(P+\rho) \tag{1.16}$$

Eq. (1.9), multiplied by a^2 and differentiated in respect to time, then yields

$$2\dot{a}\ddot{a} = (8\pi G/3)2a\dot{a}\rho + (8\pi G/3)a^2\dot{\rho} \tag{1.17}$$

and, making use of eq. (1.16) we then obtain the equation

$$2\dot{a}\ddot{a} = 8\pi G a\dot{a}(2/3)\rho - 8\pi G a\dot{a}(P+\rho) \tag{1.18}$$

which can be easily reset into the form

$$-\ddot{a}/a = (4\pi G/3)(3P + \rho) \tag{1.19}$$

By using the conformal time τ it is then easy to rewrite eq. (1.9) in the form

$$(a'/a)^2 = (8\pi G/3)a^2\rho - K \tag{1.20}$$

Eq. (1.16) clearly holds also if differentiation occurs in respect to conformal time. Differentiating then eq. (1.20) in respect to τ and using eq. (1.16) we obtain

$$-\frac{d}{d\tau}\left(\frac{a'}{a}\right) = \frac{4\pi}{3}Ga^2(3P + \rho) \tag{1.21}$$

an equation analogous to eq. (1.19).

1.3 The integration of Friedmann equations

These discoveries give a sound basis to the current approach, which separates the background cosmic expansion and the evolution of its more or less local contents.

The eqs. (1.9) and (1.10) are to be integrated to follow the evolution of the background and their integration is simple if the state equation in the form (1.8) holds, with constant w. Then, eq. (1.10) contains only the variables ρ and a and yields

$$\rho/\rho_o = (a_o/a)^\alpha \qquad \text{with :} \qquad \alpha = 3(w + 1) \tag{1.22}$$

(a_o is a reference scale factor, not necessarily its today's value; ρ_o is the energy density when the scale factor is a_o). Once the scale dependence (1.22) is known, also eq. (1.9) depends on just two variables: a and t. Its integration will then tell us how the scale factor a, and then the density ρ, depend on t.

Such integration is much simpler when the term K/a^2 is negligible. In order to test when such an approximation is licit, let us first define the *critical* energy density

$$\rho_{cr} = H^2(3/8\pi G), \tag{1.23}$$

i.e. the energy density the Universe should have, in order that $K \equiv 0$. Notice that the value of ρ_{cr}, at any instant of the cosmic evolution, is defined just by the rate of cosmic expansion.

Let us then suppose that, at the same time, a cosmic component has a density ρ. We then define the *density parameter* for such component, being the ratio

$$\Omega = \rho/\rho_{cr}. \tag{1.24}$$

Making use of these definitions, eq. (1.9) yields

$$H_o^2 = H_o^2\Omega_o - K/a_o^2 \qquad i.e. \qquad -K = a_o^2H_o^2(1 - \Omega_o) \tag{1.25}$$

(here $\Omega_o = \rho_o/\rho_{o,cr}$) and, using this expression in eq. (1.9), we obtain

$$(\dot{a}/a)^2 = H_o^2 \Omega_o (a_o/a)^\alpha - H_o^2 (1-\Omega_o)(a_o/a)^2. \tag{1.26}$$

Then, the K term can be neglected at any time if $\Omega_o \simeq 1$. But, provided that $\alpha > 2$, *i.e.* $w > -1/3$, for a sufficiently smaller than a_o, the curvature term becomes negligible.

The arguments of this section allow us to draw some important conclusions:
(i) The integration of Friedmann eqs. is simple if the P/ρ ratio is constant for all physically relevant components.
(ii) If $\Omega_o \neq 0$ and the curvature term is significant today, it is easy to find a value of the scale factor below which the curvature terms becomes negligible and $\Omega \simeq 1$.

The (i) conclusion explains why we shall be devoting the whole next chapter to the dynamical Dark Energy, for which the ratio P/ρ is not constant.

The (ii) conclusion is quite significant, when data allow us to conclude that all material components, in the present epoch of the Universe, yield a density parameter $\Omega_{o,m} \sim 0.25$.

If this were due to a significant spatial curvature, as believed until the late Nineties, it implied a dramatic *fine tuning* of Ω at the Planck time, when the Universe emerges from the quantum gravity regime. It is easy to evaluate that Ω should then differ by unity by less than $1{:}10^{60}$.

Recent data, that we shall widely discuss, allowed to conclude that, although $\Omega_{o,m} \sim 0.25$, the overall present value of the density parameter approaches unity. The gap is to be covered by the so–called Dark Energy (DE), a non–material component with $w \sim -1$.

It is then clear that such component is significant in our epoch and just in it, being rapidly diluted when we go to higher redshifts.

1.4 Cosmic scales and systems

All the discussion and the conclusions of the previous sections are based on the use of FRW metric and Friedmann eqs., basic and ancient tools of any cosmological approach.

However, when we use them today, we are aware of a whole set of data that the fathers of modern cosmology did not know. This allows us to appreciate that a terrific leap forwards in the knowledge of the Universe was really made in less than a century.

The overall picture of cosmic contents is now rather clear and this allows us to set a clear cut between upper and lower cosmic scales, on the scale where dynamics begins to be ruled by pure gravitation: this is the *galactic* scale. As a matter of fact one can hardly understand the overall dynamics inside galaxies, as well as the nature and dynamics of its sub–systems, without taking into account *dissipative* forces. They are those actions which convert gravitational

energy into radiations. Only radiating away the heat produced by the $p\,dV$ work, in the gravitational growth, could stars and/or galaxies form.

Above the galactic scale the chacteristic time for dissipation exceeds the age of the Universe. Henceforth, while the basic dynamics is gravitational, dissipative forces still play important roles. First of all, they provide a radiation mechanism making objects observable. For instance, the most efficient way of discovering galaxy clusters is through the X–rays, radiated by the hot gas inside them. Then, it must be noticed that present (and future) measurements have achieved such a precision, that also corrections due to dissipative dynamics can no longer be disregarded.

The basic individuals of cosmology, however, are galaxies. They are the inhabitants of the large scale world. In this thesis we shall seldom refer to any cosmic object over a smaller scale. The typical galactic radius is $\mathcal{O}(10\ \mathrm{kpc})$. The typical density contrast, between the inside of a galaxy and the whole Universe is $\mathcal{O}(10^7)$. These can be interpreted by saying that the *linear* radius of a galaxy is $10 \times 10^{7/3}\mathrm{kpc} \sim 0.2\,\mathrm{Mpc}$: in a sense, this is the radius of sphere wherefrom all materials contained in a single galaxy have been drained.

Systems made of galaxies may be bound or unbound. The greatest bound systems in the Universe are dubbed *galaxy clusters*. Their present radius is ~ 1–$2\,h^{-1}\mathrm{Mpc}$ and their typical density contrast is $\mathcal{O}(200)$. Accordingly, their linear radius would be ~ 6–$10\,h^{-1}\mathrm{Mpc}$, coinciding with the radii of the greatest cosmic *voids*.

All that leads to the picture of the Universe that deep observations and numerical simulations made familiar to us. Matter is distributed along sheets and filaments, intersecting in knots where galaxy clusters are observed. The mass of the largest clusters exceeds some $10^{15}h^{-1}M_\odot$. Galaxy sets down to $\sim 10^{14}h^{-1}M_\odot$ are considered clusters. Smaller galaxy sets are dubbed *groups*. Galaxy masses range from $\sim 10^8$ to $\sim 10^{12}h^{-1}M_\odot$, but these boundaries are not so well defined, as the very limits, over which dissipative forces cease to be dynamically significant, are loose. In a similar fashion it is often unclear if a given object is an individual galaxy, perhaps a satellite of a bigger galactic objects, or is a part of that galactic system.

These ambiguities, however, did not prevent us from achieving a general picture of the material contents of the Universe and the very fact that observations and simulations end up with similar pictures means that we are understanding why the Universe has the observed structure.

This does not mean that all problems are solved. On the contrary, in order to achieve such extraordinary results, unexpected assumptions were to be made. To justify such assumptions we need to ask ourselves new questions, in a field where large scale and microphysical measures and theory intersect, in a continuous dialectical way.

1.5 The cosmic horizon

Galaxy, group and cluster scales are to be compared with the so–called *cosmic horizon*, encompassing the portion of the Universe causally connected with us. The notion of horizon is spparently simple. As the Universe exists since a finite time t_o, the maximum distance wherefrom we can receive a signal is $c\,t_o$, owing to the fact that the maximum physical velocity is the *speed of light* c.

Unfortunately this argument is not simple but simplicistic. We can easily understand this if we remind that all distances scale with $a(t)$. If A and B are now at a distance R, at the time $\bar{t}$, when $a(\bar{t}) = 0.5\ a(t_o)$, their distance was $R/2$. At the time $\bar{t}$ light could travel from A to B in half time. Everything is as though the speed of light were higher in the past, increasing $\propto a^{-1}$. Hence, the maximum distance from which a signal can arrive is surely $> c\,t_o$. It could also be infinite, if the scale factor decreases fastly enough when going back in time.

The problem must then be treated with the appropriate differential tools and one easily discovers that, if $a \propto t^\alpha$ the horizon size, at the time t, reads

$$l_p = \frac{1}{1-\alpha} c\,t \tag{1.27}$$

provided that $\alpha < 1$. For $\alpha > 1$, instead, l_p is infinite.

Through similar passages, one can easily solve another problem, finding the maximum distance that a signal, emitted today, can reach. The intuitive idea that there is no limit to such distance is false. Once again, the key issue is whether a or t increases more rapidly. One then finds that this maximum distance reads

$$l_e = \frac{1}{\alpha-1} c\,t \tag{1.28}$$

provided that $\alpha > 1$. For $\alpha < 1$, instead, l_e is infinite.

The horizon (1.27) is dubbed *particle horizon*. The horizon (1.28) is dubbed *event horizon*. The expansion may not follow an exact power law, but it is then easy to show that a particle (event) horizon exists if the expansion is steadily decelerated (accelerated). In the real world, which is undergoing an accelerated expansion, there is then an event horizon. However, a transition from deceleration to acceleration occurred "recently" at a redshift $\sim$ 0.5–1; therefore, there is also a particle horizon.

If the expansion had always occurred as though the only *substance* in the Universe were non–relativistic particles, it would be $\alpha = 2/3$ and $l_p = 3c\,t_o = 2c/H_o$. This value is not far from the correct one and would be

$$(600,000/100\,h)\,\mathrm{Mpc} \;=\; 6000\,h^{-1}\mathrm{Mpc}\,.$$

This is an important reference point: The greatest bound systems in the Universe derive from a sphere whose size is $\sim 1/100$ of the horizon. The scale range where inhomogeneities have not yet reached a non–linear regime is therefore

rather restrict and, even on the horizon size, homogeneity is approached, not attained.

Altogether, to have motions running according to an almost pure Hubble flow, we must reach a scale $\sim$ 60–600 h^{-1}Mpc, 10–100 times more than the scale over which Hubble somehow pretended that a coherent expansion was observable.

Available deep galaxy samples currently reach distances in this range. This observational material is among the elements which allow to state that cosmology has fully turned into a new branch of physics.

1.6 Cosmological inputs to physics

As a matter of fact, some of the most important discoveries in physics, in the last decades, have a cosmological basis. In this introductory chapter I will refrain from entering into the complex data analysis which allowed to state the existence of non–baryonic matter (mostly quoted as Dark Matter: DM) and, more recently, of the so–called Dark Energy (DE). Some of this analysis will be reported in the next chapters.

By DM we mean particles not included in the standard model of elementary interactions. In a time when particle physicists are desperetely seeking signal of physics *beyond the standard model* and the LHC is being built to such aim, cosmology already grants that such physics must exist.

Even more peculiar are the features of the so–called DE. Both DM and DE are characterized by the (almost) total absence of interactions with standard model particles, apart gravitation.

It may be worth outlining soon why the Dark Side of the Universe needs two distinct components. DM and DE are characterized by different physical features: DM clusters and it was DM to provide the seeds of observed cosmic structures; baryons later accreted on them. DE, instead, does not cluster, in general; it is necessary to account for very large scale properties of the Universe; DE inhomogeneities existed on scales out of the horizon and rapidly faded when the horizon reached each scale. The two components are then characterized by different state equations. For DM, the ratio $w_c = P_c/\rho_c$ is assumed to vanish and is certainly quite small. For DE, instead, the ratio $w_{de} = P_{de}/\rho_{de}$ is negative and approaches -1.

Cosmological and astrophysical analysis mostly make a further assumption on the Dark Side, that DM and DE, besides of being dynamically isolated from baryonic matter, are also not interacting between them.

If this is true, astrophysics and cosmology are unlikely to provide much more ideas on the nature of DM, in a near future, apart of possible limits on the mass of its particles, if the scarsity of observed galactic satellites will be explained – partially or exclusively – by warm DM, a fairly unlikely option.

On the contrary, astrophysical and cosmological observations can still say a lot on DE nature. Evaluating the redshift dependence of $w_{de} = P_{de}/\rho_{de}$ is

hard, but can play a critical role to this aim.

No available data however can exclude that interactions occur within the Dark Side. The quest for data confirming its absence or measuring its intensity is one of the critical frontiers of research. It is also a field where large scale data bear a direct microphysical impact. For our undestanding of elementary interactions, large scale measures on DE nature are, at least, as important as accelerator outputs.

In this thesis I will widely discuss one of the most powerful tools to carry on this research, the analysis of *cosmic shear tomography*. This tool will provide us data on the distribution of matter, at different depth and redshift, unrelated from the light it emits.

Astronomical observations, until now, were mostly based on the study of the light emitted by sources. We must add to that neutrino observations, and neutrino telescopes will be another independent source of astronomical information.

A completely indipendent pattern is however based on the study of *gravitational lensing*. The formation of spectacular arclets and multiple images, due to the so–called *strong lensing* was widely observed in the last two decades. This cosmic phaenomena however require *ad–hoc* distributions of cosmic objects; accordingly, statistical studies based just on strong lensing do not allow an exhaustive insight into matter distribution over large scales.

Weak lensing (WL), instead, although much less spectacular and harder to measure, is much more promising. In the last few years many studies have managed to detect *cosmological shear* due to WL in random patches of the sky [4, 5, 6, 7, 8, 9, 10, 11, 12, 13, 14, 15, 16, 17, 18]. While early studies were primarily concerned with the detection of a non-zero WL signal, recent results already put constraints on cosmological parameters such as the matter density parameter Ω_m and the amplitude σ_8 of the power-spectrum of matter density fluctuations.

Moreover, the combination of WL measures with other cosmological probes, such as Cosmic Microwave Background (CMB) observations, can remove parameter degeneracies [19]. It should also be outlined that an extensive analysis of WL will allow a much better exploitation of light signals as, combining WL with galaxy redshift surveys, one can say a final word on how light distribution traces mass distribution.

It should then not come as a surprise that, among the cosmological probes allowing the analysis of the nature of DE, the cosmological WL has been earning a fundamental role (see [20, 21, 22, 23] for a thorough review). In fact, next generation WL surveys, covering a significant fraction of the sky, will allow to observe galaxies and cluster evolution with redshift.

After introducing all needed theoretical and observational background, I shall also report some of our contributions on the deepening of these essential questions, probably among the main physical questions that the incoming century will have to face.

Chapter 2

The dark side of the Universe

2.1 Why Dark Matter

Once radioastronomy put in evidence deviations from 1.5, in the steepness of the logN–logS curve, cosmology had to abandon any model not admitting evolution. *Big–Bang* cosmology, however, still had a number of possible variants. The discovery of CMB forced then to select the class of *hot–big–bang* models. This meant that the ratio between baryon and photon number had to be set at values close to 10^{-10} and this is an evident *fine tuning* that fundamental physics, since then, has been trying to explain.

It is however thanks to this fine tuning that Big–Bang–NucleoSynthesis (BBNS) provides a close link between cosmology and nuclear physics. Curiously enough, George Gamow had predicted the existence of CMB since the late Fourties [25], in order to explain the fraction of ^{4}He observed in the Sun and other stars. The temperature he predicted (4–5 K) is quite close to the observed value of 2.725 ± 0.002 K [24]. It is still hard to realize why, although such prediction could soon be tested, none then cared to do so, and science had to await two fair engeniers, casually meeting it (and trusting the signal they measured).

After CMB discovery, BBNS was carefully revisited and further links were found with fundamental physics. For instance, the number of families in the Standard Model was fixed by cosmology some ten years before LEP confirmed its value.

All of that had however a severe price to pay. In order to fit all available data on light nuclide abundances, the baryon density parameter was soon constrained to a very low value $\Omega_{b,o} < 0.05$. Let us remind that density parameters express the ratio between the average density of a given cosmic component (baryons in this case) and the critical density $\rho_{c,o} = 3H_o^2/8\pi G$, *i.e.* the density required in order to account for the observed Hubble parameter in a spatially flat model ($K = 0$). In turn, the gravitational dynamics in galaxy clusters led to require that the overall matter density parameter $\Omega_{m,o}$ is, at least, 3 times

greater.

Baryonic matter is made by all massive particles of the standard model including, *e.g.*, electrons, but excluding neutrinos, in spite of their (tiny) mass, and photons, which constitute the *radiative* component. This means that there must exist particles not included in the standard model, whose only appreciable interaction with standard model particles, in our epoch, is gravity.

This was however just a first reason compelling to accept the idea of non–baryonic Dark Matter. The amplitude of CMB anisotropies and polarization being a further decisive argument, that we shall discuss in more detail in the chapter 5. Here, let us just outline that matter density fluctuations, in a matter dominated expansion, can grow $\propto a$, at most . Accordingly, since the hydrogen recombination, occurring at $z \sim 10^3$, their amplitude has increased by a factor 10^3, at most; therefore, in order to reach non–linearity and form bound systems, they should have been $\mathcal{O}(10^{-3})$ or greater, at recombination. As a matter of fact we can measure baryon density fluctuations at recombination, through CMB anisotropies, expected to have a similar amplitude. Observations, telling us that $\delta T/T \sim 10^{-5}$, tell then us that the seeds of the present cosmic structure could not have been baryon fluctuations and that there must exist, at recombination, another cosmic component, in which fluctuations were much wider than in baryons.

These arguments have been widely refined by current analysis and it is however not premature outlining since here that recent sets of data, concerning both CMB [27, 28, 29, 30, 31, 32, 33, 34] and deep galaxy distribution [35], fit to an extensive range of cosmological models, provide stringent constraints on all cosmological parameters, including $\Omega_{o,b}$, so finding a full agreement with BBNS predictions.

2.2 Why Dark Energy

This fit also requires that the density parameter for all clustered matter is $\Omega_{o,m} \simeq 0.25$ and that the overall geometry of the space section of the cosmic metric is (nearly) flat. The gap is then to be covered by a non–clustering component. By itself this is a clear evidence of DE (although an intervention of DE in non–linear clustering has been also envisaged by some authors).

Quite in general, we may say that baryon matter signals can be appreciated over any scale, starting from lab scales. DM signals, instead, are to be primarily traced over cosmic scales. (We do not forget the fundamental experimental activities of various groups, trying to detect DM particles in laboratory.) DE signals, finally, are only perceivable on a very global scale.

As a matter of fact, the first signals that DE existed came from the analysis of high–z SNIa distributions [36, 37, 38], which apparently indicate that the present cosmic expansion is accelerated.

This is a feature that no matter source may cause. The assumption that the rate of cosmic expansion slows down was so diffused, that its time variation

is measured by a "*deceleration*" parameter

$$q = -\frac{\ddot{a}}{aH^2}, \tag{2.1}$$

rather than by an "acceleration" parameter. Then data yield a present value $q_o < 0$.

According to the Friedmann equations and the critical density definition,

$$-\ddot{a}/a = (4\pi G/3)(3P + \rho), \qquad H^2 = (4\pi G/3)\rho_{cr},$$

we then easily obtain

$$q = \Omega\frac{1 + 3w}{2} \tag{2.2}$$

in the case of a single cosmic component; this expression is soon generalized to more components, with density and state parameters Ω_i and w_i, reading

$$q = \sum_i \Omega_i \frac{1 + 3w_i}{2}. \tag{2.3}$$

Both eqs. (2.2) and (2.3) show that, in order to have $q_o < 0$, we need one or several components with $w_i < -1/3$.

Among possible explanations of this data set, I wish to outline some options, alternative to the idea that an extra *substance* is needed, which will then be left apart all through this thesis.

A first option is that GR, obtained from a lagrangian density $\mathcal{L} = R$ (curvature scalar), is just a 0–th order approximation of the true gravitational theory, whose lagrangian density, *a priori*, should read $\mathcal{L} = f(R)$; data are then used to constrain the function f.

Another option is that DE arises from the back reaction of the development of inhomogeneities onto the background metric [39, 40]. This scheme started from ancient ideas of Kristian & Sachs (1966), elaborated by Ellis (1984) and [41, 42]), but still meets severe difficulties.

2.3 False vacuum ad Dark Energy

When cosmic acceleration was discovered, cosmologists had an historical tool to fit data, ΛCDM models. These models could be interpreted as comprising a source, whose state equation reads $p = -\rho$ $(= -\Lambda)$. Here p and ρ are pressure and energy density of a source whose stress energy tensor is $\Lambda g_{\mu\nu}$. ΛCDM models were first discovered and then renegued by Einstein, when he added a *cosmological constant* to his own equations. Curiously enough, as though their very existence was due to him discovering them.

Leaving apart his early formulation, eq. (2.3) immediately shows that, if $\Omega_{o,m} \simeq 0.3$ and $\Omega_{o,\Lambda} \simeq 0.7$ it is $q_o = 0.15 - 0.7 = -0.55$, a value in fair agreement with SNIa observations.

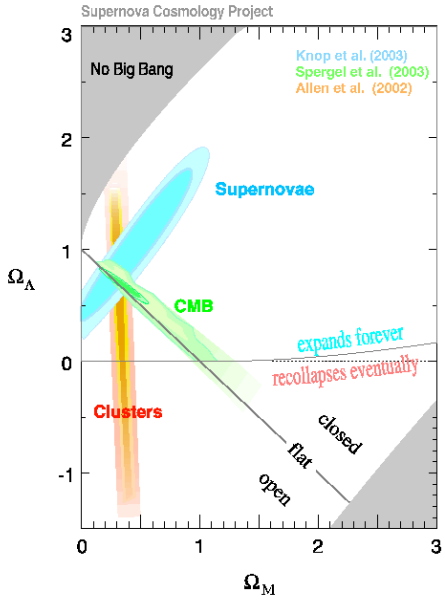

Figure 2.1: Constraints on ΛCDM model arising from CMB anisotropies, deep galaxy samples, SNIa distribution and other data. This plot was drown in 2003; recent data are even more constraining.

As a matter of fact all available cosmological data can be fitted by ΛCDM models. Figure 2.1 shows the constraints on such models, arising from CMB anisotropies, deep galaxy samples and SNIa distribution, as they were around 2003. More recent data allowed to put much more stringent constraints and confirm that the region of intersection is also associated to $\Omega_{b,o}$ values which agree with BBNS. The best–fit ΛCDM model, taking into account all the above data, is also dubbed *cosmic concordance model*.

The old relativist idea that Λ is essentially a *geometrical* constant is not an explanation, but just a way to rephrase the problem. The quest for the physical origin of a cosmic component with widely negative pressure is then open.

A firm point is that there is no ordinary free particle distribution which allows for negative pressure. Let $F(\mathbf{x}, \mathbf{p}, \tau)$ be the distribution of any set of free particles in the phase space, yielding the distribution $f(\mathbf{p}, \tau)$ in the momentum space in the homogenous case. The components of the stress energy tensor, for such particle distribution, read

$$T^\mu_\nu = \int \frac{d^3p}{p_0} p^\mu p_\nu f(\mathbf{p}, \tau) \tag{2.4}$$

so that

$$\rho \equiv T^0_0 = \int d^3p\, p^0 f(\mathbf{p}, \tau)\ , \quad 3\,P \equiv T^i_i = \int d^3p \left(p^0 - \frac{m^2}{p^0}\right) f(\mathbf{p}, \tau)\ . \tag{2.5}$$

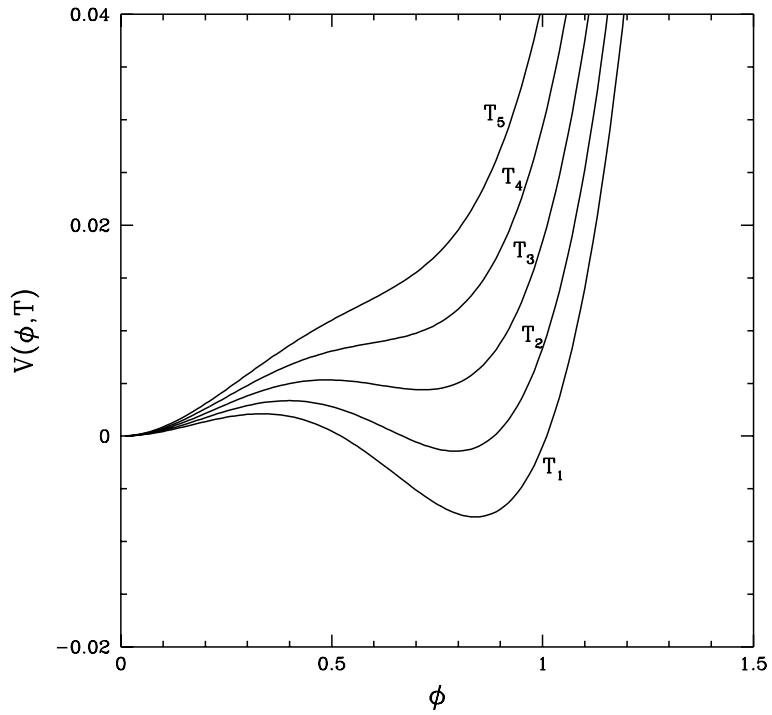

Figure 2.2: ϕ dependence of *Coleman–Weinberg* potential when T decreases from T_5 to T_1. For the sake of simplicity, potentials were plotted so to coincide at $\phi = 0$. The 0–level of energy, however, varies with T and coincides with the absolute minimum in each curve. Accordingly, for any $T > T_2$, the configuration $\phi = 0$ corresponds to the true vacuum. When $T < T_2$, instead, the true vacuum corresponds to a configuration with $\phi \neq 0$ (spontaneous symmetry breaking), while the symmetrical configuration $\phi = 0$, which could be temporarily stable, yields a *false vacuum* state. The vacuum energy density ρ_v, in such state, is the difference between the levels of the local and global minima; the vacuum pressure is then $P_v = -\rho_v$.

Eqs. (2.5) shows that $\rho = 3P$, for any particle distribution, as soon as $m \ll p^0$; they also show that, in order that $P < 0$, it should be $m > p^0$, as is for tachions.

Besides of ordinary free particles, however, we may consider a *false vacuum*. This idea was introduced in the context of relativistic phase transitions. The potential (density) for a Higgs field, *e.g.*, could have a Coleman–Weinberg behavior (see Figure 2.2), so allowing for a *false vacuum* component.

It is well known that relativistic phase transition occurred during the early cosmic expansion. The last of such transitions has probably occurred at a temperature $T_{ew} \simeq 100\,\mathrm{GeV}$, when the $SU_L(2) \otimes U_Y(1)$ symmetry of electroweak interaction has broken, so that the only remaining gauge symmetry is $U_{em}(1)$ and the only massless gauge field is the photon.

When the cosmic temperature was $\sim T_{ew}$ and before the symmetry breaking occurred, the Universe layed in a false vacuum state whose energy density was

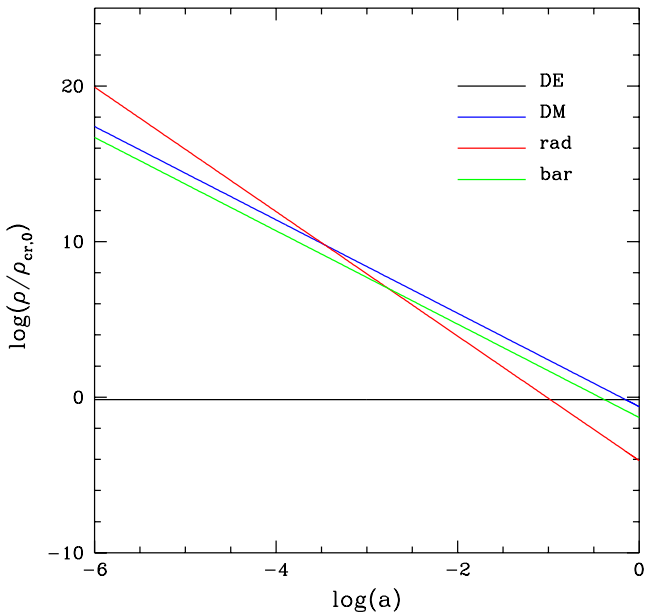

Figure 2.3: Evolution of energy density for DE, DM, radiation and baryons in a ΛCDM model.

$\rho_{v,ew} \sim T_{ew}^4$. When the passage to the true vacuum state finally occurred, this coherent energy was thermalized.

It is easy to compare T_{ew}^4 with the energy density of a present false vacuum state, assumed to cause the cosmic acceleration. The present critical density is $\simeq 0.25\ h^{-2}10^{-4}(\pi^2/15)T_o^4$; here $(\pi^2/15)T_o^4$ is the energy density of CMB radiation, whose temperature is $T_o \simeq 2.3$ eV. Accordingly, we should have that $\Lambda \sim (10T_o)^4$ so that

$$\Lambda \sim (10T_o/T_{ew})^4\rho_{v,ew} \simeq (10^{-2.5}/10^{11})^4\rho_{v,ew} \simeq 10^{-52}\rho_{v,ew}\ . \qquad (2.6)$$

This is still an optimistic view, as others believe that the fair comparison to be made is with Planck energy density.

Besides of this *fine tuning* problem, ΛCDM models suffer of a severe *coincidence* problem, illustrated in Figure 2.3, making clear that vacuum energy density became a significant cosmic component only quite recently. This fact, by itself, appear a rather peculiar coincidence. But there is more: the linear growth of any cosmic inhomogeneity is severely suppressed when vacuum energy density becomes significant and would be stopped if such component is dominant. Therefore, *e.g.*, if ρ_v were 10 times greater than observed, no significant large scale structure could form in the Universe. It is as though ρ_v had been wisely tuned, *a priori*, just to allow cosmic structures to arise.

2.4 Dynamical Dark Energy

In order to ease the above *fine tuning*, an alternative option is to have recourse to a scalar field ϕ, self–interacting through an effective potential $V(\phi)$. Under suitable conditions, such a component has widely negative pressure. Notice, however, that this approach will not ease the coincidence problem. Moreover we shall then make clear *why* this *substance* is to be treated as a field instead of quanta.

From the ϕ field lagrangian we can then derive the stress–energy tensor of the DE field and, from its components, we have

$$\rho_{de} = \rho_k + \rho_p \ , \qquad P_{de} = \rho_k - \rho_p \tag{2.7}$$

with

$$\rho_k = \phi'^2/2a^2 \ , \quad \rho_p = V(\phi) \ , \tag{2.8}$$

being the kinetic and potential energy densities of ϕ (in this section I shall mostly use the conformal time τ and set $' \equiv d/d\tau$). Either from the Euler–Lagrange equation, or from the Friedmann eq.

$$\rho'_{de} + 3(a'/a)(3P_{de} + \rho_{de}) = 0,$$

we then easily obtain the equation

$$\phi'' + 2\frac{a'}{a}\phi' + a^2 V_{,\phi} = 0 \tag{2.9}$$

to be integrated to obtain the time evolution of ϕ and, thence, of ρ_k, ρ_p, ρ_{de} and P_{de}. From these variables we then obtain the time dependence of

$$w = \frac{\rho_k - \rho_p}{\rho_k + \rho_p} \tag{2.10}$$

Notice then that it is also

$$\frac{\phi'^2}{a^2 V} = 2\frac{1+w}{1-w} \tag{2.11}$$

so that the DE state parameter w approches -1 only when the kinetic energy vanishes. It is also important to notice that $w \simeq 1$ (*stiff matter*) for $\rho_k \gg V$ (in the sequel, the state parameter w without index will always refer to DE).

Unfortunately, however, in order to integrate eq. (2.9), the τ dependence of the scale factor a must be known. This is to be worked out from the Friedmann equation

$$\left(\frac{a'}{a}\right)^2 = \frac{8\pi}{3} G\rho a^2 \tag{2.12}$$

(we assume a vanishing spatial curvature K), which can only be integrated once the τ dependence of ρ is known. Accordingly, either $\rho_{de} \ll \rho$, as can be in the early Universe, or eqs. (2.9) and (2.12) ought to be simultaneously solved, as a system of equation, by using suitable numerical techniques.

Table 2.1: Some scalar field potentials usually studied in dark energy models.

Scalar field potential	**Reference**
$V(\phi) = \frac{\Lambda^{4+\alpha}}{\phi^\alpha}$	Ratra & Peebles 1998 [43]
$V(\phi) = \frac{\Lambda^{4+\alpha}}{\phi^\alpha} e^{\frac{\kappa}{2}\phi^2} \quad \kappa = 8\pi G$	Brax & Martin 2000 [51]
$V(\phi) = \Lambda^4 e^{-\lambda\phi}$	Wetterich 1988, Ferreira & Joyce 1998 [45]
$V(\phi) = \Lambda^4[e^{\alpha\kappa\phi} + e^{\beta\kappa\phi}]$	Barreiro, Copeland & Nunes 2000 [46]
$V(\phi) = \Lambda^4[1 + \cos\frac{\phi}{f}]$	Kim 1999 [47]
$V(\phi) = \Lambda^4[(\phi - B)^\alpha + A]e^{-\lambda\phi}$	Albrecht & Skordis 2000 [48]
$V(\phi) = \Lambda^4[\cosh(\lambda\phi) - 1]^p$	Sahni & Wang 2000[49]

As a matter of fact, in early epochs, when the contribution of DE was negligible or sub–dominant, the expansion rate depends almost exclusively on the cosmic component whose density prevails.

Accordingly, $\mathcal{H}(\tau) \equiv a'/a$ depends on the dominant component and this changes the behavior of $\phi(\tau)$, according to eq. (2.9). Therefore, the equation of state of DE depends on the cosmic component dominating the expansion in each cosmological epoch.

Quite in general, the solution of a differential equation depends on the initial conditions. There exists however a class of potentials $V(\phi)$ which own an attractor solution, *i.e.*, such that – almost indipendently from the initial conditions set well inside the radiative epoch –, at any relevant epoch the behavior of $\phi(\tau)$ does not depend on the assigned initial conditions. These potentials are defined *tracker potentials* and the attractor solutions are denominated *tracking solutions*.

Much work has been done to find out tracker potentials. In Table 2.4 we list some of the tracker potentials.

This kind of DE, due to a scalar field dynamics is dubbed *dynamical DE* (dDE) or *quintessence*.

Among these potentials I shall often select the SUGRA potential

$$V(\phi) = (\Lambda^{4+\alpha}/\phi^\alpha)\exp(4\pi\phi^2/m_p^2) \tag{2.13}$$

introduced by Brax & Martin [44] (see also [50, 51]). Here $m_p = G^{-1/2}$ is the Planck mass. This potential has been shown to fit all available data at least as well as ΛCDM (Colombo & Gervasi 2006).

It can be verified that, starting from a tracking solution, this potential yields that $\phi \sim m_p$ today, when $V(\phi) \sim \rho_{o,cr}$. Accordingly, we must have

$$\Lambda^4(\Lambda/m_p)^\alpha \sim (10\,T_o)^4 \tag{2.14}$$

and, *e.g.* for $\alpha = 4$, this yields

$$\Lambda \sim \sqrt{10^{28} \times 10^{-2.5}}\text{eV} \sim 10^3\text{GeV}$$

an energy range familiar to particle physics, where the electroweak transition and/or the soft SUSY break may occur.

Accordingly, a dDE approach does not seem to require the introduction of fine–tuned energy scales.

It has however been outlined that this result is made possible by the tiny mass the ϕ field must have, in order that quintessence behaves as a field, its quanta being essentially delocalized. According to some researchers, this reintroduces a sort of fine tuning.

2.5 Coupled Dark Energy

The essential feature of the scalar field ϕ, in order that it yields DE, is its self–interaction through a potential $V(\phi)$: when the self–interaction term dominates energy density and pressure achieve opposite signs.

Altogether, therefore, in dDE theories, the ϕ field must interact with itself and with the gravitational field.

It is then natural to wonder whether any other interaction is allowed to it. If DE is coupled to another cosmic component, its stress–energy *pseudo*–conservation equation, $T^\mu_{\nu;\mu} = 0$ $(\mu, \nu = 0, 3)$ would be modified. The simplest form of possible coupling is a linear one. It can be formally obtained by performing a conformal transformation of Brans–Dicke theory (see e.g. [52]), where gravity is modified by adding a ϕR term (R is the Ricci scalar) to the Lagrangian.

Interactions with baryons are constrained by observational limits on violations of the equivalence principle (see, e.g., [53, 54]) No similar constraints hold for DE–DM interactions. In this case, constraints will follow from cosmological observations.

The option of DE–DM coupling was considered several times in the literature, starting from Wetterich (1988) [55]. Its physical effects were then discussed more in detail by Amendola (1999, 2000) [52, 56] and Holden & Wands (2000) [57], who stressed that, owing to the vanishing of the trace of $T_{\mu\nu}$ for zero–mass components, no photon and neutrino interaction with DE follows. Theoretical motivations for DE–DM coupling were found, in superstring models and in brane cosmology, by Gasperini, Piazza & Veneziano (2002) [58].

Let then $T^{(\phi)}_{\mu\nu}$ and $T^{(c)}_{\mu\nu}$ be the stress–energy tensors of a scalar field ϕ and DM, respectively. Leaving apart the connection with Brans–Dickie cosmology,

we may then notice that general covariance itself requires that the total stress–energy tensor $T_{\mu\nu}$ fulfills the continuity equation

$$T^{\mu}_{\ \nu;\mu} = 0 \ , \tag{2.15}$$

but it does not prevent an interaction between DE (the ϕ field) and DM such that

$$\begin{aligned} T^{(\phi)\mu}_{\ \ \nu;\mu} &= +CT^{(c)}\phi_{;\nu}, \\ T^{(c)\mu}_{\ \ \nu;\mu} &= -CT^{(c)}\phi_{;\nu} \ . \end{aligned} \tag{2.16}$$

As is known, eq. (2.15) tells us how the 4–momentum components evolve under the action of gravity. In the absence of gravity, they yield the conservation of momentum and energy. Accordingly, the coupling described by eqs. (2.16) accounts for a transfer of energy and momentum between DE and DM.

The analytical treatment of a coupled DE model (cDE) is clearly more involved than dDE, in particular for what concerns the dynamics of density fluctuations. Thy are usually treated either in the synchronous or in the Newtonian conformal gauge. Assuming zero spatial curvature, in the former case we the FRW metric becomes

$$ds^2 = a^2(d\tau^2 - \eta_{ij}dx^i dx^j) \ . \tag{2.17}$$

If x^α ($\alpha = 1, 2, 3$) are cartesian orthogonal coordinates, it is $\eta_{ij} = \delta_{ij} + h_{ij}$, so that any peculiar gravity due to density fluctuations is described by h_{ij}. In the latter case, instead,

$$ds^2 = a^2(\tau)[(1 + 2\Phi)d\tau^2 - (1 - 2\Psi)dx_i dx^i] \tag{2.18}$$

and, in the absence of anisotropic stresses, peculiar gravity is fully described by the potential $\Psi = \Phi$.

In the former case, the *conformal time* τ is *universal*, in the latter case it depends on the site.

In the absence of fluctuations, in the frame of reference where the metric is FRW, eqs. (2.16) yield:

$$\phi'' + 2\mathcal{H}\phi' + a^2 V_{,\phi} = C\rho_c a^2, \tag{2.19}$$

$$\rho'_c + 3\mathcal{H}\rho_c = -C\rho_c\phi' \tag{2.20}$$

An analysis of background expansion in the presence of coupling has been performed by various authors [55, 59, 52, 56, 57, 58]. The equations yielding the behavior of the different cosmic components are formally simpler if the following five variables are used:

$$x = \frac{\kappa}{H}\frac{\phi'}{\sqrt{6}}, \quad y = \frac{\kappa}{H}\sqrt{\frac{V}{3}}, \quad z = \frac{\kappa}{H}\sqrt{\frac{\rho_\gamma}{3}}, \quad v = \frac{\kappa}{H}\sqrt{\frac{\rho_b}{3}}, \tag{2.21}$$

ρ_γ and ρ_b being the energy densities of radiation (including neutrinos, assumed to be massless) and baryons, respectively. Here $\kappa^2 = 8\pi G$; furthermore, $H = \mathcal{H}a$ is the usual Hubble parameter.

x^2, y^2, z^2 and v^2 coincide with : the density parameter of the kinetic component of ϕ and the potential components of ϕ, radiation and baryons, respectively. The cold DM energy density parameter is obviously $\Omega_c = 1 - x^2 - y^2 - z^2 - v^2$.

The potential $V(\phi)$ defines a function $f(\phi)$ through to the relation

$$V(\phi) = Ae^{-\kappa\sqrt{\frac{2}{3}}\mu f(\phi)\phi} \ , \tag{2.22}$$

which also depends on the choice of the dimensionless constant μ. The exponential case (Wetterich 1995, Amendola 2000) corresponds therefore to $f = 1$, a constant potential [60] to $\mu = 0$, the power law $V \sim \phi^{-\alpha}$ to $f(\phi) = \sqrt{(3/2)}\alpha \log\phi/(\kappa\mu\phi)$, and a SUGRA type potential $V \sim \phi^{-\alpha}e^{\frac{\kappa}{2\phi^2}}$ to $f(\phi) = \sqrt{(3/2)}[\alpha\log\phi/(\kappa\phi) - \kappa\phi/2]/\mu$.

It is then also convenient to take as independent variable $l_a \equiv \log a$, instead of the scale factor a or the time t.

If differentiation in respect to l_a is still indicated by a prime, the Einstein equations and the conservation equations, for the components of the 4–momentum of the scalar field, radiation, baryons and CDM then read

$$\begin{aligned}
x' &= \left(\frac{z'}{z} - 1\right) x - \mu f_1 y^2 + \beta(1 - x^2 - y^2 - v^2 - z^2), \\
y' &= \mu f_1 xy + y\left(2 + \frac{z'}{z}\right), \\
z' &= \frac{z}{2}\left(3x^2 - 3y^2 + z^2 - 1\right), \\
v' &= \frac{v}{2}\left(3x^2 - 3y^2 + z^2\right).
\end{aligned} \tag{2.23}$$

Here

$$\beta = \sqrt{3/2\kappa^2}\ C = (3/\pi)^{1/2}(C/m_p) \tag{2.24}$$

is a dimensionless parameter suitably gauging the interaction strength, while $f_1 = \frac{df}{d\phi} + f$.

Note that the system (2.23) is subject to the condition $x^2+y^2+v^2+z^2 \leq -1$. To close the system one needs also the Friedman equation

$$\frac{H'}{H} = -\frac{1}{2}\left(3 + 3x^2 - 3y^2 + z^2\right). \tag{2.25}$$

On the basis of these equations the time dependence of the density parameters is obtainable.

Some early work on cDE apparently allowed to ease the coincidence problem. Some evidence of how this occurred is still exhibited in the Figure.

In fact, starting from a tracker solution, at recombination, DE energy density is mostly due to its kinetic component and, therefore, $w_{de} \simeq 1$. Because of the coupling, energy is transferred from DM to DE, where it dilutes $\propto a^6$ and is so washed away. This however allows ρ_{de} to keep to a significant level which, for large β values, can be comparable with DM. In turn, because of the coupling, ρ_c also declines in time more rapidly than a^3. This kind of evolution approaches an end when ϕ becomes so large that $V(\phi)$ is no longer negligible. Then ρ_{de} rapidly increases and overcomes ρ_c.

For $\beta \sim \mathcal{O}(1)$, DM and DE exhibit then an almost parallel behavior, since recombination to the eve of the present epoch. DE, therefore, is a significant portion of the Universe contents at $z \sim 10^3$, so easing the coincidence problem.

A careful comparison with observational data, however, led to exclude β values above $\sim$ 0.07–0.1, at the 3–σ level. Accordingly, cDE could hardly be "used" to ease coincidence.

In chapter 3, however, we show greater couplings, made compatible with data by the symultanous presence of significant ν masses.

The maximum β considered in the Figure, however, is still 0.21. By using a Fisher matrix technique, it appears to be consistent with available data at the 2–σ level, so pushing upward observational limits on β by more than a factor 2.

It must be acknowledged that the easing of the coincidence problem, even with $\beta \sim \mathcal{O}(0.2)$, is not completely satisfactory. However, once the gene has escaped from the bottle, it is almost impossible to put him back inside and cDE models need to be confirmed or excluded by data.

2.6 Fluctuation dynamics and its Newtonian limit

If fluctuations are then considered, in respect to the FRW background, besides of metric fluctuations we shall have density fluctuations in the various components as well as in the DE field ϕ.

Let then be $\delta = \delta\rho/\rho$ for DM, baryons and radiative components. Radiative components will be however scarcely relevant here. Let v_i be the velocity field components for each cosmic component, and let be $\theta = \nabla_i v_i$. For both δ and θ, I shall use an index $_c$ or $_b$, to indicate DM or baryons.

A Fourier expansion of density perturbation shall be performed, in order to separate te behavior of different k–harmonics. In the equations, the wave number k will appear through the adimensional variable

$$\lambda = \mathcal{H}/k. \tag{2.26}$$

Besides of the background component, that I shall now indicate ϕ_o, the scalar field will also have a perturbation, so that $\phi = \phi_o + \delta\phi$. It is then

convenient to define the adimensional field perturbation variable

$$\varphi = \kappa\,\delta\phi/\sqrt{6}\ . \tag{2.27}$$

I shall also use the *adimensional mass* of the scalar field, defined according to

$$m_\phi = V''_\phi a/\mathcal{H} \tag{2.28}$$

Using these variables, the equations for the different components, in the conformal newtonian gauge, read:

DM

$$\delta'_c = -\theta_c + 3\psi' - 2\beta\varphi' - 2\beta'\varphi\ , \tag{2.29}$$

$$\theta'_c = -\left(1 + \frac{\mathcal{H}'}{\mathcal{H}} - 2\beta x\right)\theta_c + \lambda^{-2}(\psi - 2\beta\varphi)\ , \tag{2.30}$$

Baryons

$$\delta'_b = -\theta_b + 3\psi'\ , \tag{2.31}$$

$$\theta'_b = -\left(1 + \frac{\mathcal{H}'}{\mathcal{H}} - 2\beta_b x\right)\theta_b + c_s^2\lambda^{-2}\delta + \lambda^{-2}\psi, \tag{2.32}$$

Scalar field

$$\varphi'' + \big(2 + \frac{\mathcal{H}'}{\mathcal{H}}\big)\varphi' + (\lambda^{-2} + \hat{m}_\phi^2)\varphi - 4\psi' x - 2y^2\mu f_1\psi = \beta\Omega_c(\delta_c + 2\psi) + \frac{\varphi}{x}\Omega_c\beta'\ ,$$

Metric

$$\psi = \frac{-3\lambda^2[6x\varphi + 2x\varphi' - 2y^2\mu f_1\varphi + \sum\Omega_i(\delta_i + 3(w_i+1)\lambda^2\theta_i)]}{2(1 - 3\lambda^2(x^2 + 2y^2))}, \tag{2.33}$$

$$\psi' = \frac{1}{2}[2(3x\varphi - \psi) + \lambda^2\sum 3(w_i+1)\theta_i\Omega_i]. \tag{2.34}$$

We omit here the equations for radiation and (massive) neutrinos. Their treatment has however just the standard complications. When the Universe gradually recombines, more and more spherical harmonics of photon and ν distributions ought to be considered. In the case of massive ν, whose distribution evolution, in the configuration space, depends on momentum, also the latter variable is to be suitably sampled.

Quite in general, however, such a system of differential equations requires a numerical solution. We obtained them suitably modifying public programs, like CMBFAST and CAMB, as well as through our own program, yielding high precision results.

It is also important to consider it in the Newtonian limit, as it was used to perform n–body simulations (Macció et al 2005).

Taking a Newtonian limit means going to small scales, $\lambda << 1$. Keeping just the lowest order terms in λ, the gravitational and φ field equations then read

$$\psi = -\frac{3}{2}\lambda^2(\Omega_b\delta_b + \Omega_c\delta_c + 6x\varphi + 2x\varphi' - 2y^2 f_1\,\varphi)\ ,\quad \psi' = 3x\varphi - \psi\ , \tag{2.35}$$

$$\varphi'' + \big(2 + \frac{\mathcal{H}'}{\mathcal{H}}\big)\varphi' + \lambda^{-2}\varphi - 12x\varphi + 4\psi x + 2y^2(f_2\varphi - f_1\psi) = \beta\Omega_c(\delta_c + 2\psi). \quad (2.36)$$

Here $f_2 = \phi\frac{df}{d\phi} + 2f + f_1$. If DE kinetic (and/or potential) energy substantially contributes to the expansion source, x (and/or y) is $\mathcal{O}(1)$.

In the Newtonian limit, we must also neglect the derivatives of φ, averaging out the oscillations of φ and the potential term $f_2y^2\varphi$, requiring that $\lambda << (f_2y)^{-1}$ (remind that y is $\mathcal{O}(1)$). Furthermore, in eq. (2.36), the metric potential ψ ($\propto \lambda^2$) can also be neglected. Accordingly, eq. (2.35) and (2.36) become

$$\psi = -\frac{3}{2}\lambda^2(\Omega_b\delta_b + \Omega_c\delta_c), \quad , \quad \lambda^{-2}\varphi \simeq \beta\Omega_c\delta_c. \quad (2.37)$$

(the former one is the usual Poisson equation). If we substitute in (2.30) we can define a new potential acting on DM

$$\psi_c = \psi - 2\beta_c\varphi = -\frac{3}{2}\lambda^2\Omega_b\delta_b - \frac{3}{2}\lambda^2\Omega_c\delta_c(1 + \frac{4}{3}\beta^2)\,. \quad (2.38)$$

In real space, this equation becomes

$$\nabla^2\Phi_c = 4\pi G\rho_b\delta_b + 4\pi G^*\rho_c\delta_c\,, \quad (2.39)$$

so that $G^* = \gamma G$ with $\gamma = 1 + 4\beta^2/3$. For the velocity fields $\theta_{c,b}$ we then obtain:

$$\theta_c{}' = -\theta_c\big(1 + \frac{\mathcal{H}'}{\mathcal{H}} - 2\beta x\big) - \frac{3}{2}\big(1 + \frac{4}{3}\beta^2\big)\Omega_c\delta_c - \frac{3}{2}\Omega_b\delta_b,, \quad (2.40)$$

$$\theta_b{}' = -\theta_b\big(1 + \frac{\mathcal{H}'}{\mathcal{H}}\big) - \frac{3}{2}(\Omega_c\delta_c + \Omega_b\delta_b)\,. \quad (2.41)$$

Deriving eqs. (1.28) and (1.30) and taking the Newtonian limit ($\lambda << 1$) one can obtain a couple of equations telling us how $\delta_{c,b}$ and $\theta_{c,b}$ depend on a:

$$\delta_c{}'' = -\delta_c{}'\big(1 + \frac{\mathcal{H}'}{\mathcal{H}} - 2\beta x\big) + \frac{3}{2}(1 + \frac{4}{3}\beta^2)\Omega_c\delta_c + \frac{3}{2}\Omega_b\delta_b, \quad (2.42)$$

$$\delta_b{}'' = -\delta_b{}'\big(1 + \frac{\mathcal{H}'}{\mathcal{H}}\big) + \frac{3}{2}(\Omega_c\delta_c + \Omega_b\delta_b), \quad (2.43)$$

Assuming $\Omega_b << \Omega_c$ and putting $\delta_c \propto e^{\int \eta(\alpha)d\alpha}$ and $\delta_b = b\delta_c$ with $b = cost$ from the eqs.(2.42), (2.43), we obtain the bias factor

$$b = \frac{\delta_b}{\delta_c} \simeq \frac{3\Omega_c}{3\gamma\,\Omega_c + 4\beta\,x\eta}\,. \quad (2.44)$$

The acceleration of a single DM or baryon particle of mass $m_{c,b}$ can be instead derived from eqs. (2.40), (2.41). Let us set it in the void, at a distance r from the origin, where a DM (or baryon) particle of mass M_c (or M_b) is set, and let us remind that, while the usual scaling $\rho_b \propto a^{-3}$ holds, it is

$$\rho_c = \rho_{oc}a^{-3}e^{-\int C(\phi)d\phi}, \quad \rho_{M_c} = M_{oc}a^{-3}e^{-\int C(\phi)d\phi}\delta(0), \quad (2.45)$$

because of the DE-DM coupling (here the subscript o indicates values at the present time τ_o (it is $a_o = 1$)). We can then assign to each DM particle a varying mass $M_c(\phi) = M_{oc} e^{-\int C(\phi) d\phi}$

Then, owing to eq. (2.45), and assuming that the density of the particle widely exceeds the background density, it is

$$\Omega_c \delta_c = \frac{\rho_{M_c} - \rho_c}{\rho_{cr}} = \frac{8\pi G}{3\mathcal{H}^2 a} M_c(\phi)\delta(0) \ , \quad \Omega_b \delta_b = \frac{\rho_{M_b} - \rho_b}{\rho_{cr}} = \frac{8\pi G}{3\mathcal{H}^2 a} M_b \delta(0), \tag{2.46}$$

(ρ_{cr} is the critical density and δ is the Dirac distribution). Reminding that $\nabla \cdot \mathbf{v}_{c,b} = \theta_{c,b}\mathcal{H}$ and using the ordinary (not conformal) time, eq. (2.42) yields

$$\nabla \cdot \dot{\mathbf{v}}_c = -H(1 - 2\beta x)\, \nabla \cdot \mathbf{v}_c - 4\pi G a^{-2} \left(\gamma M_c(\phi) + M_b\right) \delta(0) \tag{2.47}$$

(dots yield differentiation in respect to ordinary time and $H = \dot{a}/a$). Taking into account that the acceleration is radial, as the attracting particles lie at the origin, it will be

$$\int d^3 r\, \nabla \cdot \dot{\mathbf{v}} = 4\pi \int dr\ d(r^2 \dot{v})/dr = 4\pi r^2 \dot{v}.$$

Accordingly, the radial acceleration of a DM particle read

$$\dot{v}_c = -(1 - 2\beta x) H \mathbf{v}_c \cdot \mathbf{n} - \frac{G^* M_c(\phi)}{R^2} - \frac{G M_b}{R^2}, \tag{2.48}$$

($\mathbf{n}$ is a unit vector in the radial direction; $R = ar$). Repeating the calculation for a baryon we get immediately the result

$$\dot{v}_b = -H \mathbf{v}_b \cdot \mathbf{n} - \frac{G M_c(\phi)}{R^2} - \frac{G M_b}{R^2} \tag{2.49}$$

In eq. (2.48) the three effects of the coupling appear clearly: the masses of DM particles depend on the time evolution of ϕ; their variation induces an extra friction $-2\beta x$ in the equation of motion (2.48); a different gravity is felt by DM with respect to baryons.

The dimensionless constant β^2 yields the ratio between the DM–DM gravitational constant and usual gravity:

$$G^* = G\left(1 + \frac{4\beta^2}{3}\right) \ . \tag{2.50}$$

In fact baryons, which remain uncoupled (or very weakly coupled) to DE, keep the usual gravitational behavior. G^* holds just for interactions between DM particles, whose motions violate the equivalence principle, although this is unobservable with local experiments.

Chapter 3

Softening limits on neutrino mass through DM–DE coupling

Cosmological limits on neutrino masses are softened, by more than a factor 2, if Dark Matter and Dark Energy are coupled. In turn, a neutrino mass yielding Ω_ν up to ~ 0.20 allows coupling levels $\beta \simeq 0.15$ or more, already slightly easing the coincidence problem. The coupling, in fact, displaces both $P(k)$ and C_l spectra in a fashion opposite to neutrino mass. Tentative estimates are obtained through a Fisher–matrix technique and typical examples are obtained by exploring the parameter space.

The results described here are refered in part to a paper published by the author [61].

3.1 Introduction

There seem to be little doubt left: at least one neutrino mass eigenstate or, possibly, two of them exceed $\simeq 0.055$ eV (direct or inverse hierarchy). This follows solar [62] and reactor [63] neutrino experiments, yielding $\Delta m^2_{1,2} \simeq 8 \times 10^{-5}\mathrm{eV}^2$ and, namely, atmospheric [64] and accelerator beam [65] experiments yielding $\Delta m^2_{2,3} \simeq 3 \times 10^{-3}\mathrm{eV}^2$.

Cosmology is also sensitive to neutrino mass. Valdarnini & Bonometto (1984) [66] made a detailed analysis of transfer functions in cosmologies where a part of Dark Matter (DM) is due to massive neutrinos, so proposing mixed DM models, where neutrinos play an essential role in adjusting CMB (Cosmic Microwave Background) anisotropies and matter fluctuation spectra to fit observations. A large deal of work on this subject took place in the Nineties; mixed models were widely tested, using both the linear and the non–linear theory.

Hubble diagram of SNIa [67] showed then an accelerated cosmic expansion, while advanced data on CMB [68] and large scale structure [69] required a *spatially flat* cosmology with a matter density parameter $\Omega_{o,m} \simeq 0.27$, so that

the gap up to unity was to be filled by a smooth non–particle component dubbed Dark Energy (DE).

All that relegated neutrinos to a secondary role in shaping cosmic data while, by using such advanced astrophysical data, increasingly stringent limits on neutrino masses could be computed (see, *e.g.* [70])

Standard limits on neutrino masses were recently summarized by Komatsu et al (2008) [71], within the WMAP5 release, and are quoted in Table 3.1. More stringent but more speculative limits are suggested in [72], who make a more extensive use of SDSS or 2dF data, and in [73], by using Lyα forest data.

These limits, clearly, rely on implicit assumptions concerning the dark cosmic sector, whose knowledge still fully relies on astrophysical data, requiring two components characterized by state parameters $w \simeq 0$ and $\simeq -1$. But the assumption that no energy exchange between them occurs, tested vs. data, leads just to coupling limits.

As we showed in Chapter 2, a large deal of work dealt with the coupling option, in the attempt to overcome the *coincidence* paradox. All that makes our epoch unique and, unless one indulges to *anthropic* views, apparently requires an explanation. However, also indipendently from this conceptual issue, our very ignorance of the physics of the dark sector requires that all reasonable options consistent with basic physics and data are explored.

It is also important to outline that neutrino mass limits can be softened if DE with a state parameter $w < -1$ is considered [74]. Unfortunately, this kind of state equations, yielding the so–called *phantom–DE*, can be justified only making recourse to unconventional physics.

In this section we show that spectral distortions due to DM–DE coupling and to neutrino mass tend to compensate. We tentatively estimate how far we can go, simultaneously increasing coupling and mass, by using a Fisher Matrix (FM) technique. On that basis we perform a preliminary exploration of the parameter space, substantially confirming FM findings.

3.2 Some angular and linear spectra

The point of this paper can be appreciated through the spectra in Figures 3.1 and 3.2. We compare a model with zero coupling and zero neutrino mass (00–model, hereafter) with: (i) a model with 2 massive neutrinos with mass $m_\nu = 0.119\,\mathrm{eV}$, yielding $\Omega_\nu = 0.005$ (plus 1 massless neutrino); (ii) a model with a DM–DE coupling $\beta = 0.049$; (iii) a model with both neutrino mass and

Table 3.1: Summary of the 2–σ (95% C.L.) constraints on the sum of ν masses, from WMAP 5-year and other cosmological data sets.

	$w = -1$	$w \neq -1$
WMAP5	< 1.3 eV	< 1.5 eV
WMAP5+BAO+SN	< 0.67 eV	< 0.80 eV

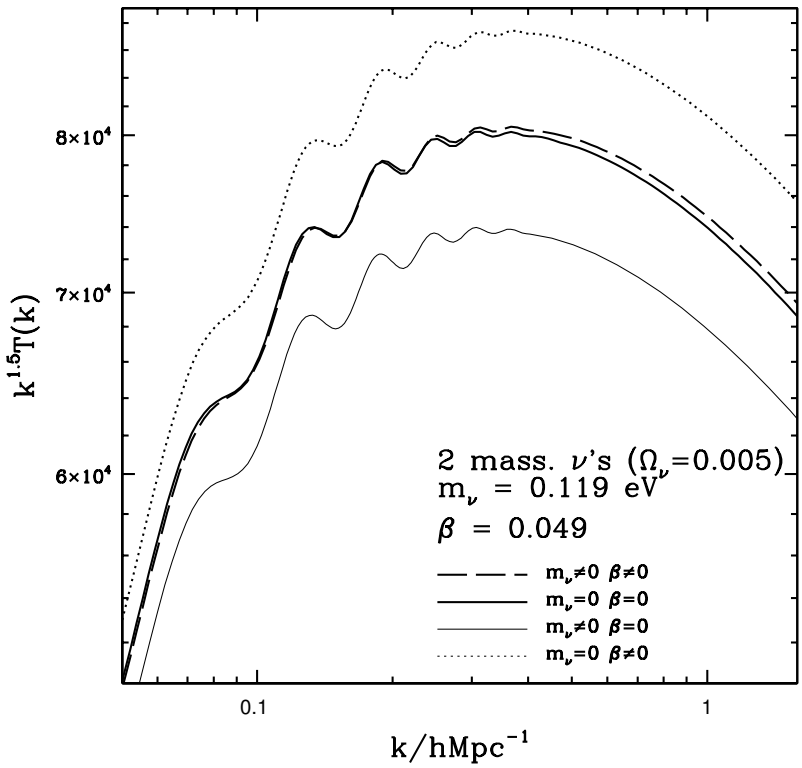

Figure 3.1: Transfer functions in cosmologies with/without coupling and with/without 2 massive neutrinos. Coupling and mass are selected so to yield an approximate balance. The functions are multiplied by $k^{1.5}$, to help the reader to distinguish different cases.

coupling (CM–model, herafter). All models are spatially flat, have adimensional Hubble parameter $h = 0.71$, density parameters $\Omega_b = 0.04$, $\Omega_{de} = 0.73$, spectral index $n_s = 0.96$ and a cosmic opacity $\tau_{opt} = 0.089$. DE is due to a SUGRA potential with $\Lambda = 1.1\,\mathrm{GeV}$, fitting WMAP and other data at least as well as a ΛCDM.

Angular and spatial spectra are computed with an extension of the program CAMB, allowing to treat coupled DE models also in the presence of massive neutrinos.

Both l and k ranges are selected for being those physically most significant. At lower l's model discrepancies essentially vanish. In the l region shown, we have the sequel of maxima and minima due to primeval compression waves. The k range covers the scale explored by deep samples, as 2dF or the SLOAN digital survey, up to k values where non–linear effects become important.

In the plots, spectra are multiplied by suitable powers of the abscissa l or k, so to reduce the ordinate range. In spite of that, in the C_l plot different spectra are not easy to distinguish. We then plot also the ratio $\Delta C_l/C_l$ at constant l; shifts would however appear even smaller if slight shifts along the l axis (by 1 or 2 units) were performed.

The Figures are principally meant to show that the effects of neutrino

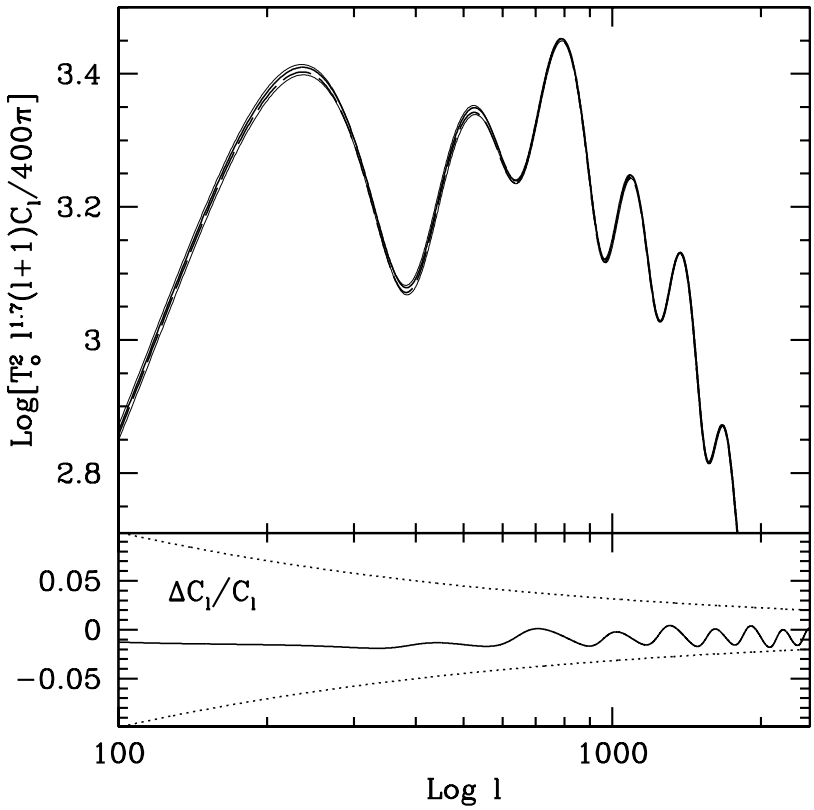

Figure 3.2: Angular anisotropy spectra for the same models of the previous figure. Due to intrinsic C_l oscillations, this Figure is slightly harder to read. In the lower frame we also give the spectral differences between 00– and CM–models. Large l oscillations could be further damped by a shift by 1 or 2 units along l. The dotted lines represent the cosmic variance interval.

mass and coupling are opposite. The coupling intensity, in fact, is selected so to (approximately) balance neutrino masses.

We took, however, $\sum m_\nu \ll 0.61$ and $\beta \ll 0.075$ (see Amendola 1999, Amendola & Quercellini 2000, Macciò et al 2004); each of these values, by itself, is within current observational limits. Accordingly, even the difference between thin and thick solid–line spectra cannot be appreciated through current data.

In particular, let us outline how the BAO (baryonic acoustic oscillation) structure is faithfully reproduced when passing from the 00–models (thick solid line) to the CM–models (thick dashed line).

3.3 Fisher matrix

We then aim to test how far we can go, simultaneously increasing β and Ω_ν, without conflicting with data. This can be estimated by using a FM analysis [75, 76, 77] (see App. A.1).

This approach allows a rapid, semi–analytic estimate of the confidence limits for a specific experiment. It assumes a reference model as the most probable one, *i.e.* as the maximum of the likelihood distribution $\mathcal{L}(\vec{x}|\vec{\theta})$ of the data system $\vec{x}$ given the model, described by parameters $\vec{\theta} \equiv (\theta_i)$. Exploiting this hypothesis, one can approximate $\mathcal{L}$ by a multivariate Gaussian distribution, built using its second derivatives in respect to the parameters $(\bar{\theta}_i)$ at the reference model. Nevertheless, as is known, this technique is limited by the actual non–Gaussian behavior of data.

3.3.1 Data and technique

In the literature, cosmological models are constrained by using a large number of observables. To our present aims we shall directly consider the spectrum of matter fluctuations $P(k)$ and the CMB angular spectra C_l^{XY} ($XY = TT, TE, EE$). In their recent analysis, Komatsu et al (2008) made a more restricted use of $P(k)$, using only BAO's, while they used SNIa Hubble diagrams, so significant also for being the first signal of DE.

Here we chose observables directly coming from the model, in the attempt to leave apart observational biases, focusing just on the level of sensitivity of possible experiments. We consider then two different experimental contexts. The first one assumes that CMB spectra are measured at WMAP sensitivity and $P(k)$ is measured with the sensitivity of the 2dF experiment (case W). The second assumes Planck sensitivity for CMB spectra and SDSS sensitivity for $P(k)$ (case P). The observational features for each mission considered are listed in Table 3.2 for the case of CMB experiments and in Table 3.3 for the galaxy surveys.

Table 3.2: WMAP and PLANCK mission specifications used in the paper.

Mission	l_{max}	f_{sky}	θ_{FWHM}	σ_T	σ_P
WMAP	1000	0.8	13'	260	500
PLANCK	2500	0.8	7.1'	42	80

Table 3.3: 2dF and SDSS–like mission specifications used in the paper. Scales and volumes are in Mpc/h and $(\mathrm{Mpc/h})^3$, respectively.

Mission	k_{min}	k_{max}	Volume
2dF	0.02	0.1	10^8
SDSS	0.02	0.15	0.72×10^9

Let us now consider first the use of CMB data only and let C_l^{XY} be the angular spectra of the input model, to which we must add a white noise signal, to obtain

$$\bar{C}_l^{XY} = C_l^{XY} + N_l^{XY} \qquad \text{with} \qquad N_l^{XY} = \delta_{XY}\sigma_X^2 \exp\left[l(l+1)\frac{\theta_{FWHM}^2}{8\ln 2}\right] . \quad (3.1)$$

The expressions of the Fisher matrix F_C^{ij} components are then obtainable according to the relation

$$F_C^{ij} = \sum_l \sum_{XY,X'Y'} \frac{\partial}{\partial\theta_i} C_l^{XY} [\mathrm{Cov}_C^{-1}]_l^{XYX'Y'} \frac{\partial}{\partial\theta_j} C_l^{X'Y'} \quad (3.2)$$

with

$$[\mathrm{Cov}_C]_l^{XY,X'Y'} = \frac{1}{(l+1/2)f_{sky}} \begin{pmatrix} (\bar{C}_l^{TT})^2 & (C_l^{TE})^2 & C_l^{TE}\bar{C}_l^{TT} \\ (C_l^{TE})^2 & (C_l^{EE})^2 & C_l^{TE}\bar{C}_l^{EE} \\ C_l^{TE}\bar{C}_l^{TT} & C_l^{TE}\bar{C}_l^{EE} & \frac{1}{2}[(C_l^{TE})^2 + \bar{C}_l^{TT}\bar{C}_l^{EE}] \end{pmatrix} . \quad (3.3)$$

On the contrary, when dealing with matter power spectra, we used the following definition for the FM [78]

$$F_P^{ij} = \sum_{\alpha,\beta} \frac{\partial}{\partial\theta_i} P(k_\alpha) [\mathrm{Cov}_P^{-1}]_{\alpha\beta} \frac{\partial}{\partial\theta_j} P(k_\beta) \quad (3.4)$$

with

$$[\mathrm{Cov}_P]_{\alpha\beta} \simeq \delta_{\alpha\beta} \frac{V_f}{V_s(k_\alpha)} 2P^2(k_\alpha) , \quad (3.5)$$

where $V_f = (2\pi)^3/V$ is the volume of the foundamental cell in k space, V is the volume of the survey and $V_s(k_\alpha) = 4\pi k_\alpha^2 \delta k$ is the volume of the shell of width δk centered on k_α [79, 80]. In eq.(3.5) we left aside the contribution of the trispectrum, because in our analysis we considered only the linear scales, where the trispectrum is negligible.

The cosmological model we consider is characterized by 9 parameters: $\omega_b = \Omega_\mathrm{b} h^2$, $\omega_c = \Omega_\mathrm{c} h^2$ density parameters for baryons and CDM, respctively, H_0 Hubble parameter, A_s scalar fluctuation amplitude, n_s spectral index, τ_opt cosmic opacity to CMB photons, $\mathrm{Log}(\Lambda)/\mathrm{GeV}$ logarithm of the energy scale in SUGRA potential, β DM–DE coupling parameter, $\sum m_\nu/\mathrm{eV}$ sum of neutrino masses. We estimate the neutrino mass density parameter, $\Omega_\nu h^2$, converting it from the total neutrino mass via

$$\Omega_\nu h^2 = \frac{\sum m_\nu}{93.5\ \mathrm{eV}} . \quad (3.6)$$

We compute the CMB anisotropies (temperature and polarisation) power spectra and the transfer functions, used to calculate linear matter power spectrum, using a modified version of the public available code CAMB[1]. Numerical derivatives were evaluated considering a 5% stepsize, except for Λ, where we adopted a 5% stepsize on $\lambda \equiv \mathrm{Log}(\Lambda/\mathrm{GeV})$.

[1] http://www.camb.info/

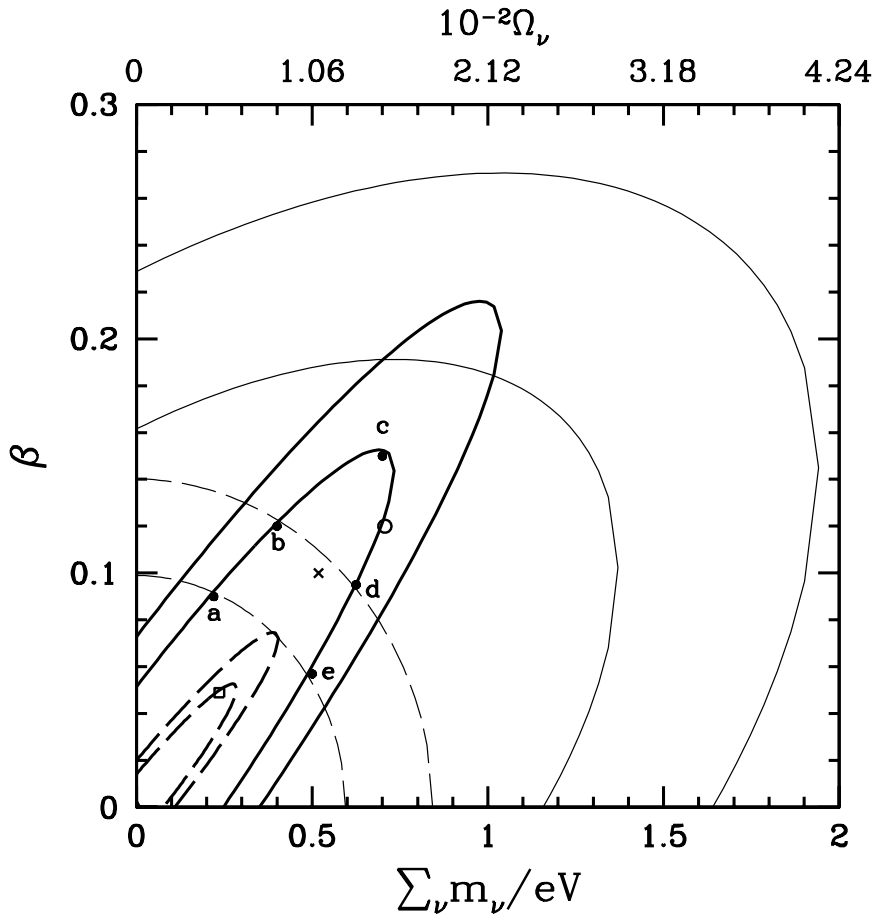

Figure 3.3: 1– and 2–σ confidence levels for a 2–massive–neutrino model, assuming that the true cosmology is a SUGRA model with $\log(\Lambda/\mathrm{GeV}) = 1.1$, while $\beta = 0$ and $\Omega_\nu \simeq 0$. Thick (thin) curves show the constraints deriving from CMB and deep sample data (from CMB data only). Solid curves refer to the (i) case (WMAP+2dF). Dashed curves refer to the (ii) case (PLANCK+SDSS). In the sequel we shall examine in detail models corresponding to the points labeled a, b, c, d, e and others. The location of the CM–model of Figs. 3.1 and 3.2 is indicated by an open box. The two locations indicated by an open circle and a cross will also be considered in detail below. This Figure is somehow analogous to Fig. 2 in Hannestad, 2005.

3.3.2 Results

In Figure 3.3 we then report the expected 1– and 2–σ likelihood curves on the $\sum m_\nu$–β plane, for both cases W and P. In either case we analyse the constraints coming just from CMB data and those arising from the joint exploitation of CMB and deep sample data. We performed the analysis either assuming 3 equal mass neutrinos, or 1 massless and 2 massive neutrinos. The plots shown in the Figure are obtained for the latter case, but discrepancies are just a minor effect.

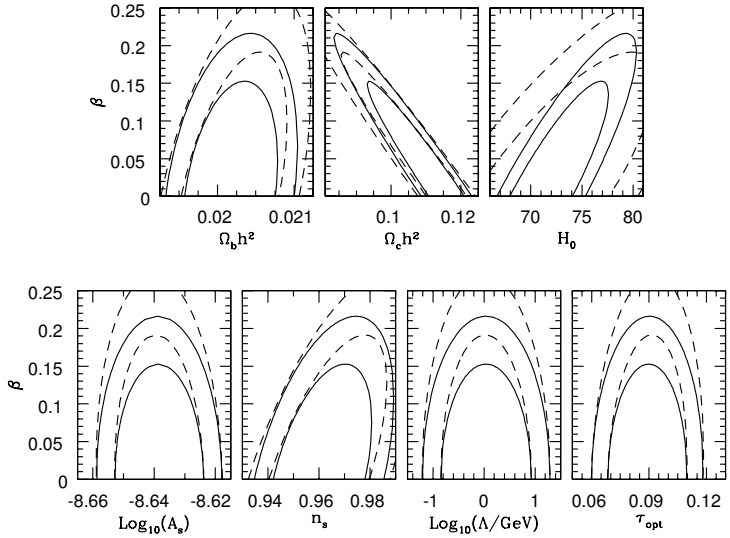

Figure 3.4: Correlation between β and the other model parameters for the W case (WMAP+2dF); dashed lines refer to CMB data only.

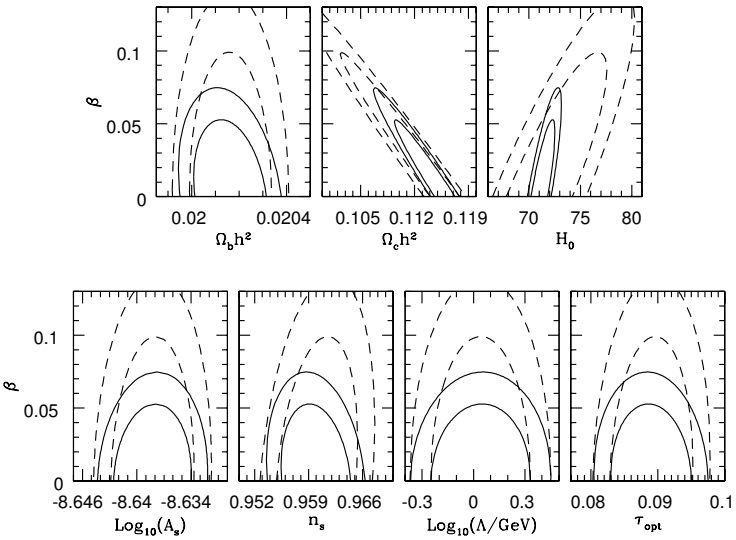

Figure 3.5: Correlation between β and the other model parameters for the P case (PLANCK+SDSS); dashed lines refer to CMB data only.

The Fisher–matrix results, for the W case, substantially confirms known 1– and 2–σ limits on β, yielding $\beta < 0.05$ and $\beta < 0.075$, respectively, along the β axis (*i.e.* with $\sum m_\nu = 0$).

On the other axis, with $\beta = 0$, $\sum m_\nu$ seems to be more constrained than what we know from current limits ($\sum m_\nu < 0.35$ vs. $\sum m_\nu < 0.8$ with $w \neq -1$). These discrepancies can be read as an indication of the level or reliability that Fisher–matrix estimate can have. In particuilar, they may be partially due to the impact of using the whole $P(k)$ information, as well as to the fact that the reference cosmology is SUGRA instead of ΛCDM. However, the CMB

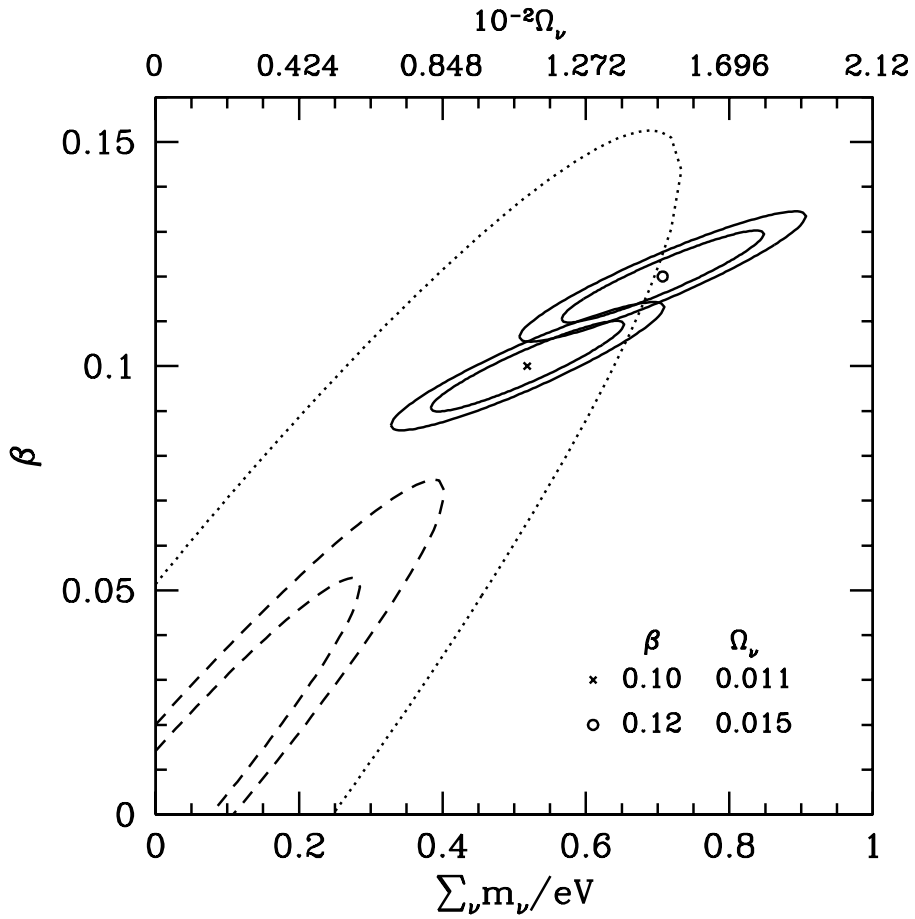

Figure 3.6: 1– and 2–σ limits, for the P–case, assuming that the true cosmology corresponds to the points marked by cross or open circle. The dashed lines report the same limits around the 00–model, as shown in Fig. 3.3; similarly, the dotted line is the 1–σ limit around the 00–model in the W–case, as shown in Fig. 3.3. This Figure shows that cosmologies, comprising DM–DE coupling and neutrino masses, presently compatible with the 00 option, will be easily discriminated, at the P sensitivity level.

2–σ constraint we find, $\sum m_\nu < 1.65$, is close to the 95 % confidence limit $\sum m_\nu < 1.5$ obtained through a full MonteCarlo analysis of WMAP data only, with $w \neq -1$.

The likelihood plots have the expected shape. Taken at face value they yield upper limits $\beta \lesssim 0.22$ and $\sum m_\nu \lesssim 1.05$ eV , in the case W. With the value of H_o used here this would correspond to $\Omega_\nu \simeq 0.022$, almost 2/3 of baryon density.

On the contrary, in the case P, constraints are more severe, as only CM–models with $\beta < 0.07$ and $\sum m_\nu < 0.4$ appear consistent with the 00–model, at the 2–σ level. These limits are close to the maximum coupling and neutrino mass separately admitted in the present observational constraints.

In Figure 3.4 we also show the correlations between β and the whole set of

parameters considered, in the W case. Correlations can be considered negligible for the parameters A_s, n_s, Λ, τ_{opt} . The correlations with the parameters ω_c, ω_b, H_o, as expected, are stronger.

Figure 3.5 yields analogous results for the P case. The same comments here above hold for this case, just within the more constrained intervals allowed.

It may also be useful to consider Figure 3.6, showing that models, including DM–DE coupling and neutrino masses, compatible with the 00 option at the W sensitivity level, at the P sensitivity level will be well discriminated from it and between them.

3.4 Exploring the parameter space

A further insight into FM results can be gained by considering a few examples. In Figures 3.7 and 3.8 we exhibit the spectra for a set of models. As shown in the frame of Fig. 3.7, the models yielding the maximum DM–DE coupling (and vanishing ν mass) or the maximum neutrino mass (and vanishing coupling) have the thick line spectra. Model discrepancy is enhanced by taking the same amplitude A_s, instead of normalizing them to the same σ_8.

The setting of models *a, b, c, d, e* on the $\sum m_\nu$–β plane is indicated in Fig. 3.3. They are all on the 1–σ boundaries. The best performance, perhaps, can be ascribed to models *d* and *e*. Both of them yield a present hot dark matter density exceeding 1 % of the critical density and 5 % of the whole DM.

3.5 Conclusions

In this section we performed a first inspection on the possibility that high ν masses and DM–DE coupling yield compensating distortions of matter fluctuations and CMB spectra. This compensation is highly effective for small masses and couplings, as shown in Figs. 3.1 and 3.2. We then address the most significant question concerning the limits on coupling and ν masses, when simultanously considered.

This question should be carefully addressed by using MonteCarlo techniques and considering all available observational constraints. Unfortunately, to do so, we should widen the usual parameter space, by adding 3 extra degrees of freedom: the coupling parameter β, neutrino mass, and the energy scale Λ in the SUGRA model (or another equivalent parameter, in the same or in another dynamical DE potential).

This is among the reasons that led previous authors to perform a preliminary test by using a Fisher matrix technique. Here we implemented such test by exploring the parameter space under the guide of Fisher matrix outputs. We reserve the MCMC analysis for a future work.

Taking Fisher matrix outputs at face value leads to state that models with $\Omega_\nu \lesssim 0.022$ and $\beta \lesssim 0.22$ are observationally consistent with a $\Omega_\nu = 0$ and

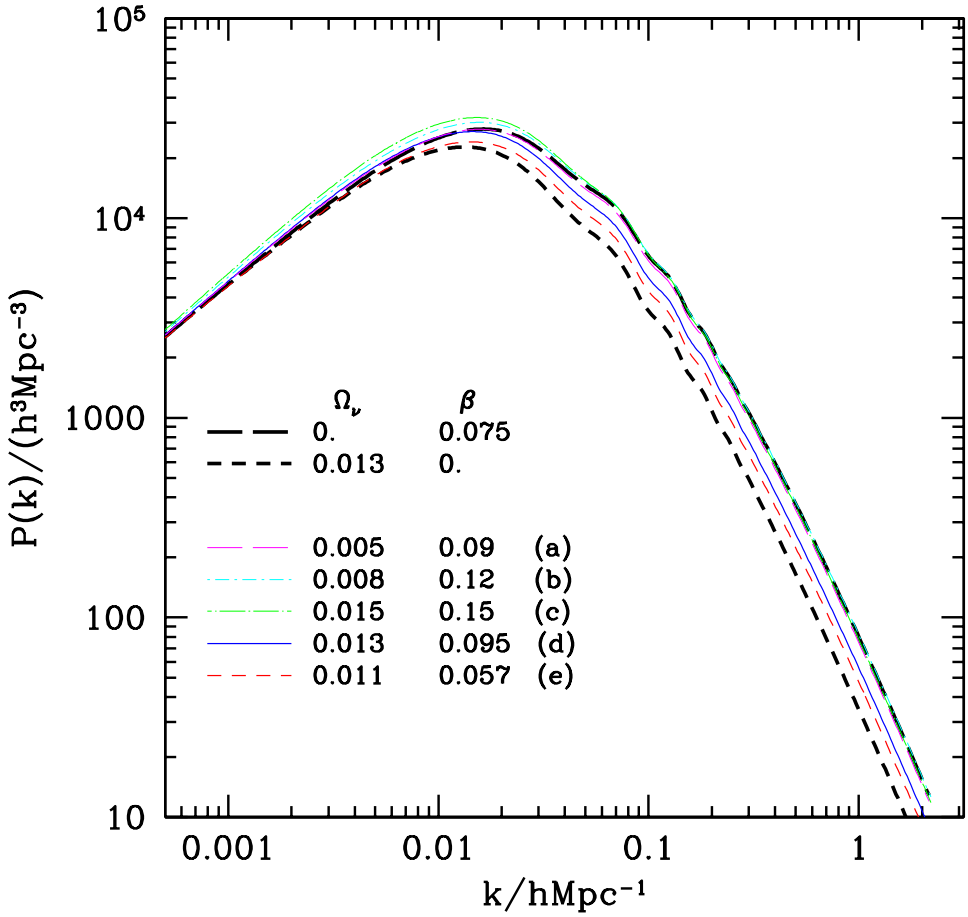

Figure 3.7: Spectra for a number of cosmologies. All of them are obtained setting $n_s = 0.96$ and $\log A_s = -8.64$, so to enhance model differences. Thick lines correspond to models presently considered in agreement with data, and yielding maximum values either for $\sum m_\nu$ or β. The other lines yield models corresponding to the points *a, b, c, d, e* in Fig. 3.3, consistent with the 00–model at the 1–σ level.

$\beta = 0$ model. We then directly explored the parameter space and confirmed that a model with $\Omega_\nu \simeq 0.015$ and $\beta \simeq 0.1$ appears in fair agreement with the observables considered. Direct inspection on $\Omega_\nu \sim 0.022$–$\beta \sim 0.22$ is not so satisfactory.

This just confirms the expected limits of the Fisher matrix technique, but we do expect similar values to be in agreement with the present observations if the whole parameter set is suitably tuned. This "extreme" regime will be easily falsified by experiments with a sensitivity comparable with PLANCK and SDSS, as Figure 3.6 shows.

In turn, such experiments could lead to a safe detection of neutrino masses widely exceeding microphysical data from flavor mixing. A mass range yielding $\Omega_\nu \sim 0.02$ would mean that hot DM is $\sim 10\,\%$ of the DM total, so that its effects significantly contribute to shaping large scale structure, as in old mixed

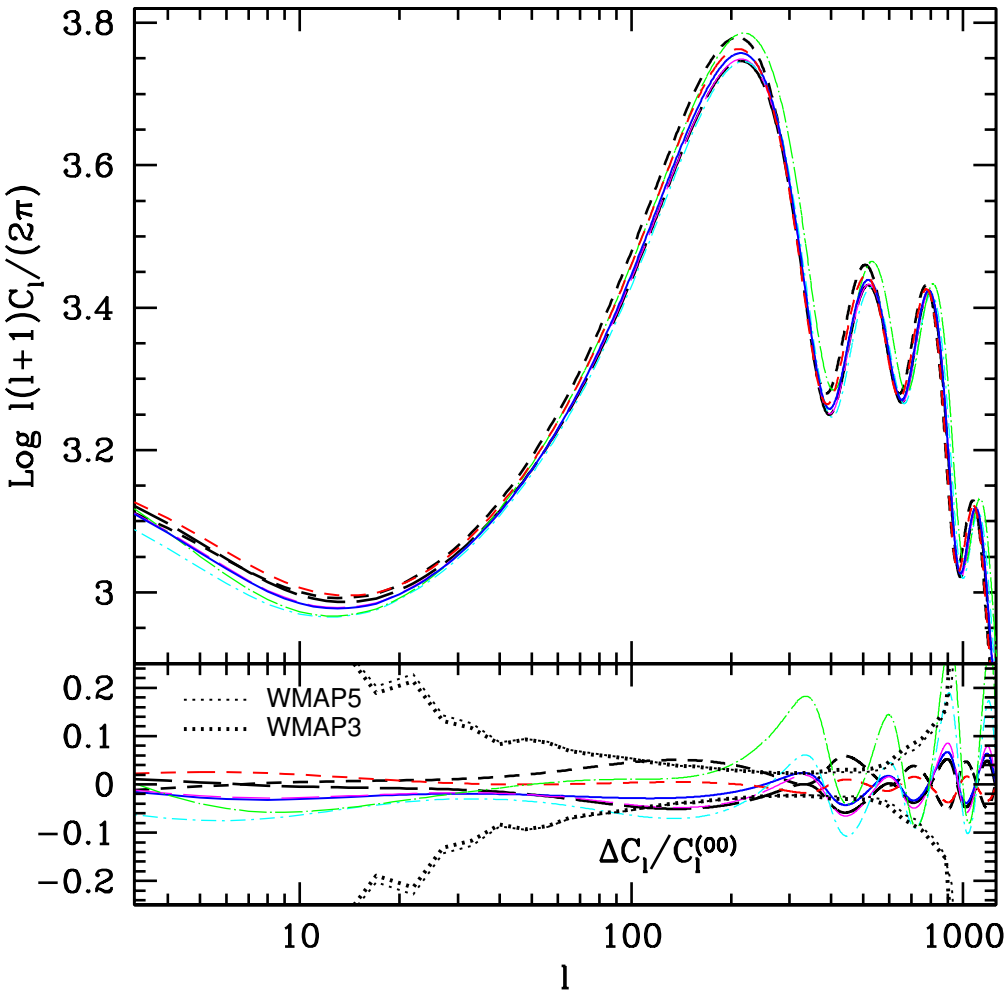

Figure 3.8: Spectra of CMB anisotropies for the same cosmologies of Fig. 3.7, compared with WMAP error amplitudes. Let us remind that all of them are obtained keeping the same values $n_s = 0.96$ and $\log A_s = -8.64$, so to enhance model differences. The relative difference of the thick line models from the 00–model appears not so wide as for some of the other models. Among them, however, the solid and dashed line models seem to perform quite well. Their performance can be improved by adjusting the H_o value, slightly modifying Fisher matrix outputs.

matter models.

Such "extreme" models would also achieve another important result. Models with cDE were initially considered to overcome the *coincidence* problem, in the presence of DE. In Figure 3.9, we show the scale dependence of the density parameters, for various models with different $\sum m_\nu$ and β.

In the usual case, with negligible m_ν, a DM–DE coupling compatible with data hardly eases the coincidence problem. Such easing is represented by the *plateau* in the Ω_{de} curve, whose proportions are then almost unsignificant. This does not mean that $\beta \neq 0$ is not to be considered among the possible degrees

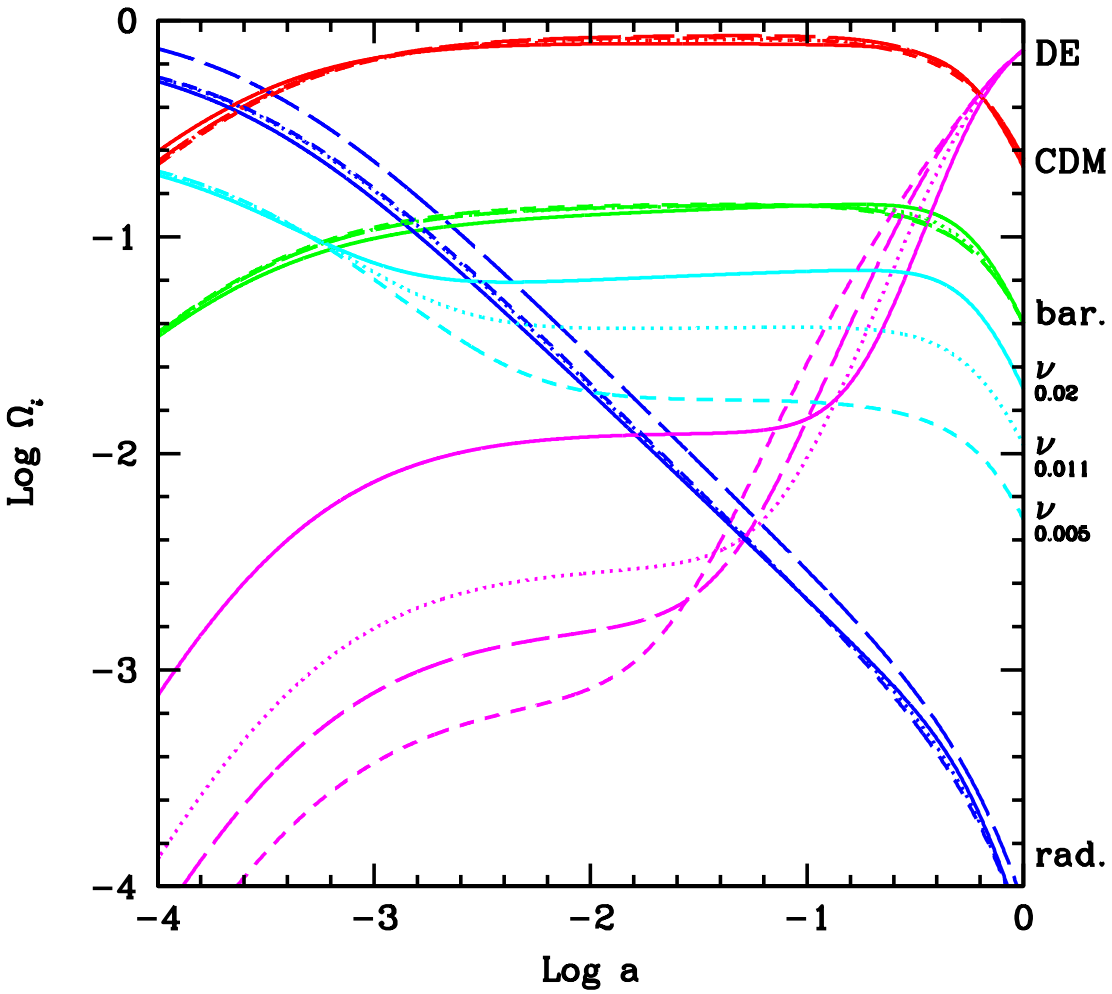

Figure 3.9: Density parameters for cold DM, hot DM (ν's), DE and radiation in models with Ω_ν and β taking the values 0.005–0.049 (short dashed), 0–0.07 (long dashed), 0.011–0.1 (dotted), 0.02–0.21 (solid), respectively. In the last case, the DE plateau, extending up to the equatlity redshift, uccurring slightly above $z \sim 10^3$, shows a DE density keeping $\sim 1/20$ of cold DM.

of freedom; *e.g.*, Vergani et al. (2008) have shown that a cosmology with β as small as ~ 0.05, if inspected assuming $\beta \equiv 0$, can yield badly wrong values for some cosmic parameters, including ω_{oc}. Figure 3.9 however indicates that, when $\beta \sim 0.02$ is recovered, in the presence of suitably massive ν's, a significant *plateau* is present and DE density keeps at the level $\sim$ 1–2 % of the critical density up to $z \sim 10^3$.

Chapter 4

Weak Lensing properties

Weak gravitational lensing directly probes matter distribution, through its gravitational potential, and, in principle, does so in any celestial site, requiring no peculiar distribution of cosmic objects. Matter distribution, then, is much more directly related to theoretical predictions than light distribution. In this chapter I develop some of the formalism used to reconnect this phenomenon to theory.

4.1 Basics of gravitational lensing

Light rays are deflected by any gravitational field. Deflection becomes observable if produced by quite a massive body. The possibility of light deflection had been suspected since 1704, by Newton in the first edition of his *Opticks*. This idea was subsequently pursued, in the context of a corpuscular theory of light using Newton's law of gravitation, by Cavendish (1784), Laplace (1796), and Soldner (1801). After Maxwell electro–magnetic unification, light wave deflection could also be confirmed. Nevertheless, General Relativity (GR) put lensing on a firm theoretical footing, and yields twice the Newtonian value for the deflection angle [81]. The agreement of this prediction with the deflection of light from distant stars by the Sun, claimed for the solar eclipse of 1919 [82], was considered a great success for Einstein's theory and brought General Relativity to the general attention. More recent experiments safely confirmed such early output.

According to GR, light propagates along the null geodesics and, for almost all relevant observational cases, we can assume that the overall geometry of the Universe is described by FRW metric and that matter inhomogeneities causing lensing are no more than local perturbations.

4.1.1 Deflection of light rays

Accordingly, we can assume a locally flat, Minkowskian space-time, weakly perturbed by the Newtonian gravitational potential Φ ($|\Phi| \ll c^2$) of the mass distribution constituing the lens. In this scheme, the effect of the space-time curvature on the light paths can be represented as the analogous of the effect of a prism, defining an effective index of refraction n, which is given by (e.g. [83])

$$n = 1 - \frac{2}{c^2}\Phi = 1 + \frac{2}{c^2}|\Phi| \; . \tag{4.1}$$

As in the case of the prism, the deflection is the integral along the light path of the gradient of n perpendicular to the light path, *i.e.*:

$$\vec{\alpha} = -\int \vec{\nabla}_\perp n \, dl = \frac{2}{c^2} \int \vec{\nabla}_\perp \Phi \, dl \; . \tag{4.2}$$

In all cases of interest the deflection angle $\vec{\alpha}$, a 2–vector on the celestial sphere, is small. We can therefore simplify its evaluation by integrating $\vec{\nabla}_\perp n$ along an unperturbed light ray with its very impact parameter, instead of following in detail the deflected ray (this corresponds to a Born approximation; the difference from a complete computation is $\sim \mathcal{O}(\alpha^2)$). As an example, for a point mass M, we obtain then

$$\vec{\alpha} = \frac{2}{c^2} \int \vec{\nabla}_\perp \Phi \, dz = \frac{4GM}{c^2} \frac{\vec{\xi}}{|\vec{\xi}|^2} \; , \tag{4.3}$$

twice the value obtainable in Newtonian gravity. Here $\vec{\xi}$ is the impact parameter of the unperturbed light ray, being a vector in the plane orthogonal to the light path, while the coordinate z is an affine parameter along the light ray. Equation (4.3) yields no dependence on z. The fact that the deflection angle does not depend on the longitudinal extension of the lens still holds in the extended lens case. A mass distribution for which this condition is satisfied is called *geometrically-thin lens*.

In the weak limit, GR field equations can be linearized. Hence, the deflection angle of a set of mass points δm_i set in points of coordinateds $\vec{\xi}_i$ and z_i is the (vectorial) sum of the deflections due to each δm_i. In the same way, if $\rho(\vec{\xi}, z)$ is a three-dimensional mass density distribution and $\mathrm{d}m = \rho(\vec{\xi},z)\,\mathrm{d}V$ the mass in the volume element $\mathrm{d}V$; the total deflection angle then reads

$$\begin{aligned} \vec{\alpha}(\vec{\xi}) &= \frac{4G}{c^2} \sum_i \delta m_i \, \frac{\vec{\xi} - \vec{\xi}_i}{|\vec{\xi} - \vec{\xi'}_i|^2} \\ &= \frac{4G}{c^2} \int \mathrm{d}^2\xi' \int \mathrm{d}z \; \rho(\vec{\xi'}, z) \, \frac{\vec{\xi} - \vec{\xi'}}{|\vec{\xi} - \vec{\xi'}|^2} \; . \end{aligned} \tag{4.4}$$

If one then defines the *surface mass density*

$$\Sigma(\vec{\xi}) \equiv \int \mathrm{d}z \; \rho(\vec{\xi}_1, \vec{\xi}_2, z) \; , \tag{4.5}$$

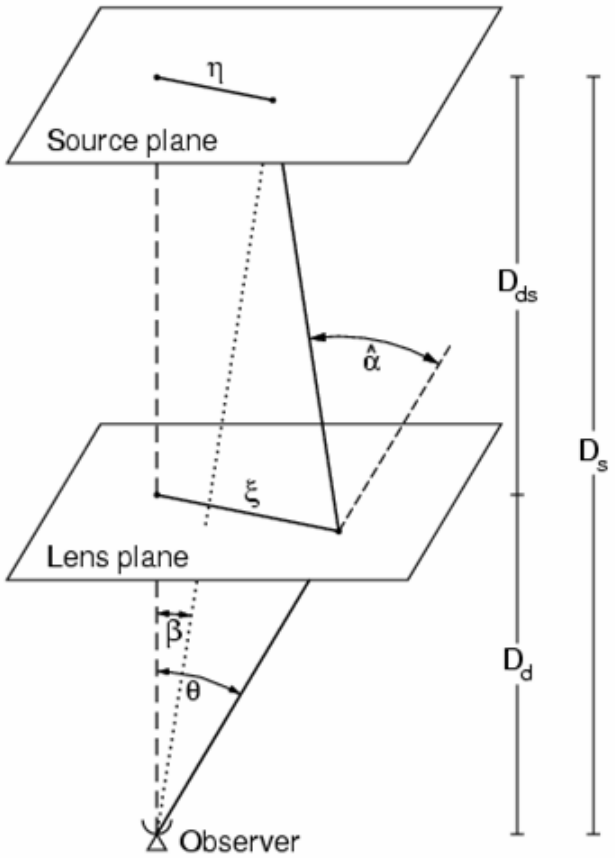

Figure 4.1: Sketch of a typical graviational lens system.

i.e., the mass density projected onto the celestial sphere, then an arbitrary density distribution yields a deflection angle

$$\vec{\alpha}(\vec{\xi}) = \frac{4G}{c^2} \int \mathrm{d}^2\xi' \, \Sigma(\vec{\xi}') \, \frac{\vec{\xi} - \vec{\xi}'}{|\vec{\xi} - \vec{\xi}'|^2} \, , \tag{4.6}$$

indipendent from the lensing mass distribution along z. This is a consequence of neglecting terms $\mathcal{O}(\alpha^2)$ and is true if the deviation from a straight (undeflected) line, within the mass distribution, is small compared to the angular scale on which the mass distribution has significant changes. This condition is however satisfied in most astrophysical cases.

4.1.2 The lens equation

The geometry of a typical gravitational lens system is shown in Fig. 4.1. A light ray from a source at redshift z_s (or distance D_s) is deflected by a mass concentration at redshift z_d (or distance D_d), whose depth is smaller than both D_d and D_{ds} (source–lens distance). The angle between the optic axis and the

true source position is $\vec{\beta}$ and the angle between the optic axis and the image is $\vec{\theta}$. The lens equation relates the true position of the source to its observed position on the sky through the deflection angle $\vec{\alpha}$. Let $\vec{\eta}$ denote the two dimensional position of the source on the source plane perpendicular to the optical axis. Fig. 4.1 shows that

$$\vec{\theta} D_s \simeq \vec{\beta} D_s + \vec{\alpha} D_{ds} \ ,$$

because of the smallness of the angles involved. This equation also reads

$$\vec{\beta} = \vec{\theta} - \widehat{\vec{\alpha}}(\vec{\beta}) \ . \tag{4.7}$$

where

$$\widehat{\vec{\alpha}} = \frac{D_{ds}}{D_s} \vec{\alpha} \tag{4.8}$$

is dubbed *scaled deflection angle*. Eq. (4.7) establishes that a source with true position $\vec{\beta}$ is seen in the angular position $\vec{\theta}$ satisfying (4.7).

When eq. (4.7) has more than one solution for fixed $\vec{\beta}$, a source in $\vec{\beta}$ has multiple images on the sky. This case is known as *strong gravitational lensing*.

In principle, eq. (4.7) allows to calculate $\vec{\beta}$ for any mass distribution $\Sigma(\vec{\xi})$. However, the main problem is the inversion of (4.7), since the mapping $\vec{\theta} \to \vec{\beta}$ is non-linear. Analytical result can be then obtained only for very simple mass distributions in the lens. Nevertheless, there are methods to determine the image multiplicity as a function of the source position.

Note that we derived eq. (4.7) by using Euclidean geometry, for which it is

$$separation = angle \times distance$$

It is not obvious that this is true in curved space-time. In an expanding universe, it holds, provided that its space section can be considered flat and we take *comoving* distances.

Eq. (4.4) reads then also

$$\widehat{\vec{\alpha}}(\vec{\theta}) = \frac{1}{\pi} \int_{\mathbb{R}^2} \mathrm{d}^2\theta' \ \kappa(\vec{\theta'}) \ \frac{\vec{\theta} - \vec{\theta'}}{|\theta - \theta'|^2} \ . \tag{4.9}$$

Here

$$\kappa(\theta) := \frac{\Sigma(D_d \theta)}{\Sigma_{cr}} \quad \text{with} \quad \Sigma_{cr} = \frac{c^2}{4\pi G} \frac{D_s}{D_d \ D_{ds}} \ , \tag{4.10}$$

is dubbed *dimensionless surface mass density* or *convergence*, while the *critical surface mass density* Σ_{cr} depends on the distances to the source and to the lens.

A mass distribution yielding $\kappa \geq 1$ somewhere, *i.e.* $\Sigma \geq \Sigma_{cr}$, produces multiple images if there are sources in suitable positions. Σ_{cr} therefore sets the separation between 'weak' and 'strong' lensing regimes.

A useful expression of the (scaled) deflection angle is obtained by defining the *deflection potential*,

$$\psi(\vec{\theta}) = \frac{1}{\pi} \int_{\mathbb{R}^2} \mathrm{d}^2\theta' \, \kappa(\vec{\theta'}) \ln(|\vec{\theta} - \vec{\theta'}|) \, , \tag{4.11}$$

so that the mapping $\vec{\theta} \to \vec{\beta}$ reads as a gradient

$$\widehat{\vec{\alpha}} = \nabla\psi \, , \tag{4.12}$$

and, from the identity $\nabla^2 \ln|\vec{\theta}| = 2\pi\delta_D(\vec{\theta})$ (δ_D is the two-dimensional Dirac delta distribution) and eq. (4.11) one obtains

$$\nabla^2\psi = 2\kappa \, , \tag{4.13}$$

i.e., a Poisson equation in two dimensions.

4.1.3 Magnification and distorsion

When an extended object is lensed, its observed shape will not coincide with the shape of the source, because light bundles are deflected differentially. In general, the shapes of the images must be determined by solving the lens equation for all points within an extended source.

Nevertheless, while geometry is modified, the Liouville's theorem and the absence of emission and absorption of photons in gravitational light deflection imply that lensing conserves surface brightness.

If a source is much smaller than the angular scale on which the lens properties change, the lens mapping can be locally linearized. The distortion of images is then described by the Jacobian matrix

$$\mathcal{A}(\theta) \equiv \frac{\partial\beta}{\partial\theta} = \left(\delta_{ij} - \frac{\partial^2\psi(\theta)}{\partial\theta_i \partial\theta_j} \right) = \begin{pmatrix} 1 - \kappa - \gamma_1 & -\gamma_2 \\ -\gamma_2 & 1 - \kappa + \gamma_1 \end{pmatrix} \, , \tag{4.14}$$

where we have introduced the components of the *shear* $\gamma \equiv \gamma_1 + i\gamma_2 = |\gamma| \mathrm{e}^{2i\varphi}$,

$$\gamma_1 = \frac{1}{2} \left(\psi_{,11} - \psi_{,22} \right) \, , \quad \gamma_2 = \psi_{,12} \, , \tag{4.15}$$

and κ is related to ψ through Poisson's equation (4.13)

$$\kappa = \frac{1}{2} \left(\psi_{,11} + \psi_{,22} \right) = \frac{1}{2} \operatorname{tr} \psi_{ij} \, . \tag{4.16}$$

The meaning of the terms convergence and shear now becomes intuitively clear. Convergence acting alone causes an isotropic focusing of light rays, leading to an isotropic magnification of a source. The source is mapped onto an image with the same shape but larger size. Shear introduces anisotropy (or astigmatism) into the lens mapping; the quantity $\gamma = (\gamma_1^2 + \gamma_2^2)^{1/2}$ describes

the magnitude of the shear and φ describes its orientation. In the presence of both κ and γ, the image of a circular source becomes an ellipse. The ratios of the semi-axes of such an ellipse to the radius of the source are given by the inverse of the eighenvalues of $\mathcal{A}(\theta_0)$, which are $1-\kappa\pm|\gamma|$, and the ratio of the solid angles subtended by an image and the unlensed source is the inverse of the determinant of $\mathcal{A}$. The inverse of the Jacobian is called the magnification tensor, $M(\theta)=\mathcal{A}^{-1}$, and, for a small source, the magnification is

$$\mu = \det M = \frac{1}{\det \mathcal{A}} = \frac{1}{(1-\kappa)^2 - |\gamma|^2} \,. \tag{4.17}$$

Note that the magnification is in general a function of position θ. The sign of μ is called the *parity* of an image: negative-parity images are mirror-symmetric images of the source. To consider the distortion of the shape of the images in somewhat more detail, one can write the Jacobi matrix as

$$\mathcal{A}(\theta) = (1-\kappa)\begin{pmatrix} 1-g_1 & -g_2 \\ -g_2 & 1-g_1 \end{pmatrix} \,, \quad \text{where } g(\theta) \equiv \frac{\gamma(\theta)}{1-\kappa(\theta)} \tag{4.18}$$

is the so called *reduced shear*, which is the central quantity in weak gravitational lensing.

4.1.4 Gravitational lensing phenomenology

As we have just described, light rays emitted by a distant source are deflected by the presence of a massive body along the line of sight toward the observer. Depending on the relative position of the source and the lens on the celestial sphere, it is possible to distinguish two different lensing regimes which give rise to different phenomenologies.

The *strong lensing* regime is produced when the lens is a highly non-linear massive object (*e.g.*, a large cluster of galaxies) and the source is close enough to it on the celestial sphere. In this case, light rays are strongly deflected and can reach the observer along different paths, leading then to multiple images of the source or causing the formation of arcs and/or rings. The observed distortion of background sources provides then information on the properties of the lens (*e.g.*, its mass).

If the source exhibits then an appreciable time variation, the multiple images will vary with time as well. As light does not cover the same source–observer distance for each image, source variations can occur at different times in different images. From the observed time delays, the distance scale at a given redshift can be measured, so allowing an estimate of the Hubble parameter H_o. A crucial point for this estimate is constructing a reliable mass distribution within the lens (see [84, 85] for details).

A particular case of strong lensing, is the so–called *microlensing*. It can occurs even with small lensing masses for sufficiently distant lenses and sources. It is a rare event, taking place when the separation among multiple images is

below the limiting resolution. In a typical microlensing event we observe then a light curve exhibiting rapid rise and fall, while the source crosses the position of the lens in the sky. The characteristic variation time scale, for lenses in our own Galaxy, is of the order of a month. Microlensing, in priciple, can then be used to trace galactic populations of faint or dark objects as white, red or brown dwarfs, extrasolar planets, neutron stars, black holes, etc. Various research programs actually led to the observation of previously undetected halo objects, currently dubbed MACHO's (Massive Compact Halo Objects) from the name of one of the above expriments (ref....).

Let us now consider the case of *weak lensing*; in this case, the distorsion of images is not to be associated with a particular intervening lens. Distorsions are typically small ($\sim 1\%$: the Jacobi matrix $\mathcal{A}$ is close to a unit matrix) and arise from all density fluctuations along the lines of sight. Hence, weak lensing does not yield the features of a single lensing object but allows to investigate the statistical properties for the density field as well as the geometry of the Universe.

To this aim, one computes the mean shear over a rather large region on the sky (a few arcmin^2 or more) by seaking systematic trends in the observed ellipticities of many ($\sim$ hundreds) galaxies. Indeed, since galaxies are not intrinsically spherical, one needs to average over many galaxies and cross-correlate their observed ellipticity so to extract a signal. By collecting many such observations one obtains a large survey (from a few to many thousands of square degrees) which may have an intricate geometry. Statistical measures applied to it allow then to derive constraints on cosmological parameters and on the statistical properties for the density field, over scales between a few arcmin to one degree.

Let us finally underline an important difference between strong and weak lensing. Strong lensing only occurs in the central part of clusters and therefore probes their inner mass structure. On the contrary, weak lensing probes the mass distribution at much larger angular separations even from cluster centres. Therefore, weak lensing can provide a parameter–free reconstruction of the projected two–dimensional mass distribution in clusters, directly mapping dark and visible matter distributions thereinside [86, 87].

Many researchers have devoted their work to these topics (see, *e.g.*, [88, 89, 90, 91, 92, 93, 87]). More details, obtained from the above papers, are discussed in the next sections.

4.2 Weak lensing by large scale structure

When propagating from the source to the observer, light rays are deflected and images are typically distorted not by localized mass concentrations, like galaxies or clusters, but rather by the whole gravitational field arising from the large scale structure (LSS) of the matter density field. This complex lensing effect requires that we extend previous results to any cosmology and 3–dimensional

matter distributions.

4.2.1 Light propagation in an inhomogenous Universe

According to GR, light propagates along the null–geodesics of the space–time. As shown in [83], the propagation of thin light bundles through an arbitrary space-time is described by the equation of geodesic deviation,

$$\frac{\mathrm{d}^2\vec{\xi}}{\mathrm{d}\,\lambda^2} = \mathcal{T}\vec{\xi}. \tag{4.19}$$

Here $\vec{\xi}$ is the separation vector of two neighboring light rays, λ the affine parameter along a suitably selected "central" ray of the bundle (fiducial ray), and $\mathcal{T}$ is the optical tidal matrix, which describes the influence of space–time curvature on the propagation of light. $\mathcal{T}$ can be expressed directly in terms of the Riemann curvature tensor.

The metric of the Universe, in the conformal Newtonian gauge, then reads

$$\mathrm{d}s^2 = a(\tau)^2\left[(1+2\Phi)\,c^2\mathrm{d}\tau^2 - (1-2\Phi)\,(\mathrm{d}w^2 + f_K^2(w)\,\mathrm{d}\Omega^2\,)\right]\,, \tag{4.20}$$

where τ is the conformal time, w is the comoving radial distance, $a = (1+z)^{-1}$ the scale factor, $f_K(w)$ is the comoving angular diameter distance, coinciding with w in a spatially flat model, and $\Phi(\mathbf{x}, w)$ is the Newtonian peculiar potential; it depends on the comoving position vector $\mathbf{x}$ and on τ, directly related to w, on the light cone.

Let now $\nabla_\perp = (\partial/\partial x_1,\, \partial/\partial x_2)$ be a transverse comoving gradient operator, and $\Phi^{(0)}(w)$ the potential along the fiducial ray. The comoving separation vector $\mathbf{x}$, between a ray separated by an angle $\vec{\theta}$ from a fiducial ray at the observer's position, will then evolve according to the equation

$$\frac{\mathrm{d}^2\mathbf{x}}{\mathrm{d}\,w^2} + K\mathbf{x} = -2\left[\nabla_\perp\Phi(\mathbf{x}(\boldsymbol{\theta}, w), w) - \nabla_\perp\Phi^{(0)}(w)\right]\,. \tag{4.21}$$

Formally, this transport equation can be solved by the method of Green's function, yielding

$$\mathbf{x}(\boldsymbol{\theta}, w) = f_K(w)\boldsymbol{\theta} - 2\int_0^w \mathrm{d}w'\, f_K(w-w')\left[\nabla_\perp\Phi(\mathbf{x}(\boldsymbol{\theta}, w'), w') - \nabla_\perp\Phi^{(0)}(w')\right]\,. \tag{4.22}$$

By definition, a source at distance w with separation $\mathbf{x}$ from the fiducial light ray, in the absence of lensing, would be seen at angular separation $\vec{\beta} = \mathbf{x}/f_K(w)$ from the fiducial ray. Therefore, the situation is analogous to standard lens theory. We can locally linearize the lens mapping, defining the Jacobian matrix

$$\mathcal{A}(\boldsymbol{\theta}, w) = \frac{\partial\beta}{\partial\boldsymbol{\theta}} = \frac{1}{f_K(w)}\frac{\partial\mathbf{x}}{\partial\boldsymbol{\theta}}\,, \tag{4.23}$$

and obtain from (4.22)

$$\mathcal{A}_{ij}(\boldsymbol{\theta}, w) = \delta_{ij} - 2\int_0^w \mathrm{d}w' \, \frac{f_K(w-w')f_K(w')}{f_K(w)} \Phi_{ik}(\mathbf{x}(\boldsymbol{\theta}, w'), w') \, \mathcal{A}_{kj} \,, \quad (4.24)$$

an exact relation in the limit of validity of the weak–field metric. The matrix Φ_{ik} is obtained by performing covariant derivatives of Φ in respect to x_i, x_k. Next, we expand $\mathcal{A}$ in powers of Φ and keep the linear term only:

$$\mathcal{A}_{ij}(\boldsymbol{\theta}, w) = \delta_{ij} - 2\int_0^w \mathrm{d}w' \, \frac{f_K(w-w')f_K(w')}{f_K(w)} \Phi_{ij}(f_K(w')\boldsymbol{\theta}, w') \,. \quad (4.25)$$

Hence, to linear order, the distortion is again obtained by integrating along the unperturbed ray $\mathbf{x} = f_K(w)\,\boldsymbol{\theta}$. Corrections to this Born approximation are $\mathcal{O}(\Phi^2)$. If we now define the deflection potential

$$\psi(\boldsymbol{\theta}, w) \equiv 2\int_0^w \mathrm{d}w' \, \frac{f_K(w-w')}{f_K(w)f_K(w')} \Phi(f_K(w')\boldsymbol{\theta}, w') \,. \quad (4.26)$$

then $\mathcal{A}_{ij} = \delta_{ij} - \psi_{ij}$ (ψ_{ij} is related to ψ as Φ_{ij} is related to Φ), just as in ordinary lens theory. In this approximation, lensing by the 3–D matter distribution can be treated as an equivalent lens plane with deflection potential ψ and convergence and shear

$$\kappa = \nabla^2\psi/2 \,, \quad \gamma = \gamma_1 + i\gamma_2 = (\psi_{,11} - \psi_{,22})/2 + i\psi_{,12} \,. \quad (4.27)$$

Note that the convergence κ and the shear γ_i, both obtainable from the scalar lensing potential ψ, are stricly related, so that $\kappa_{,1} = \gamma_{1,1} + \gamma_{2,2}$ [94].

This allows one to derive consistency relations satisfied by weak lensing distortions (e.g. [95]) and observational deviations from them yield estimates for observational noise or systematics.

4.2.2 Convergence and shear power spectrum

In a very simple way it is possible to relate κ and γ to the mass density contrast δ of matter fluctuations in the Universe. Let us consider the case of the convergence. From eqs (4.26), (4.27) and from the 3–D Poisson equation in comoving coordinates

$$\nabla^2\Phi = \frac{3H_0^2\Omega_m}{2a}\delta \,, \quad (4.28)$$

one can draw the full expression of the convergence:

$$\kappa(\boldsymbol{\theta}, w) = \frac{3H_0^2\Omega_m}{2}\int_0^w \mathrm{d}w' \, \frac{f_K(w')f_K(w-w')}{f_K(w)} \, \frac{\delta(f_K(w')\boldsymbol{\theta}, w')}{a(w')} \,, \quad (4.29)$$

where in the 3–D Laplacian of ψ, the component $\Phi_{,33}$ vanishes in the line-of-sight integration.

The result (4.29) concerns the presence of a single source located at distance w or redshift z_s. For a redshift distribution of sources $n_w(w)\,dw = n_z(z)\,dz$, the effective surface mass density becomes

$$\begin{aligned}\kappa(\boldsymbol{\theta}) &= \int \mathrm{d}w\, n_w(w)\,\kappa(\boldsymbol{\theta}, w) \\ &= \frac{3H_0^2\Omega_m}{2}\int_0^{w_h} \mathrm{d}w\, g(w)\, f_K(w)\,\frac{\delta(f_K(w')\boldsymbol{\theta}, w')}{a(w')}\,, \end{aligned} \tag{4.30}$$

with

$$g(w) = \int_w^{w_h} \mathrm{d}w'\, n_w(w')\,\frac{f_K(w-w')}{f_K(w')}\,, \tag{4.31}$$

which is the source–redshift weighted lens efficiency factor D_{ds}/D_s for a density fluctuation at distance w, and w_h is the comoving horizon distance, obtained from $w(a)$ by letting $a \to 0$.

For statistical analysis of cosmic shear, it is most common to use 2–point quantities, *i.e.* those which are quadratic in the shear. Higher order statistics will not be discussed in this thesis.

In particular, we define the power spectra $P_\delta(k)$ of the 3–D matter density contrast and $P_\kappa(\ell)$ of the 2–D convergence as

$$\langle \delta(\mathbf{k}_1)\delta(\mathbf{k}_2)\rangle = (2\pi)^3\delta_D(\mathbf{k}_1+\mathbf{k}_2)P_\delta(k_1) \tag{4.32}$$

and

$$\langle \kappa(\ell_1)\kappa(\ell_2)\rangle = (2\pi)^2\delta_D(\ell_1+\ell_2)P_\kappa(\ell_1)\,. \tag{4.33}$$

Here, δ_D represents the Dirac function. It expresses statistical homogeneity, whereas statistical isotropy implies that $P_\delta(\mathbf{k})$ and $P_\kappa(\ell)$ only depend on $k = |\mathbf{k}|$ and $\ell = |\ell|$.

It is often useful to work in Fourier space. Thus, the 3–D matter density contrast $\delta(\mathbf{x})$ and the convergence $\kappa(\boldsymbol{\theta})$ can be written as

$$\delta(\mathbf{x}) = \int \frac{\mathrm{d}\mathbf{k}}{(2\pi)^3}\, e^{-i\mathbf{k}\cdot\mathbf{x}}\,\delta(\mathbf{k}) \quad \text{and} \quad \kappa(\boldsymbol{\theta}) = \int \frac{\mathrm{d}\ell}{(2\pi)^2}\, e^{-i\ell\cdot\boldsymbol{\theta}}\,\kappa(\ell). \tag{4.34}$$

Finally, it is worth noting that in Eq.(4.33) we used a flat-sky approximation which is sufficient for most weak-lensing purposes. For full-sky studies, the expansion over spherical harmonics (instead of plane waves as in Eq.(4.34)) will be necessary.

In order to relate the convergence power spectrum to the power spectrum $P_\delta(k)$ of the 3–D matter distribution in the Universe, it is necessary to introduce the Limber's equation (1953). If δ is an homogeneous and isotropic 3–D random field, then the projections

$$g_i(\boldsymbol{\theta}) = \int \mathrm{d}w\, q_i(w)\,\delta(f_K(w)\boldsymbol{\theta}, w) \tag{4.35}$$

also are (2–D) homogeneous and isotropic random fields, where the q_i are weight functions. In particular, the correlation function depends only on the modulus of the separation vector. Therefore, its Fourier transform, the 2–D power spectrum at angular scale $1/\ell$ is obtained from the 3–D power at length scale $f_K(w)(1/\ell)$, integrated over w.

Hence, comparing (4.30) and (4.35), one can argue that $\kappa(\boldsymbol{\theta})$ is a projection of δ with the weights $q(w) = (3/2)\, H_0^2\, \Omega_m\, g(w)\, f_K(w)/a(w)$, so that

$$P_\kappa(\ell) = \frac{9H_0^4\Omega_m^2}{4} \int_0^{w_h} \mathrm{d}w\, \frac{g(w)^2}{a^2(w)}\, P_\delta\left(\frac{\ell}{f_k(w)}, w\right) . \tag{4.36}$$

The power spectrum P_κ, if observable, can therefore be used to constrain the 3–D power spectrum P_δ. The shear power spectrum P_γ is identical to the expression (4.36). The reason is that, in Fourier space, the quantities $\langle\kappa^2\rangle$ and $\langle\gamma^2\rangle$ are identical. This can be derived easily from Eq.(4.25) and Eq.(4.27), with the derivatives replaced by powers in ℓ's in Fourier space.

The powerspectrum $P_\kappa(\ell)$ is plotted in Fig. 4.2 for a number of cosmological models. Predictions of P_κ are plotted both assuming linear growth of the density structure, and the prescription of the fully nonlinear power spectrum as given by the fitting formulae of Smith *et al.* [96].

From this figure one infers that the nonlinear evolution of the density fluctuations becomes dominant for values of $\ell \gtrsim 200$, corresponding to an angular scale of about $30'$ ($\theta \sim 100\,\mathrm{deg}\,/\ell$), the precise values depending on the cosmological model and the redshift distribution of the sources. Furthermore, the dimensionless power spectrum $\ell(\ell+1)P_\kappa(\ell)$ peaks at around $\ell \sim 10^4$, corresponding to an angular scale of $\sim 1'$, again somewhat depending on the source redshift distribution. Finally, one notices that the shape and amplitude of P_κ depends on the values of the cosmological parameters; therefore, by measuring the power spectrum, or quantities directly related to it, one can constrain the values of the cosmological parameters.

Measuring cosmic shear is certainly a particularly challenging goal. In fact since the weak lensing effects are very small, expecially on larger scales, the observational and instrumental effects are expected to be larger than the cosmic shear signal, and thus have to be understood and removed with great precision.

For this reasons, it took until the year 2000 before these effects were first detected by four groups independently [97, 98, 99, 100]. Later, in [101] they reported a significant cosmic shear measurement which also agreed with the earlier results. The fact that the results from four independent teams agreed within the respective error bars immediately lend credit to this new window of observational cosmology.

Relatively soon after the announcement of the first cosmic shear detections, additional results were published. These newer surveys can roughly be classified as follows: deep surveys (like the VIRMOS-DESCART survey [102, 103] or the Suprime-Cam survey [104]), shallower, but much wider surveys (RCS

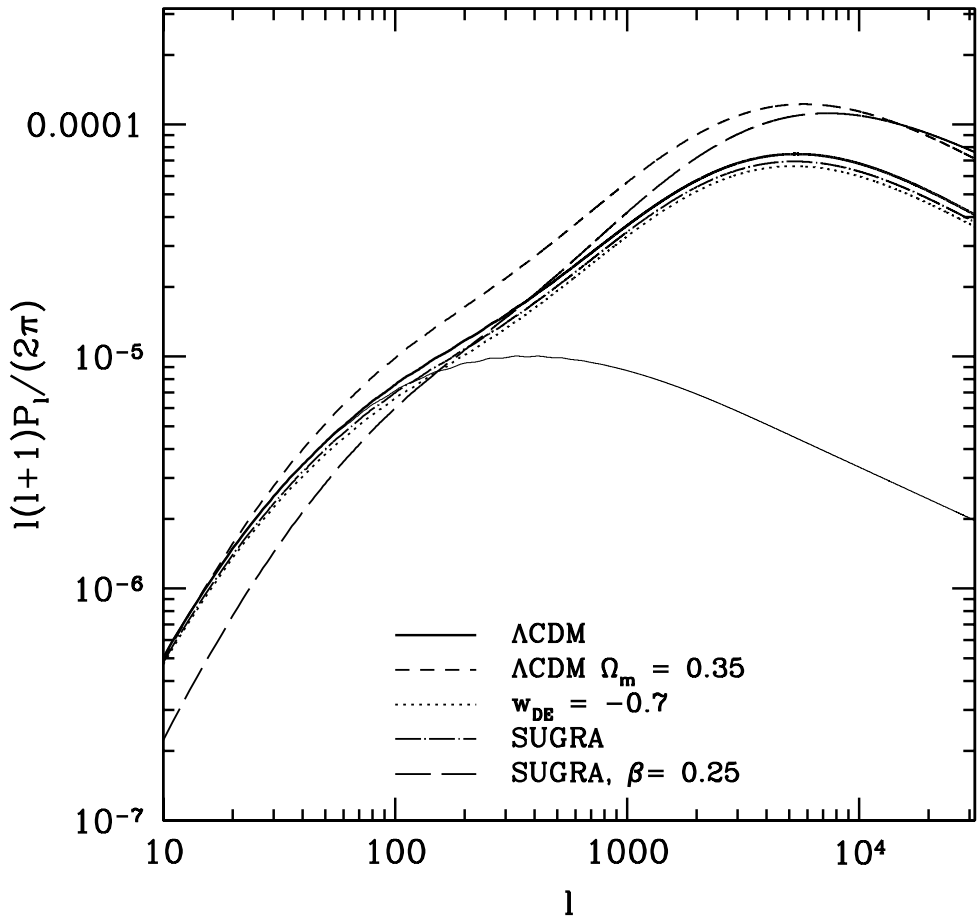

Figure 4.2: Weak lensing power spectra for different cosmological models. Here, the spectrum of the ΛCDM model is plotted varing some of its parameters, in order to point out the sensibility to different parameters. Also the spectra for a SUGRA and a coupled SUGRA model are plotted. It is worth noting the quite good agreement between the spectra of a constant w_{DE} and a SUGRA model.

survey [105, 106]), and special surveys, such as those obtained with the Hubble Space Telescope.

4.3 3–D Weak Lensing

In the analysis of weak gravitational surveys as described in the previous sections, the signal is generated by correlations of shapes of galaxies projected onto the sky. In order to estimate correctly this correlation, one needs to know the statistical distribution of the source galaxies.

Therefore, most lensing surveys use multi-colour photometry of the sources to estimate their redshifts. Even if "photometric redshifts" are not as accurate as "spectroscopic redshifts", the former are most extensively used because of

the depth and the large number of sources a typical survey can provide. On the other hand, if one has an estimate of the distance information of *individual* sources, rather than just the *distribution* of distances, then it is possible to use this information and investigate lensing in three dimensions.

There are several ways 3–D informations can be used: one is to reconstruct the 3–D gravitational potential or the overdensity field from 3–D lensing data [107, 108, 109]. The second is to exploit the additional statistical power of 3–D information, firstly by dividing the sources into a number of shells based on estimated redshifts. One then essentially performs a standard lensing analysis on each shell, but exploits the extra information from cross–correlations between shells. This sort of analysis is commonly referred to as *tomography* [110, 111, 112, 113, 114, 115, 116]. Finally, one can perform a fully-3D analysis of the estimated shear field [117, 118, 119]. Each approach has its merits, but in this thesis we will discuss in particular about the case of tomography.

4.3.1 Weak lensing tomography

A natural course of action in the tomographic technique is to divide the survey into slices at different distances, and perform a study of the shear pattern on each slice. In order to effectively use the informations, it is necessary to look at cross-correlations of the shear fields in the slices, as well as correlations within each slice [110].

The power spectrum for the weak lensing convergence between the ith– and jth– redshift bin can be obtained generalizing the expression (4.36):

$$P_\kappa^{(ij)}(\ell) = \frac{9H_0^4\Omega_m^2}{4}\int_0^{w_h} \mathrm{d}w\, \frac{g^{(i)}(w)\, g^{(j)}(w)}{a^2(w)}\, P_\delta\left(\frac{\ell}{f_k(w)}, w\right). \tag{4.37}$$

In this case, the source–redshift weighted lens efficiency factor (4.31) becomes

$$g^{(i)}(w) = \int_w^{w_h} \mathrm{d}w'\, n_w^{(i)}(w')\, \frac{f_K(w-w')}{f_K(w')}, \tag{4.38}$$

where the function $n_w^{(i)}(z)$ is the redshift distribution of the source galaxies falling in the i-th photometric redshift bin, per unit solid angle.

Ref.[110] illustrates the power and limitation of tomography, with two shells (Fig. 4.3). As expected, the deeper shell (2) has a larger lensing power spectrum than the nearby shell (1), as the more distant are galaxies, the greater quantity of material their light rays have to cross. Moreover, it is no surprise to find that the power spectra from shells are correlated, since the light from both passes through some common material.

One can occount for errors in distance estimates with photometric redshifts with a suitable modification to $n_w^{(i)}(z)$ [120]:

$$n_w^{(i)}(z) \;=\; \int_{z_{ph}^{(i)}}^{z_{ph}^{(i+1)}} \mathrm{d}z_{ph}\, n_z(z)\, p(z_{ph}|z). \tag{4.39}$$

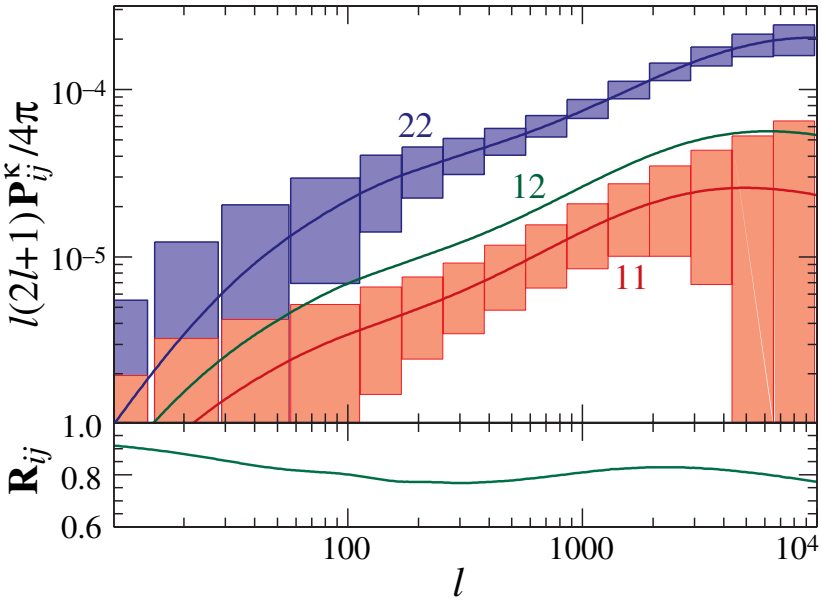

Figure 4.3: The power spectra and cross-correlation of two slices and their correlation coefficient. The galaxy population is split into two bins across a median redshift $z_{\rm median} = 1$. From Hu (1999).

It is a very crucial point. In fact, as previously said, due to the large number of observed galaxies with future surveys, one needs to refer to their photometric redshifts, even if the determination of these redshifts may be not so accurate as the spectroscopic ones. In the model given by equation (4.39), the mapping between the photometric z_{ph} and the spectroscopic redshift z is obtained convolving the overall galaxy distribution per unit solid angle, $n_z(z)$, with a probability distribution $p(z_{ph}|z)$ in z_{ph} at a given z. We choose a Gaussian function at each redshift for the distribution of photometric redshifts, *i.e.*

$$p(z_{ph}|z) = \frac{1}{\sqrt{2\pi}\sigma_z} \exp\left[-\frac{(z - z_{ph})^2}{2\sigma_z^2}\right] \tag{4.40}$$

while the overall distribution of source galaxies is chosen in the parametrized form:

$$n_z(z) = \frac{d^2N}{dz\, d\Omega} = \frac{B}{z_0\, \Gamma\left(\frac{A+1}{B}\right)} \left(\frac{z}{z_0}\right)^A \exp\left[-(z/z_0)^B\right], \tag{4.41}$$

where A, B and z_0 are the parameters. One can easily check that equation (4.39) turns into:

$$n_z^{(i)}(z) = \frac{1}{2} n(z) \left[\mathrm{erf}(x^{(i+1)}) - \mathrm{erf}(x^{(i)})\right], \tag{4.42}$$

with $x^{(i)} \equiv (z_{ph}^{(i)} - z)/\sqrt{2}\sigma_z$ and $\mathrm{erf}(x)$ the error function.

The cosmic shear power spectrum will receive an additional shot-noise contribution from the random intrinsic ellipticities of source galaxies and measurement error [121]. Thus, the observed power spectrum between redshift bins i and j can be expressed as:

$$P_{\rm obs}^{(ij)}(\ell) = P_{\kappa}^{(ij)}(\ell) + \delta_{ij}\frac{\sigma_\epsilon^2}{\bar{n}_i} \tag{4.43}$$

where σ_ϵ is the rms shear due to intrinsic ellipticity and measurement noise (we assume $\sigma_\epsilon \simeq 0.22$ [166]) and

$$\bar{n}_i = \left[\frac{n_g}{amin^{-2}}\right]\left(\frac{1}{60}\frac{\pi}{180}\right)^{-2}\hat{n}_i \tag{4.44}$$

is the average number density of galaxies per steradians in the i-th redshift bin, n_g being the number of galaxies per square arcminute and $\hat{n}_i$ the fraction of sources belonging to the bin.

Chapter 5

CMB properties

In this chapter I shall outline the principal statistical and physical properties of the CMB field.

5.1 Description of the radiation field

The properties of an electromagnetic wave, propagating in a direction $\vec{k}$, orthogonal to the celestial sphere, can be conveniently described by a rank 2 symmetric tensor, $I_{ab}(\vec{k})$. Labeling E_i the components of the electric field vector with respect to an orthonormal basis $(\vec{e}_1, \vec{e}_2)$ in a plane perpendicular to $\vec{k}$, such tensor reads:

$$I_{ab}(\vec{k}) = \frac{\langle E_a E_b \rangle}{4\pi c}. \tag{5.1}$$

Brackets yield time averaging. The total intensity of the radiation along the direction $\vec{k}$ is then the tensor trace

$$I(\vec{k}) = I_{11}(\vec{k}) + I_{22}(\vec{k}). \tag{5.2}$$

Averaging over the celestial sphere, we obtain the *average* radiation intensity $\bar{I}$. Assuming a thermal radiation spectrum, it is $\bar{I} = \sigma T^4$ (in units $c = \hbar = 1$, $\sigma = \pi^2/15$). However, much cosmological information enclosed in the CMB radiation is conveyed by temperature and polarization *fluctuations*. It is then convenient to replace I_{ab} with the dimensionless tensor $\Delta_{ab} = I_{ab}/\bar{I} - \delta_{ab}/2$. Its components are directly related to the temperature anisotropies and the Stokes parameters as follows:

$$\hat{T} = (\Delta_{11} + \Delta_{22})/4 \ , \ Q = \Delta_{11} - \Delta_{22} \ , \ U = \Delta_{12}/2. \tag{5.3}$$

The Stokes parameter V, accounting for circular polarization, is assumed to vanish: Thomson scattering of photons, during recombination and reionization, does not induce circular polarization.

Temperature anisotropies $\hat{T}$ are a scalar field; Q and U, instead, depend on the choice of the basis $(\vec{e}_1, \vec{e}_2)$. If the basis is rotated by an angle ψ, so that

$$\vec{e_1'} = \cos\psi\ \vec{e}_1 + \sin\psi\ \vec{e}_2, \qquad \vec{e_2'} = -\sin\psi\ \vec{e}_1 + \cos\psi\ \vec{e}_2\ , \tag{5.4}$$

the Stokes parameters transform into

$$Q' = \cos 2\psi\ Q + \sin 2\psi\ U, \qquad U' = -\sin 2\psi\ Q + \cos 2\psi\ U. \tag{5.5}$$

Accordingly, $Q \pm iU$ are spin–2 fields.

5.2 The CMB angular power spectra

The observed values of $\hat{T}$, Q and U are functions of the sky direction $\vec{n}$ $(= -\vec{k})$. Accordingly, we can expand $\hat{T}$ using ordinary scalar spherical harmonics $Y_{lm}(\vec{n})$, which form an orthonormal basis for differentiable functions on the sphere. The temperature anisotropy in the direction $\vec{n}$ then reads:

$$\hat{T}(\vec{n}) = \sum_{l=2}^{\infty} \sum_{m=-l}^{m=+l} a_{T,lm} Y_{lm}(\vec{n})\ . \tag{5.6}$$

The coefficients with index l are related to features on angular scales $\alpha \sim \pi/l$, while m refers to the azimuthal orientation of such features. At each l, there are $2l+1$ independent orientations m. The expansion (5.6) includes contributions by the quadrupole and higher moments: the monopole vanishes by construction and the dipole component, dominated by the Doppler shift due to observer's motion with respect the CMB frame, is subtracted.

An analogous expansion for polarization must take into account the behaviour of Q and U under rotations of the vectors $(\vec{e}_1, \vec{e}_2)$ [122, 123, 124]. The spin ± 2 linear combinations $Q \pm iU$, under rotations by ψ, change by a phase:

$$(Q \pm iU)' = e^{\pm 2i\psi}\,(Q \pm iU) \tag{5.7}$$

An orthonormal basis on the sphere for functions of definite spin s, is provided by the *spin-weighted spherical harmonics* ${}_sY_{lm}$, which can be obtained by applying suitable operators, called spin raising or lowering operators, to ordinary spherical harmonics. The resulting expansions read:

$$\begin{array}{rcl} (Q+iU)(\vec{n}) & = & \sum_{lm} a_{+2,lm}\ {}_{+2}Y_{lm}(\vec{n}) \\ (Q-iU)(\vec{n}) & = & \sum_{lm} a_{-2,lm}\ {}_{-2}Y_{lm}(\vec{n}). \end{array} \tag{5.8}$$

We can then introduce two new scalar quantities E and B, defined through the rotationally invariant coefficients

$$\begin{array}{rcl} a_{E,lm} & = & -\left(a_{2,lm} + a_{-2,lm}\right)/2 \\ a_{B,lm} & = & -\left(a_{-2,lm} + a_{2,lm}\right)/2i, \end{array} \tag{5.9}$$

reading

$$E(\vec{n}) = \sum_{l=2}^{\infty} \sum_{m=-l}^{m=+l} a_{E,lm} Y_{lm}(\vec{n}) \ , \qquad B(\vec{n}) = \sum_{l=2}^{\infty} \sum_{m=-l}^{m=+l} a_{B,lm} Y_{lm}(\vec{n}) \ . \tag{5.10}$$

Being defined in harmonic space, the E and B fields are nonlocal and, in principle, in order to know them in one direction, measurements are required over the whole celestial sphere. If data cover it partially, the decomposition of CMB polarization into E and B is not unique (see, e.g., [125, 126, 127]). In this case a third, *ambiguous* mode must be added, in order to avoid leakages between E and B modes.

Besides the advantage of being scalar quantities, E and B allow to relate CMB polarization to its physical origin, thanks to their different behaviour under parity: E is even, B is odd (in analogy with electric and magnetic fields, wherefrom their denomination arose). As we outline in Sec. 5.5, this different behaviour has several important consequences.

The set of expansions coefficients $\{a_{T,lm}, a_{E,lm}, a_{B,lm}\}$ completely describes the CMB field. If the field is Gaussian, their phases are random and the mean of each multipole vanishes, $\langle a_{T,lm} \rangle = \langle a_{E,lm} \rangle = \langle a_{B,lm} \rangle = 0$. All physical information is then enclosed in four angular power spectra (APS):

$$\begin{array}{rcl} \langle a^*_{T,lm} a_{T,l'm'} \rangle & = & C_{Tl} \ \delta_{l,l'} \, \delta_{m,m'} \\ \langle a^*_{E,lm} a_{E,lm'} \rangle & = & C_{El} \ \delta_{l,l'} \, \delta_{m,m'} \\ \langle a^*_{B,lm} a_{B,lm'} \rangle & = & C_{Bl} \ \delta_{l,l'} \, \delta_{m,m'} \\ \langle a^*_{T,lm} a_{E,lm'} \rangle & = & C_{TE,l} \ \delta_{l,l'} \, \delta_{m,m'} . \end{array} \tag{5.11}$$

The power spectra for the cross-correlations between B and $\hat{T}$ or E vanish due to their different behaviour under parity transforms.

The brackets at the l.h.s of eq. (5.11) prescribe an averaging operation which, in principle, is an ensemble average. However, we are given only a single realization of the CMB sky. When applying the above definition to real data, eq. (5.11) translates into:

$$\tilde{C}_{Tl} = \frac{1}{2l+1} \sum_{m=-l}^{+l} |a_{T,lm}|^2 \tag{5.12}$$

with similar relations holding for the other APS. Under ideal conditions, these are the minimum variance estimators of CMB APS, with associated errors:

$$\Delta \tilde{C}_{Tl} = \sqrt{\frac{2}{2l+1}} \tilde{C}_{Tl}. \tag{5.13}$$

The expression (5.13) yields the precision with which a CMB multipole can be directly known to a single observer, due to Cosmic Variance (CV). CV is clearly higher for low multipoles, for which, by definition, just a few realizations are observable; for instance, CV for the quadrupole is $\sim 65\%$.

Suggestions for easing CV limitations have been proposed by [128, 129, 130], by probing the quadrupole and higher multipoles seen by high–z clusters. These methods require sensitivity levels and foreground decontamination far from present capacities.

5.3 Comparison with real data and parameter extraction

For Gaussian fields, the APS and the two–point correlation functions completely define the statistical properties of the pure CMB anisotropies and polarization fields, in multipole and position space respectively. The comparison of predictions with real data, however, involves additional complications. The microwave signal is observed through a finite resolution antenna, and the resulting measurements are collected into sky maps with pixels of finite size. Moreover, the signal in each pixel of an actual sky map sums up the CMB contribution and different kinds of foreground and instrumental noises.

5.4 Time Evolution of Energy density fluctuations

In this section we briefly describe the physical processes responsible for the birth and evolution of CMB temperature and polarization anisotropies, outlining how several cosmological parameters affect the APS introduced in the previous sections. This section therefore describes a great success of theoretical analysis, which succeded in relating cosmological parameters to observational data with unprecedented precision and now forms the core of the so-called *precision cosmology*. This success is made possible by the reliability of linearized differential equations, thanks to the low fluctuation amplitude, and by the high efficiency reached by observational apparati.

Several authors have accurately studied the problem of setting initial conditions in cosmology and the expressions of the dynamical equations governing the evolution of perturbations. Here we shall mostly describe the key procedures and results of such analysis, and refer to the comprehensive work by Ma & Bertschinger [131] for analytical details.

It is convenient to start the analysis of fluctuation evolution at a time t_i earlier than matter–radiation equality, which occurs at a redshift $z_{eq} \simeq 2.6 \cdot 10^4 \Omega_m h^2$, and selected in order that all scales of interest are still outside the cosmological horizon.

To first order, perturbations in the metric tensor arise either from primordial density fluctuations or from gravity waves (GW) generated during Inflation. Density fluctuations involve all components of the cosmological fluid (radiation, baryons, dark matter and, possibly, dark energy) and produce only

scalar perturbations, as they are invariant under parity transform. Density perturbations are typically expressed in term of their power spectrum, $P(k)$ (i.e. the Fourier transform of the two–points correlation function for density fluctuations), assumed to follow a power law, $P(k) = Ak_s^n$, so to avoid privileged scales. Generic inflationary models predict a scalar spectral index $n_s \sim 1$; if $n_s = 1$ (Zel'dovich spectrum) fluctuations at horizon entry display the same average amplitude over all scales.

For $n_s < 1$, generic inflationary models predict a background of GW, with a power spectrum [132, 133]

$$P_t(k) = rA\,k^{n_T} \quad \text{with} \quad n_T = n_s - 1 \text{ and } \; r = 7(1 - n_s) \tag{5.14}$$

which have a tensor nature and are then responsible for pseudoscalar features in the CMB APS.

The sequel of events shaping the observed APS are then the following ones:
(1) – Entry into the horizon and passage from radiation dominated to matter dominated expansion.
(2) – Gradual passage from the tight–coupling regime to photon free streaming, during the primeval hydrogen recombination.
(3) – Reionization at low–z ($\sim$ 5–25) and cosmic opacity to CMB photons.
(4) – Deviations from matter dominated expansion, when Dark Energy (DE) becomes first sub–dominant and then eventually drives the expansion.

Until recombination, photons and the electron–baryons component form a tightly coupled fluid on all scales of cosmological relevance. In fact: (i) Electric charge accumulation would require high amounts of energy and thus never occurs: electron and baryons therefore move together as though they were bound in atoms. (ii) Photons could in principle follow a different distribution, however Thomson scattering yields a photon mean free path well below all scales of cosmological interest.

In the first stages of Universe evolution, then, the dynamical state of the baryon–electron–photon plasma is completely defined by its density (fluctuation) and velocity fields.

Outside horizon, no causal relation is possible and perturbation modes in the Newtonian gauge are frozen. Once a relevant scale enters the horizon, fluctuations start evolving and compression waves can form. The number of compressions and rarefaction phases experienced by a given perturbation is set by the time elapsing from the moment of horizon entering, and hence the mass scale of the fluctuation, and recombination. A mass scale of $\sim 10^{16} M_\odot$ enters the horizon around recombination and will be in a state of maximum compression, oscillations on scales $\lesssim 10^{12} M_\odot$, instead die out before recombination, as electron m.f.p. becomes greater than their wavelength.

Recombination occurs when the temperature is so low that the number of photons, with energy > 13.6 eV, is no longer enough to keep electrons and protons from binding into hydrogen atoms. The number of free charged particles drops rapidly in a redshift interval around $z_{rec} \sim 1100$ and the Universe

becomes transparent to electromagnetic radiation.

As the coupling fades, photons no longer constitute a fluid, and higher order multipoles gradually switch on in their distribution, as power is transferred from low l's to higher ones. Most of the features observed in present APS have then been imprinted at the Last Scattering Band, when $\sim$ 90–95% of CMB photons had their last interaction with matter.

As is known, DM interacts with photons and baryonic matter just through gravitation. Its effect, however, cannot be neglected even in the prediction of CMB APS. DM sets the location of the first anisotropy peak and is responsible of the different height further acoustic peaks. Its role in SW and ISW effects (see below) is then dominant.

5.4.1 Physical effects in the last scattering band

Evolution of CMB perturbations can be followed accurately only through numerical integration [1]. For the sake of example, in Fig. 5.1 we show the $C_{T,l}$ spectrum, for the Standard Cold Dark Matter (SCDM) model.

The SCDM spectra clearly shows an almost flat region at low multipoles, followed by alternated peaks and deeps, that are related to the presence of compression waves in the baryons–radiation plasma, until recombination. At $l > 1000$, the spectrum starts to fade. All these features can be reconduced to three main effects affecting the photon distribution at recombination:
(1) – *The Sachs & Wolfe effect* (SW) [136]. On scales larger than the horizon at recombination, density fluctuations trace the gravitational potential ψ, as they had not yet entered an oscillatory regime. At decoupling photons are no longer tied to the matter distribution; as they climb out from potential wells, photons suffer the effects of a gravitational redshift and time dilation. The net results are temperature fluctuations $\hat{T} \propto \psi$, whose variance is seen as $C_{T,l}$ over very large scales. Additional anisotropies can also arise along the photon's path, if the time derivative of the metric is non–vanishing. This effect, called *Integrated Sachs & Wolfe* (ISW), can be due to GW or time evolution of the gravity potential, and is therefore expected to play a key role in models with DE.
(2) – *Radiation concentration or rarefaction.* Fluctuations on scales entering the horizon before recombination begin oscillating as acoustic waves. Waves

[1] Solving the full set of Boltzmann equations, governing the photon distribution up to $z = 0$, is quite expensive in terms of computational resources. Boltzmann equations can be however integrated along the line of sight [134]. The resulting expressions for APS depend on a source term and a geometrical term. The former receives contributions just from 4 spherical harmonics, which need to be calculated exactly through Boltzmann equations; the latter does not depend on the model and can be evaluated once and then stored for subsequent evaluations. The critical difficulty to produce a fair numerical code is then a fair truncation of the multipole series, preventing the "signal" to bounce at the truncation point. The line–of–sight approach forms the core of most modern codes. Among them we mention here the CMBFAST code by Seljak & Zaldarriaga [134], and its derivative code, CAMB by Lewis & Challinor [135].

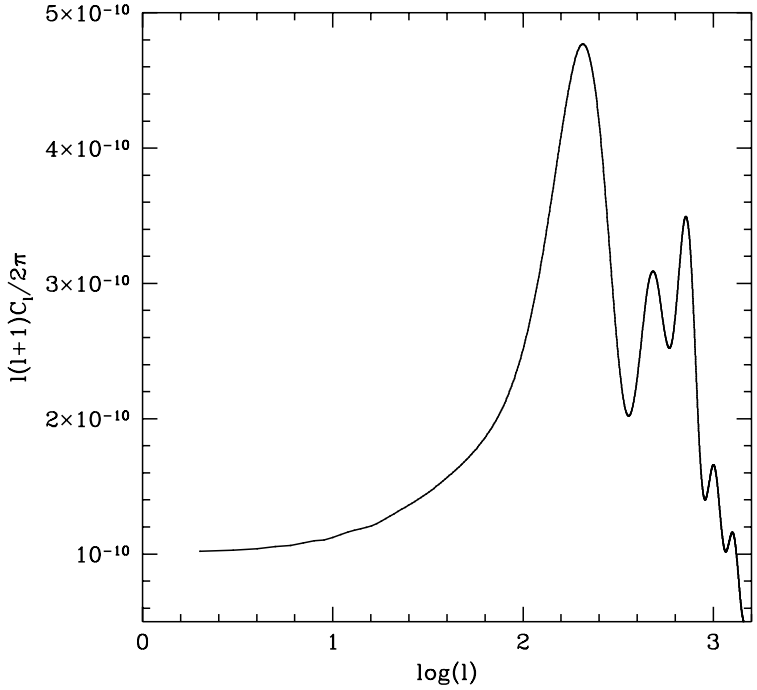

Figure 5.1: Anisotropy spectrum in a SCDM model.

reaching the LSS in an antinode state correspond to fluctuations δ undergoing a state of maximum compression or rarefaction and with vanishing velocity. The CMB temperature fluctuation for scales attaining recombination with a antinode is, therefore, $\hat{T} = Tr(\Delta_{ab}) = \delta/4$.

(3) – *Doppler shifts.* Compression waves attaining recombination in a node phase corresponds to fluctuations of vanishing amplitude but with maximum velocity, $|\vec{v}| = \delta$. While δ is a scalar quantity, $\vec{v}$ is a vector and its contribution to CMB spectra arise because of its component along the line of sight, which, in average is $v/\sqrt{3}$. Accordingly, the observed temperature fluctuation $\hat{T}$, on scales attaining recombination in this state, is lower than on scales attaining recombination with an antinode.

These effects are clearly visible in the features of the APS displayed in Fig. 5.1. The plateau extending up to $l \sim 100$ is a consequence of the Sachs & Wolfe effect, which predicts $l(l+1)C_l = const$ for $P(k) \propto k$. The $\hat{T}$ peak at $l \simeq 200$ denotes the largest scale undergoing compression exactly at recombination. This is clearly the scale which is just entering the horizon. The position of the first peak in l space, is then fixed by the angle under which the Hubble radius at recombination is seen by an observer at $z = 0$. The following peaks correspond to waves attaining recombination with an antinode phase. In absence of Doppler effects, power between subsequent peaks would vanish, in correspondence of waves reaching the LSS in a node state. Doppler effects are then mainly responsible for filling the gaps between peaks, and the habit of dubbing the first acoustic peak, *Doppler* peak is misleading.

The alternating heights of the peaks also has a simple qualitative explanation. As already stated, when a scale enters the horizon, baryonic matter and radiation begin oscillating. DM fluctuations, not being subjected to photon drag, are instead free to continue growing. The growing potential well due to DM sets the zero–point for the sonic oscillations in the photon-baryon plasma. Peaks corresponding to oscillations in phase with DM fluctuations (first and third in the Fig shown) will then be higher than peaks for oscillations in phase opposition with DM.

Finally, on scales smaller than the width of the LSS fluctuations they are smoothed out due to the high optical depth to Thomson scattering during recombination. For a LSS width of $\Delta z \simeq 40$, this results in drastic erase of features on angular scales smaller than of $\simeq 20$ arcmin and is shown by the APS' amplitude decrease after the third peak.

5.4.2 Constraints from primary T–anisotropy data

The qualitative discussion in the previous section outlined the main physical processes responsible for the *primary anisotropies* observed in the microwave sky. In turn, these processes depend on several cosmological parameters and variation of such parameters affects the CMB spectra in a precise (and predictable) way. In this section we show how some of this parameters alter features in APS for models more realistic than the simple SCDM. Most of these effects were first ordered by Hu and Sugiyama [137].

For purely adiabatic perturbations, power-law initial conditions are determined completely by four parameters A, n_s, r, and n_T. The first two parameters enter into the definition of the primeval fluctuation spectrum $P(k)$, the latter two in the definition of the spectrum of GW's. Within the context of single–field Inflation, the consistency relation (5.14) implies that GW parameters are univocally fixed by the scalar fluctuation tilt and amplitude. Departures from power law behaviour or an admixture of isocurvature initial conditions would require additional parameters [138].

The evolution of perturbations from these initial state until decoupling involves a set of *physical* parameters, which are specific combinations of standard cosmological parameters.

(i) Relativistic particles at recombination include photons and massless neutrinos. The energy density of radiation is fixed by the current microwave background temperature T_o, while that of the neutrino backgrounds depends on the effective number of massless neutrino species N_ν.

(ii) The magnitude of the Sachs-Wolfe effect depends on the gravitational potentials describing scalar perturbations, which in turn depend on $\Omega_m h^2$, the fraction of critical density as nonrelativistic matter. The gravitational potentials also appear as a forcing term in the oscillator equation describing the acoustic waves in the plasma.

(iii) The baryon density, $\Omega_b h^2$, alters the effective mass in the oscillator equation and reduce sound speed in the plasma (with a slight extra dependence

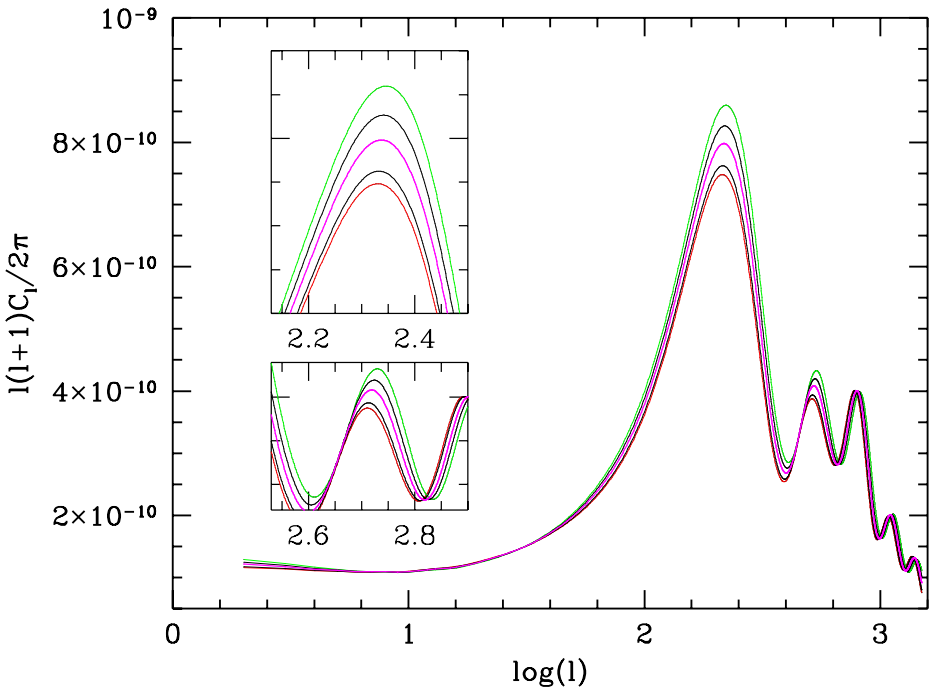

Figure 5.2: Dependence of $C_{T,l}$ spectrum on $\Omega_m h^2$. The magenta curve corresponds to $\Omega_m = 0.3$, $h = 0.7$. Curves above (below) it yield lower (higher) density models; the top green (bottom red) curve is for $\Omega_m h^2 = 0.25$ (0.35). We took $T_o = 2.73$, $N_\nu = 3$, $\Omega_b = 0.04$. In the small boxes, features around the *Doppler* peak and the successive peak are magnified. Notice that the green (red) curve is the top (bottom) one in both plots.

on N_ν). Together this effects lead to an enhancement of the amplitude of oscillations, and a displacement of the equilibrium point, thus breaking the symmetry of oscillations.
(iv) The redshift z_{eq} is then determined by the $\Omega_m h^2$, which in turn affects the size of DM fluctuations, since they start to grow gravitationally only after z_{eq}. Also, the gravitational potentials evolve in time at $z > z_{eq}$ and cease to do so afterward. Hence, the later z_{eq} occurs, the greater the time evolution of the potentials at decoupling, increasing the Integrated Sachs-Wolfe effect.
(v) The horizon size at recombination, which sets the overall scale of the acoustic oscillations and, in particular, the position of the Doppler peak, depends only on the total mass density $\Omega_m h$.
(vii) The scale for diffusion damping depends on the baryon density $\Omega_b h^2$ with a slight extra dependence directly on Ω_b alone.

In summary, the $\hat{T}$ spectrum at last scattering is shaped by the physical parameters $\Omega_m h^2$, $\Omega_b h^2$, $\Omega_m h$, instead by the individual cosmological parameters Ω_m, Ω_b, h. The quality of present data sets allow to constrain several parameters simultaneously. Accurate exploration of such large parameter spaces requires however great computational resources; adopting physical parameter instead of cosmological ones can then lead to improved efficiency. Further de-

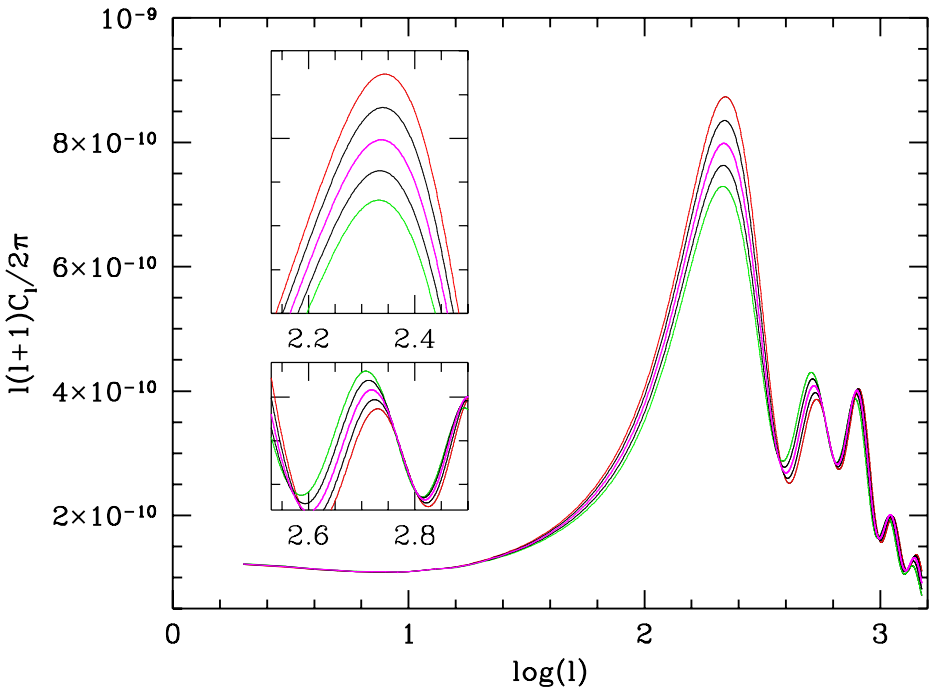

Figure 5.3: Dependence of $C_{T,l}$ spectrum on $\Omega_b h^2$. The magenta curve corresponds to $\Omega_b = 0.04$, $h = 0.7$. Curves above (below) it yield lower (higher) density models; the green (red) curve is for $\Omega_b h^2 = 0.0147(0.0245)$. We took $T_o = 2.73$, $N_\nu = 3$, $\Omega_m = 0.3$. In the small boxes, features around the *Doppler* peak and the successive peak are magnified. Notice that the green (red) curve is the top (bottom) one for the *Doppler* peak and the bottom (top) one for the successive peak: $\Omega_b h^2$ controls the ratio between the heights of the first two peaks.

tails on the way how $C_{T,l}$ depends on these parameters are outlined in the captions of Figs. 5.2–5.3.

5.4.3 Secondary anisotropies and low–z effects

During the path from the LSS to the observer, several effects induce further anisotropies in the photon distribution. These anisotropies are often dubbed *secondary* anisotropies to distinguish them from the primary anisotropies tied to recombination, and usually originate at redshifts much lower than z_{rec}. The main physical sources of secondary anisotropies are:
(i) *Curvature and Dark Energy.* While conceptually distinguished, a non–flat geometry and DE affect the CMB spectra in much a similar way. On large angular scales, the rapid variation of the gravitational potentials associated with the passage from a matter–dominated expansion to a curvature– or DE–dominated expansion marks the APS through the ISW effect. The angular position of the peaks is instead altered due to variations to the angular diameter distance.

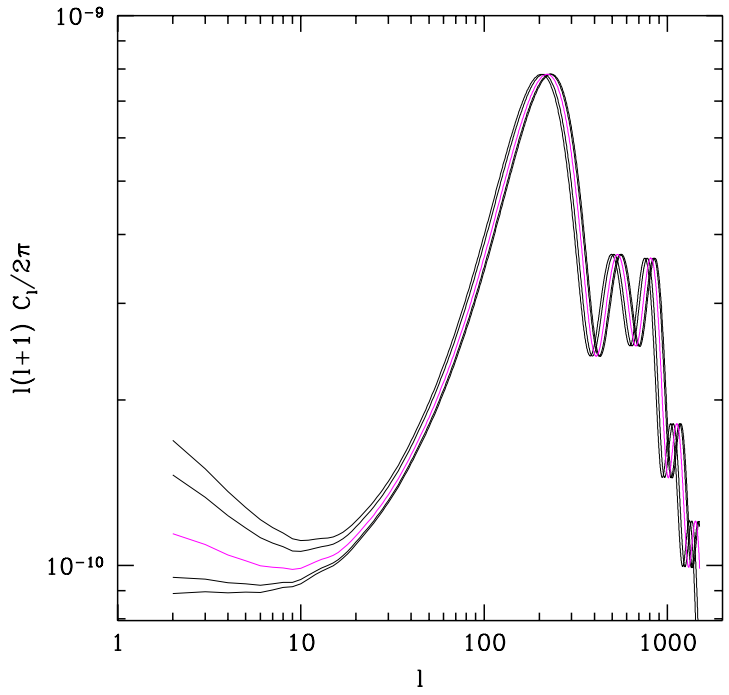

Figure 5.4: Dependence of $C_{T,l}$ spectrum on $\Omega_m h$. The magenta curve corresponds to $\Omega_m = 0.3$, $h = 0.7$. Curves above (below) correspond to lower (higher) density models. Normalization was set so to have equal height for *Doppler* peaks. This shows the gradual displacement to the right of the peaks as $\Omega_m h$ increases.

(ii) *Reionization.* Observations of the Inter Galactic Medium (IGM) show that it is fully ionized at least up to $z \sim 6$. The scattering of CMB photons on free electrons induces further anisotropies in the CMB spectra which, in a first approximation, depend on the total optical depth for Thomson scattering, τ. In the simplest model of a single and instantaneous, or *sharp*, reionization, a non vanishing τ reduces the amplitude of the peaks in $C_{T,l}$ spectra, as the re–scattering smoothers the peaks associated with primary anisotropies, while at largest scales the APS remain almost unchanged.
(iii) *Sunayev–Zel'dovich effect* [139]. CMB photons traversing clusters of galaxies experience inverse Compton scattering on the highly energetic electrons of the Intra Cluster Medium. Scattered photons acquire energy at the expense of the electrons, resulting in a *diminished* temperature of CMBR in correspondence of the cluster, as photons get shifted from microwave to lower wavelengths. The SZ effect alters the high multipoles of the APS ($l \sim 1500 - 2000$).

Aside from these physical effects, APS are modified by the photons' free–streaming, which produces a transfer of power from lower to higher l's. Although it is simply a geometrical effects, free–streaming is fundamental in accounting for large angle polarization.

While each of the physical parameters discussed in this section and in the previous one affect the APS in a precise and predictable way, there exist

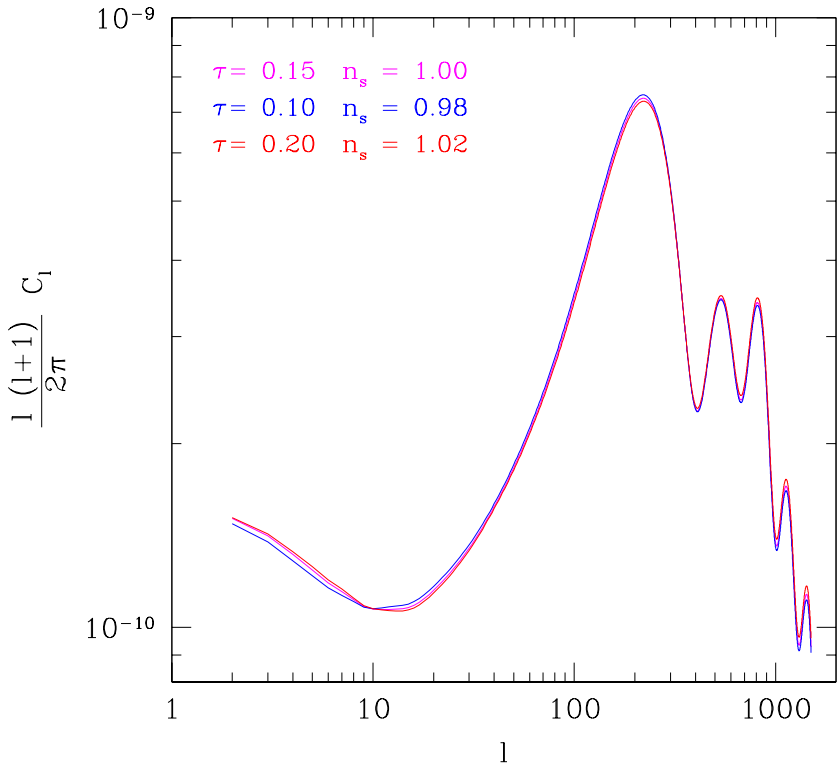

Figure 5.5: Degeneracy of $C_{T,l}$ spectrum with respect to simultaneous changes of n_s and τ.

combinations of parameters which can be changed in such a way as to leave the temperature anisotropies spectrum almost unchanged. As an example of such degeneracies, in Fig. 5.5 we show the effects of simultaneously varying n_s and τ. In this case, polarization measures can help break the degeneracy, in other situations other sorts of data, e.g. analysis of large scale structure, are needed.

5.5 The polarization of the CMB

Photons undergoing Thomson scattering become linearly polarized, as outgoing radiation cannot have an oscillation mode parallel to its direction of propagation. Nevertheless, if the distribution of the radiation incident on an electron is isotropic, the outgoing radiation has no net polarization, as polarization states originating from incident directions separated by 90° balance each other exactly. A similar argument shows that a dipole pattern is not enough to generate net polarization and therefore the incident radiation field needs to have a quadrupole moment [140].

5.5.1 Kinematics of Thomson scattering

Let us consider a (nearly) monochromatic, unpolarized and plane wave of intensity I' incident on a stationary electron. The Thomson scattering cross-section is given by

$$\frac{d\sigma}{d\Omega} = \frac{3\sigma_{Th}}{8\pi}|\vec{\epsilon}' \cdot \vec{\epsilon}|^2 \,, \tag{5.15}$$

where $\vec{\epsilon}'$ and $\vec{\epsilon}$ are unit vectors describing the polarization states of incoming and outgoing waves, respectively. The reference frame is chosen so that the scattered waves propagates along the z–axis direction and label $\vec{\epsilon}_x$ ($\vec{\epsilon}_y$) the polarization vectors of the outgoing wave perpendicular (parallel) to the scattering plane. Likewise $\vec{\epsilon}'_x$, $\vec{\epsilon}'_y$ define the polarization vectors of the incoming wave. Since this is unpolarized, $Q' = U' = V' = 0$ while intensities along the directions defined by $\vec{\epsilon}'_x$ and $\vec{\epsilon}'_y$ are equal, $I'_x = I'_y = I'/2$. The scattered intensities are instead

$$\begin{aligned} I_x &= \frac{3\sigma_T}{8\pi}[I_x\prime(\vec{\epsilon}'_x \cdot \vec{\epsilon}_x)^2 + I_y\prime(\vec{\epsilon}'_y \cdot \vec{\epsilon}_x)^2] = \frac{3\sigma_T}{16\pi} I\prime \\ I_y &= \frac{3\sigma_T}{8\pi}[I_x\prime(\vec{\epsilon}'_x \cdot \vec{\epsilon}_y)^2 + I_y\prime(\vec{\epsilon}'_y \cdot \vec{\epsilon}_y)^2] = \frac{3\sigma_T}{16\pi} I\prime \cos^2\theta \,, \end{aligned} \tag{5.16}$$

where θ is the angle between the incoming and outgoing waves. The Stokes parameters of the outgoing wave are then:

$$\begin{aligned} I &= I_x + I_y = \frac{3\sigma_T}{16\pi} I'(1+\cos^2\theta), \\ Q &= I_x - I_y = \frac{3\sigma_T}{16\pi} I' \sin^2\theta \,. \end{aligned} \tag{5.17}$$

Q and U describe the polarization state with respect to sets of directions rotated by $\pi/4$. To obtain U, then, we can simply rotate the $x-y$ plane by $\pi/4$. The rotated Q will be equal to the U parameter in the original frame. Moreover, Thomson scattering does not induce circular polarization and V remains zero, e.g., [141].

When considering a radiation field instead of a single wave, the net polarization of scattered light is determined by integrating eqs. (5.17) over all incoming directions. Notice that the Stokes parameters of outgoing radiation must be defined with respect to a common reference frame. Therefore, the coordinate system for each incoming direction must be rotated about the z–axis by a suitable angle. We obtain then:

$$\begin{aligned} I &= \frac{3\sigma_T}{16\pi} \int d\Omega (1+\cos^2\theta) I'(\theta,\phi) \,, \\ Q &= \frac{3\sigma_T}{16\pi} \int d\Omega \sin^2\theta \cos(2\phi) I'(\theta,\phi) \,, \\ U &= -\frac{3\sigma_T}{16\pi} \int d\Omega \sin^2\theta \sin(2\phi) I'(\theta,\phi) \,. \end{aligned} \tag{5.18}$$

The outgoing polarization state depends only on the intensity distribution of the unpolarized incident radiation. Expanding the incident radiation field in spherical harmonics,

$$I'(\theta,\phi) = \sum_{\ell m} a_{\ell m} Y_{\ell m}(\theta,\phi), \tag{5.19}$$

leads to the following expressions for the outgoing Stokes parameters:

$$\begin{aligned} I &= \frac{3\sigma_{Thom}}{16\pi}\left[\frac{8}{3}\sqrt{\pi}\,a_{00} + \frac{4}{3}\sqrt{\frac{\pi}{5}}a_{20}\right], \\ Q &= \frac{3\sigma_T}{4\pi}\sqrt{\frac{2\pi}{15}}\mathrm{Re}(a_{22})\,, \\ U &= -\frac{3\sigma_T}{4\pi}\sqrt{\frac{2\pi}{15}}\mathrm{Im}(a_{22})\,. \end{aligned} \tag{5.20}$$

Thus, Thomson scattering of an unpolarized radiation field having a non–vanishing quadrupole moment leads to a linearly polarized outgoing radiation. Notice that eqs. (5.20) hold in the reference frame in which the electron is at rest.

5.5.2 Origin of polarization

At times significantly before decoupling, the Universe is hot enough that protons and electrons exist freely in a plasma. During this epoch, the rate for photons to Thomson scatter off of free electrons is large compared to the expansion rate of the Universe. This tight coupling regimes ensures that the photons' distributions behaves like a fluid and therefore can have only a monopole and dipole terms, while higher momenta are rapidly damped away. Prior to decoupling, therefore, no net polarization can arise.

As recombination proceeds and free–streaming of photons begins, higher momenta gradually switch on. In particular, a quadrupole term forms due to velocity gradients in the photon–baryon fluid across the last scattering surface, e.g., [142]. In fact, photons, coming from regions where the fluid has slightly different velocities, are seen in the rest frame of the electron with an intensity which depends on direction. However, as recombination is a fairly rapid process, only a relatively small fraction of photons become polarized before the Universe become totally transparent to CMB.

Furthermore, a quadrupole moment can only arise after a given scale has entered the horizon. We thus expect that on scales still outside the horizon at recombination, the degree of polarization be small. This corresponds to l's laying below the Doppler peak. On the contrary, on smaller scales, the polarization amount depends on the phase of the fluctuation, when it meets recombination, and is stronger for those scales entering recombination in the kinetic stage.

Following all these effects in detail require numerical integration, however the above arguments allow to qualitatively understand the features of polarization APS. In Fig. 5.6 we show the $\hat{\mathrm{T}}$–, E– and TE– APS for SCDM model. Dotted lines refer to a no–reionization scenario. The E–mode APS show a series of peaks in the range $l \sim 10^2$–10^3, in correspondence of scales that enter the horizon in sonic regime. On this scales $C_{E,l} \sim 10^{-2}$–$10^{-3}\langle C_{T,l}\rangle$, as only a small fraction of photons scatters during the last phases of recombination. On larger scales, no significant quadrupole is present at recombination and the spectrum drastically falls at negligible levels. Moreover, polarization is produced by velocity gradients while temperature anisotropies receive contributions from both density and velocity perturbations, with those from density being the dominant ones. As velocity's and density's oscillations are out of phase, peaks in polarization's APS will have a different position from those of $C_{T,l}$. This arguments also explains why peaks in $C_{E,l}$ increase in height with increasing l, at variance with temperature's spectrum.

This picture is however radically altered when the effects of an early reionization are taken into account. CMB photons can again undergo Thomson scattering on free electron and new polarization can form. If reionization occurs at redshifts $10 < z < 30$, as suggested by recent data, the associated optical depth can be relatively low, due to the low density of electrons with respect to recombination. However, the CMB quadrupole has been greatly enhanced by free–streaming since z_{rec}, and even a low τ can produce a significant signal. As shown by the solid lines in Fig. 5.6, the most noticeable imprint of reionization on CMB is the appearance of new peaks in polarization APS at low l's.

5.5.3 B–modes and lensing

We conclude this Chapter with a brief discussion of B–mode polarization. Density fluctuations, being a scalar field, produce features in CMBR that are invariant under parity transform, and therefore contribute only to $\hat{\mathrm{T}}$, E and TE spectra. Tensor modes, instead, add power to all four APS. Then, detection of *cosmological* B–modes would be direct proof of a background of primordial GW's and yet another hint in favour of Inflation.

Inflationary models predict that GW's rapidly decay on scales below the Hubble radius, therefore we expect the $C_{B,l}$ to be relevant up to $l \sim 200$, and rapidly decrease afterward. In the absence of reionization, the best observational window for B–modes is then $50 \lesssim l \lesssim 200$ (see Fig. 5.7). A non–vanishing optical depth acts on $C_{B,l}$ in much the same way it did on $C_{E,l}$; however, for B–modes the reionization peak has about the same height has the main peak, although being more affected by CV.

Detection of B–modes is impaired by the low–value of the expected signal. The relative contribution to the level of polarization induced by GW's with respect to density fluctuations, depends on the tensor–to–scalar ratio, r, which in turn is fixed by n_s. For realistic values of n_s, the $C_{B,l}$ spectrum is expected

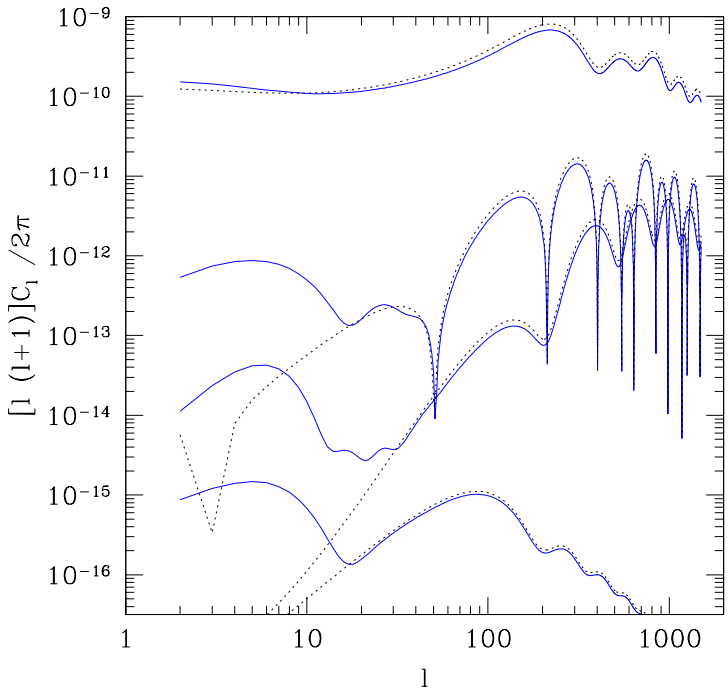

Figure 5.6: Angular power spectra $C_{Y,l}$ for (top to bottom) $Y = T, TE, E, B$, for a ΛCDM model with $\Omega_m = 0.3$, $\Omega_b = 0.05$, $h = 0.7$ and $n_s = 0.99$. Dotted curves refer to a model with no reionization, while solid curves refer to $\tau = 0.17$.The most noticeable effect due to reionization is the appearance of a new peak in the low–l region of polarization APS.

to be 1∼2 orders of magnitude smaller than E–mode spectrum for $l \lesssim 200$.

Despite detection of the B–mode polarization proves to be quite difficult, a large theoretical effort on the study of its properties has been made [123, 143]. In fact, measuring the $C_{B,l}$ power spectrum appears to be, at the moment, the only way to obtain precise enough detection of the tensor perturbations, although some loose constraints are available by the analysis of current anisotropy data [32, 144]. In Inflation models, the amplitude of the tensor perturbations is directly proportional to the energy scale at which Inflation occurred. Then B–mode polarization becomes a probe of GUT–scale physics at 10^{16} GeV [145].

Aside the low intrinsic level of B–modes, further difficulties in detection of tensor modes arise from the effects of *gravitational lensing* on CMB. Lensing by large scale structure induce additional shear and vorticity in the CMB fields, even in the absence of any intrinsic handedness. In particular, lensing causes a leakage between different polarization modes, so that a spurious B–mode can appear.

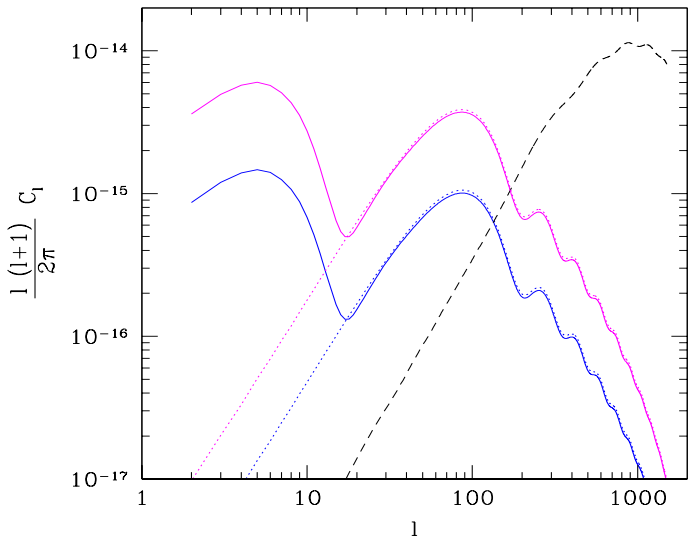

Figure 5.7: B–spectra possible lensing effect. Solid lines are for $\tau = 0.17$. Dotted lines are for $\tau = 0$. The magenta (blue) lines are for $n = 0.95$ (0.99). The black dashed line shows the B–mode generated by lensing the E–mode of the $n = 0.95$ model. Clearly the observational window for the B–mode due to GW's goes up to $l \simeq 100$. Resolving angles $< 3^o$, only allows to confirm the B–mode due to lensing.

It can be shown [146] that lensed APS are related to unlensed ones by:

$$\begin{aligned}
\tilde{C}_{T,l} &= C_{T,l} + \mathcal{W}^{l'}_{1l} C_{T,l'} \\
\tilde{C}_{E,l} &= C_{E,l} + \frac{1}{2}[\mathcal{W}^{l'}_{1l} + \mathcal{W}^{l'}_{2l}]\; C_{E,l'} + \frac{1}{2}[\mathcal{W}^{l'}_{1l} - \mathcal{W}^{l'}_{2l}]\; C_{B,l'} \\
\tilde{C}_{B,l} &= C_{B,l} + \frac{1}{2}[\mathcal{W}^{l'}_{1l} - \mathcal{W}^{l'}_{2l}]\; C_{E,l'} + \frac{1}{2}[\mathcal{W}^{l'}_{1l} + \mathcal{W}^{l'}_{2l}]\; C_{B,l'} \\
\tilde{C}_{ET,l} &= C_{ET,l} + \mathcal{W}^{l'}_{3l}\; C_{ET,l'},
\end{aligned} \tag{5.21}$$

Details of the physical mechanism responsible for lensing are here encoded by the *filter* functions $\mathcal{W}^{l'}_{il}$ $(i = 1, 2, 3)$; their full analytical expressions can be found in [146]. For the purpose of this discussion, it suffices to say that (i) they are oscillatory functions of l' and their main contribution is concentrated around l, and (ii) filters corresponding to different i's, only differ at the % level. Accordingly their differences are much smaller than their sum. The main effect of lensing on $\hat{\mathrm{T}}$, E and TE spectra, therefore, amounts to smearing the l–dependence.

For polarization spectra an additional effect consists in the leakage between different polarization modes. In particular, the third row of eqs. (5.21) shows that gravitational lensing can induce a spurious B–mode even if unlensed $C_{B,lm}$ vanish. Moreover, as the E–mode can surpass the B–mode by more than a factor of 10^2, the term proportional to $C_{E,l}$ can dominate over those proportional to $C_{B,l}$, despite the differences in the magnitude of the respective coefficients.

In Fig. 5.7 the APS of the lensing–induced B–mode is shown by the dashed line. Depending on the value of r, primordial B–modes surpass lensing–induced ones up to multipoles $l \sim 100 - 200$. At higher multipoles, corresponding to angular scales $\sim 1^{\circ}$, detection of B–mode polarization does not provide any insight on inflationary physics.

Additional complications arise in the case of incomplete sky coverage. As shown in sec. 5.2, E and B modes are non–local quantities; if measurements are available only on a finite sky–patch, decomposition of polarization field into electric and magnetic parts is not well defined, and the two polarization modes mix. These leakage is significant on the largest scales probed, and becomes progressively negligible at scales much smaller that the size of the region explored. It is then clear why probing primordial GW's with CMB polarization requires a full sky experiment.

Chapter 6

Gravitational Lensing Constraints on Dynamical and Coupled Dark Energy

Upcoming Weak Lensing (WL) surveys can be used to constrain Dark Energy (DE) properties, namely if tomographic techniques are used to improve their sensitivity. In this chapter, a Fisher matrix technique is used to compare the power of CMB anisotropy and polarization data with tomographic WL data, in constraining DE parameters. Adding WL data to available CMB data improves the detection of all cosmological parameters, but the impact is really strong if the option of a DE–DM coupling is considered; then WL tomography succeeds to reduce the errors on some parameters by factors > 10 .

The results described here are refered in part to a paper published by the author [147].

6.1 Introduction

In the most popular scenario, DE is ascribed to a cosmological constant Λ. However, in this thesis we widely considered the option of a self–interacting scalar field, ϕ (quintessence [148], or dynamical DE [44, 51, 50]), possibly coupled to Dark Matter.

Let me remind that ΛCDM models apparently accommodate all available data systems. The problem being the physical origin of Λ, which arises a *fine tuning* problem, and the *coincidence* problems.

As we saw in previous Chapters, the former problem is eased by dynamical DE (dDE), a scalar field ϕ self–interacting through a *tracking* potential $V(\phi)$ [149]. If $V(\phi)$ is SUGRA [44, 51, 50], the fit with data is at least as good as for ΛCDM [150].

We also outlined in previous Chapters that, in the attempt to ease the coincidence problem, a DM–DE interaction (e.g., [59, 56, 58, 151, 152]) was

also considered, yielding an energy transfer between the dark components, so allowing a (quasi)–parallel scaling of DM and DE from a fairly high redshift until the present.

Lab data set no significant constraint on DM–DE interaction strength, parametrized by β. In chapter 2 we also discussed constraints on possible couplings, arising from SNIa data [153] or the redshift evolution of the Hubble parameter, H [154]. We also saw that massive neutrinos can allow to bypass the limits $\beta < 0.07$–0.10 [155, 156] otherwise set by observations. Values of β widely exceeding 0.2 can be however considered highly unlikely.

Such a low coupling level only partially eases the coincidence problem [157] but, as we said before, once the genie has come out from the lamp, it is hard to put it back inside. The point is whether low values of β, as allowed by current data, can interfere with future data analysis. In particular, when we allow for non–zero β, how do errors on other parameters behave?

Here we try to answer this question by using a Fisher matrix technique. We consider two different models, set by similar values of cosmological parameters, without and with coupling. In the latter case, we took $\beta = 0.1$. Neutrinos are kept massless. Starting from these models, we evaluate the expected errors on cosmological parameters, as obtained when data concern just CMB anisotropy and polarization or include tomographic weak lensing (WL).

As a matter of fact, in coupled models, the time evolution of the dark components is non–standard. We saw that, if such models are considered in a Newtonian approximation, it is as though DM particles had a ϕ–dependent mass. Also for quite low β's, this anomalous scaling leaves an imprint on both the expansion history of the Universe, and the growth of (matter) fluctuations, at the linear and non–linear levels (e.g. [52, 158]).

However, any detected evolution of H can be reproduced through a suitable redshift dependence of DE density ρ_{de} and state parameter w_ϕ, when ϕ approaches m_p (the Planck mass). A risk is that, if matter and dark energy are coupled, fitting observations leads to an estimate of a phantom equation of state ($w_\phi < -1$), even if $w_\phi > -1$ at all redshifts [159].

In principle, this risk can be excluded if the redshift dependence of the growth factor $G(z)$ is also tested, through the increase in number and concentration of bound systems. Data providing information both on $H(z)$ and $G(z)$ are therefore able to discriminate between coupled and uncoupled models. Experiments, or combinations of experiments, probing $H(z)$ and $G(z)$ are then needed.

CMB data, used to constrain coupling [155, 160], place only upper limits on β. The analysis of Ly–α and the matter power spectrum of the 2dF and SDSS surveys [156] does not lead to great improvements. At the available sensitivity level, such data systems provide just weighted integrals of $H(z)$ and $G(z)$, which remain consistent with a rather wide set of options.

On the contrary, gravitational lensing, alone or in combination with CMB data, was already shown to be a powerful tool for the analysis of DE. WL

tomography probes the power spectrum $P(k)$ at different redshifts and is thus well suited to constrain $G(z)$.

Here we aim to put these conceptual points on a more quantitative basis and to deepen the case of coupling, by performing a Fisher analysis of future WL surveys and CMB experiments.

The outline of this chapter is as follow. In Sec. 6.2 we review the basic properties and definitions of dDE models and WL, in Sec. 6.3 we show the results of the Fisher analysis, in Sec. 6.4 we discuss them and in Sec. 6.5 we summarize our findings and draw our conclusions.

6.2 Models and definitions

6.2.1 Interacting Dark Energy

We consider a cosmological model where the DE field ϕ interacts with the cold DM component. We slightly modify the formalism with respect to chapter 2. The model requires the specification of the potential $V(\phi)$ and the function $f(\phi)$ characterizing the coupling. The equation of motion for ϕ then reads

$$\ddot{\phi} + 3H\dot{\phi} = -V^{eff}_{,\phi} \quad \text{with} \quad V^{eff} = V + \rho_c \ . \tag{6.1}$$

Here dots denote ordinary time differentiation, $H(a) = \dot{a}/a$ and ρ_c is DM energy density. In turn, its evolution is governed by

$$\dot{\rho}_c + (3H + C\dot{\phi})\rho_c = 0 \ , \qquad \text{with} \qquad C(\phi) = \frac{d\log(f)}{d\phi} \ . \tag{6.2}$$

This equation can be integrated and gives:

$$\rho_c(a) = \rho_{c,0} a^{-3} f(\phi) \ . \tag{6.3}$$

For $f = 1$ eqs. (6.1), (6.3) return ordinary dDE equations. The equations for the other components remain unchanged. In a generic coupled model, then, the ratio between the energy densities of cold DM and baryons is not fixed, but evolves in time according to $f(\phi)$.

However, it is always possible to define an effective DE component of density

$$\rho^{eff}_{de}(a) = \rho_c a^{-3}[f(\phi) - 1] + \rho_{de}(a) \ . \tag{6.4}$$

In general, $\rho^{eff}_{de}(a)$ is not guaranteed to be positive and detecting $\rho^{eff}_{de}(a) < 0$ would be a clear indication that our description of the dark sector is not adequate. Lacking such clear giveaway, however, experiments probing $H(z)$ can hardly discriminate between DE–DM interaction and an *ad hoc* DE component. If its effective state parameter w^{eff} $(= p^{eff}/\rho^{eff})$ is < -1, data may appear to require phantom DE (see [161] for discussion).

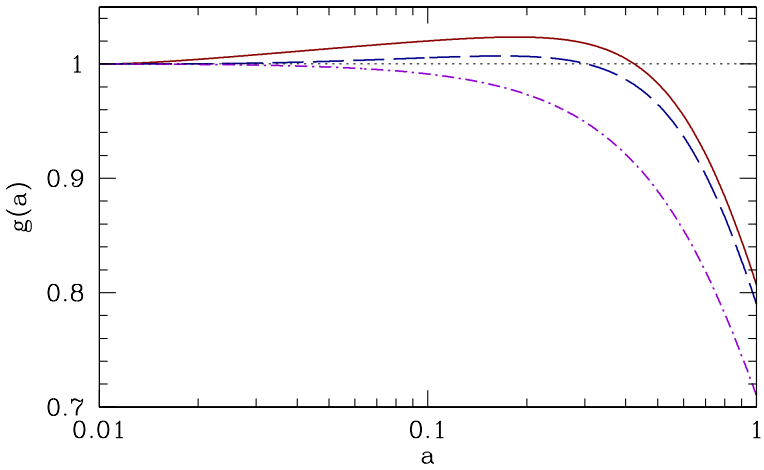

Figure 6.1: The growth suppression rate $g(a) \equiv \delta(a)/a$ for CDM (solid line) and baryons (dashed line) in a coupled model. Curves refer to a SUGRA potential with exponential coupling. It can be noticed that the cold dark matter evolution rapidly diverges from the standard cold dark matter solution, $g(a) = 1$ (dotted line), even well into the matter dominated era. For comparison, we also plot $g(a)$ for the same SUGRA model with coupling turned off (dot–dashed line).

Coupling affects also fluctuation growth. In the Newtonian limit, *i.e.* well below the horizon, and neglecting the contribution of radiation, baryons and DM fluctuations grow according to the equations (e.g. [52, 158, 162]):

$$\begin{aligned} \ddot{\delta}_{\rm b} + 2H\dot{\delta}_{\rm b} &= 4\pi G(\rho_{\rm b}\delta_{\rm b} + \rho_c\delta_c) \\ \ddot{\delta}_c + 2H\dot{\delta}_c &= 4\pi G\left[\rho_{\rm b}\delta_{\rm b} + (1+\tfrac{4}{3}\beta^2)\rho_c\delta_c\right], \end{aligned} \tag{6.5}$$

where we defined β so that

$$C(\phi) = 4\sqrt{\frac{\pi}{3}}\frac{\beta(\phi)}{m_p}, \tag{6.6}$$

while $m_p = G^{-1/2}$. Therefore, baryons and DM perturbations grow at different rates and, even soon after recombination, a growing mode $\delta \propto a$ no longer exists (see Fig. 6.1), leading to a bias between baryon and DM perturbations. Analytical models of spherical collapse have shown that this differential growth results in a baryon–DM segregation, with baryons occupying the outer regions of collapsed objects [163].

Eqs (6.5) also show that the growth equations explicitly depend on both H and ρ_c; therefore, if we measure the growth from data, a possible anomalous scaling can no longer be masked though an *ad–hoc* definition of an effective DE density. It is then licit to conclude that experiments probing the rate of growth of fluctuations are in principle well suited to test coupling between the dark components.

Here we are interested to combining WL and CMB data, which cannot be accurately described using current parametrizations [164]. Therefore, we follow a more conventional approach and choose the functional forms

$$V(\phi) = \frac{\Lambda^{4+\alpha}}{\phi^{\alpha}} \exp\left(4\pi \frac{\phi^2}{\mathrm{m}_{\mathrm{PL}}^2}\right) , \qquad f(\phi) = \exp\left(\beta \sqrt{\frac{8\pi}{3}} \frac{\phi_0 - \phi}{\mathrm{m}_{\mathrm{PL}}}\right) \quad (6.7)$$

The SUGRA [44, 51, 50] potential $V(\phi)$ depends on the slope α and the energy scale Λ. Fixing DE density today and Λ (α), however, determines a unique value of α (Λ). CMB, SNIa and deep sample data yield $\Lambda \lesssim 10^3$GeV [150], in the absence of coupling. Here we focus on the SUGRA potential as it naturally arises in the context of Supergravity Theories and is an example of tracking potential characterized by a rapid time variation of the equation of state, when DE becomes dominant. Therefore, assuming a constant w for this class of potential may lead to misleading results. Different choices for the potential are clearly possible.

The coupling function $f(\phi)$ depends on β, and ϕ_0 is the field value today. In this work we assume a constant $\beta \geq 0$ (see however [161] for a different approach); data place the upper limit $\beta \lesssim 0.12 - 0.15$ [155, 156]. For reasonable values of the cosmological parameters and of Λ, we expect coupling effects not to be relevant for $\beta \lesssim 0.01$, so that the dynamically interesting values for the coupling lies in the range $0.01 < \beta < 0.10$.

6.3 Forecasts for Future Experiments

We present here the results of the Fisher analysis of future experiments, considering both WL and CMB measurements. For definiteness we assume a fiducial WL survey with characteristics similar to those of the recently proposed DUNE project [165]. We assume a redshift distribution of the form (4.41) with $A = 2$, $B = 1.5$ and $z_0 \simeq z_m/1.412$, corresponding to a median redshift of the survey $z_m = 0.9$ (see [166]), and a mean surface density of galaxies $n_g = 35\,\mathrm{arcmin}^{-2}$. The full survey, covering half of the sky ($f_{sky} = 0.5$), is divided into $N = 5$ redshift bins, with $p(z_{ph}|z)$ given by equation (4.40) and $\sigma_z(z) = 0.05(1+z)$.

We consider lensing multipoles up to $\ell_{\mathrm{max}} = 20000$, since we find that results do not depend significantly on larger ℓ. However, one should bear in mind that when considering scales $\ell \gg 1000$ there could be some non–linear and baryonic effects on the matter power spectrum, and so on the WL spectrum [167]. These effects, not yet well understood, could be important for forecasts. However, in this work we suppose these effects to be negligible.

For CMB data, we consider an ideal experiment with characteristics based on the 143GHz PLANCK channel: angular resolution $\theta_{\mathrm{fwhm}} = 7.1'$ and sensitivity $\sigma_{\mathrm{T}} = 42\mu\mathrm{K}\,\mathrm{arcmin}$, $\sigma_{\mathrm{P}} = 80\mu\mathrm{K}\,\mathrm{arcmin}$.

The cosmological model we consider is characterized by 7 parameters with

Table 6.1: Estimated errors on model parameters.

	CMB		WL		WL+CMB	
	SUGRA $\beta = 0.$	SUGRA $\beta = 0.1$	SUGRA $\beta = 0.$	SUGRA $\beta = 0.1$	SUGRA $\beta = 0.$	SUGRA $\beta = 0.1$
$100*\omega_{\rm b}$	0.016	0.019	0.5	0.9	0.011	0.012
$\omega_{\rm m}$	0.002	0.006	0.016	0.03	0.0004	0.0005
$\Omega_{\rm m}$	0.05	0.12	0.002	0.0014	0.0011	0.0014
n_s	0.004	0.005	0.012	0.018	0.0014	0.0021
σ_8	0.07	0.13	0.0026	0.0029	0.0017	0.0016
λ	7.2	9.5	0.89	1.1	0.28	0.28
β	–	0.04	–	0.018	–	0.0016
τ	0.005	0.006	–	–	–	–

fiducial values:

$$\vec{\theta} = \{ \quad \omega_{\rm b} = (0.045 \cdot 0.7^2),\ \omega_{\rm m} = (0.30 \cdot 0.7^2),\ \Omega_{\rm m} = 0.30,\ n_{\rm s} = 1.00,$$
$$\sigma_8 = 0.8,\ \Lambda_{\rm DE} = 5 \cdot 10^{-3}{\rm GeV},\ \beta = 0.1\ \}.$$

Here $\Omega_{\rm m}$ represents the current total (CDM + baryons) matter density in units of the critical density; $\omega_{\rm b} \equiv \Omega_{\rm b}\, h^2$ and $\omega_{\rm m} \equiv \Omega_{\rm m}\, h^2$ are the physical baryons and total matter densities, respectively; $n_{\rm s}$ is the slope of the primordial power–law spectral index of density fluctuations; σ_8 is the rms mass fluctuation in spheres of $8h^{-1}$ Mpc radius while $\Lambda_{\rm DE}$ and β were defined in Sec. 6.2.1. Let us notice that the class of DE models considered here reduces to ΛCDM for $(\Lambda_{\rm DE})^4 \simeq 10^{-47}{\rm GeV}^4$ and $\beta = 0$. Moreover, the fiducial values of DE parameters $\Lambda_{de} = 5 \cdot 10^{-3}$GeV and $\beta = 0.1$ are chosen in order to reproduce at $z = 0$ an effective equation of state which mimics the case of ΛCDM model, $w = -0.95$. Finally, when dealing with CMB data, we also need to fix the value of the optical depth to reionization, $\tau = 0.10$.

We compute the CMB anisotropies (temperature and polarisation) power spectra and the transfer functions, used to calculate linear matter power spectrum, using a modified version of CAMB [135]. To evaluate the non–linear matter power spectrum, P_{NL}, we employ the prescription by Smith *et al.* [96]. This is only tested for model with a cosmological constant; as we are concerned here with Fisher matrix estimates assume that the results of [96] can be extended to coupled models simply by taking into account the non–standard scaling of ρ_c (eq. 6.3). Numerical derivatives were evaluated considering a 5% stepsize, except for $\Lambda_{\rm DE}$, where we adopted a 5% stepsize on $\lambda \equiv Log_{10}(\Lambda_{\rm DE}/{\rm GeV})$.

6.3.1 CMB measurements

Table 6.1 lists the estimated errors on the various parameters considered. For each data set, we compare forecasts for the target model with results for a

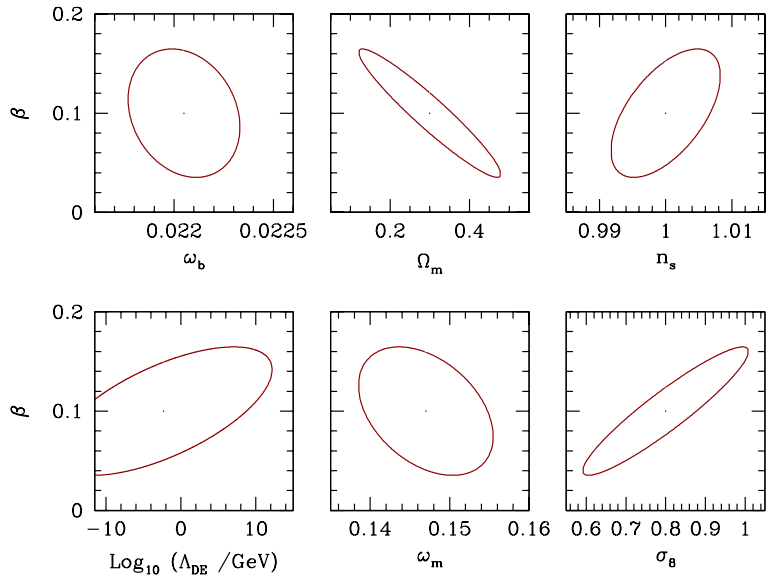

Figure 6.2: Forecasts of joint 1–σ confidence regions on the coupling parameter $\beta = 0.1$ and selected parameters, for a PLANCK–like experiments, after full marginalization over the remaining parameters.

SUGRA model with the same values of the relevant parameters. The table clearly shows that a PLANCK–like experiment is able to provide a measurement of a direct DE–DM interaction at 68% confidence level, even for moderate values of the coupling strength β. However, we expect that at 90% confidence level data will still be compatible with $\beta = 0$.

In any case, allowing for a direct interaction strongly degrades the experimental sensitivity on the parameters characterizing the matter density and the normalization of the primordial spectrum of density fluctuations. Errors on these quantities increase by a significant amount.

Figure 6.2 shows the joint 68% confidence regions between β and each of the other parameters, except for τ, considering only CMB data. In each plot we marginalized over the parameters not shown. β is strongly correlated with most parameters considered here, with the exception of ω_b (and τ), thus introducing additional degeneracies in actual data analysis.

A detailed characterization of these degeneracies would require a different approach than that followed here (e.g. Monte Carlo Markov Chains simulations). We just point out that they can be understood recalling that the heights of the acoustic peaks of CMB spectra are sensitive to the total matter density and to baryon/dark matter ratio at last scattering. In coupled models, these quantities are not univocally determined by their present day value, but strongly depend on β. In addition, the total growth between the last scattering epoch and today is strongly sensitive to β, resulting in a clear degeneracy between β and σ_8.

Let us notice that, as we are concerned with a combination of CMB and WL data, the parameter set is not optimized for CMB experiments. Using

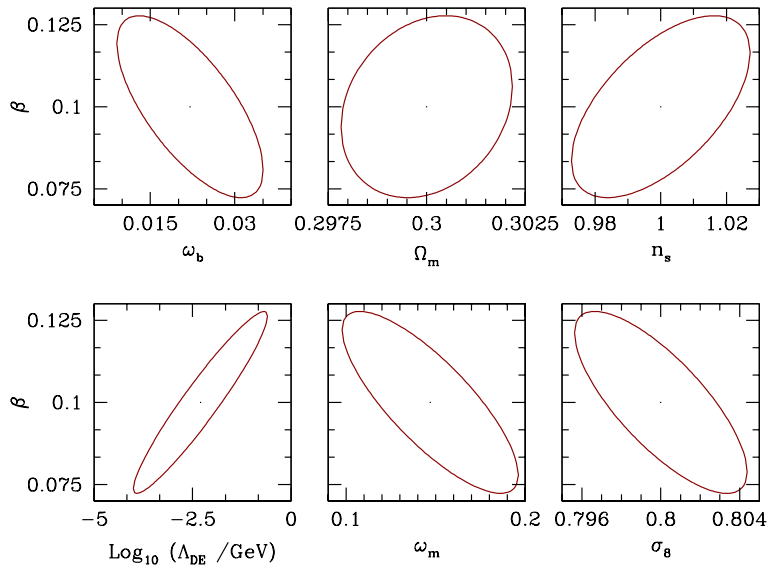

Figure 6.3: Forecasts of joint 1–σ confidence regions on the coupling parameter $\beta = 0.1$ and selected parameters, for a DUNE–like experiments, after full marginalization over the remaining parameters. Notice the change of scales with respect to Fig. 6.2

a different parametrisation can alter error estimates and/or the degeneracies between the various parameters. In particular, CMB data are better described in terms of the angle subtended by the acoustic horizon at recombination, θ, and the amplitude of the primordial spectrum of density fluctuations A_s, rather than in terms of Ω_m and σ_8. This results in large errors on the latter parameters, when CMB data alone are considered. Adopting a set of parameters better suited to the analysis of CMB data results in slightly lower error estimates overall, but the effects of coupling are largely unchanged.

6.3.2 Weak Lensing

The covariance between the power spectra $P^{\rm obs}_{(ij)}(\ell)$ and $P^{\rm obs}_{(mn)}(\ell')$ is approximately given by

$$\mathrm{Cov}\left[P^{\rm obs}_{(ij)}(\ell),\, P^{\rm obs}_{(mn)}(\ell')\right] = \frac{\delta_{\ell\ell'}}{(2\ell+1)\Delta\ell f_{sky}}\left[P^{\rm obs}_{(im)}(\ell)\, P^{\rm obs}_{(jn)}(\ell') + P^{\rm obs}_{(in)}(\ell)\, P^{\rm obs}_{(mj)}(\ell')\right] \tag{6.8}$$

where f_{sky} is the sky fraction covered by the survey and $\Delta\ell$ is the bin width centred at ℓ. The above expression assumes that the power spectrum in each multipole bin is very flat, in order to replace the value of the spectrum evaluated at the bin center with the average of spectrum over each bin (see A.2 for the complete expression). In addition, we have not included the non-Gaussian term, due to the contribution of the shear trispectrum [168, 169].

Figure 6.3 is analogous to figure 6.2 for our target weak lensing survey. Together with Table 6.1, these results show the great potential of WL surveys in

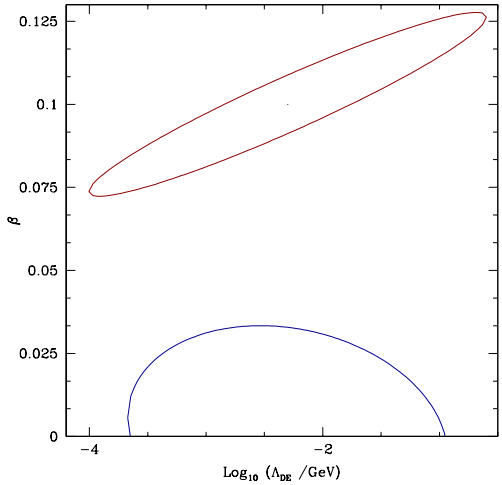

Figure 6.4: Comparison between the 1–σ confidence regions of a coupled SUGRA model with $\beta = 0.1$ (red) and a non–coupled SUGRA model with $\beta = 0$ (blue) for a WL experiment. It is clearly possible to distinguish between the two models.

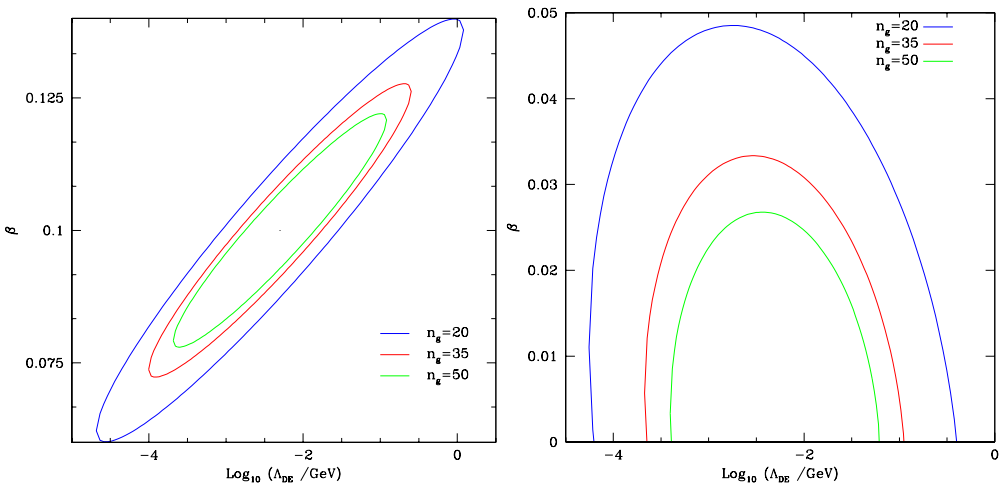

Figure 6.5: Joint 1–σ confidence regions on β and $\Lambda_{\rm DE}$ after marginalization over the remaining parameters, for different number of galaxies n_g. On the left SUGRA coupled model with $\beta = 0.1$, on the right SUGRA coupled model with $\beta = 0$ and β derivatives calculated only on one side, for positive values of the parameter.

constraining interacting DE models. Marginalized errors on β and λ are of the order of $\sigma(\beta) \simeq 0.02$ and $\sigma(\lambda) \simeq 1$; these figures represent a factor of 2, or more, improvement over Planck estimates. WL data alone can clearly distinguish the target model from a non–coupled model or a cosmological constant even at the 3σ-level, *viceversa* assuming a reference SUGRA model with $\beta = 0$, we can expect to put an upper limit $\beta \lesssim 0.03$, at the same confidence level (see fig. 6.4).

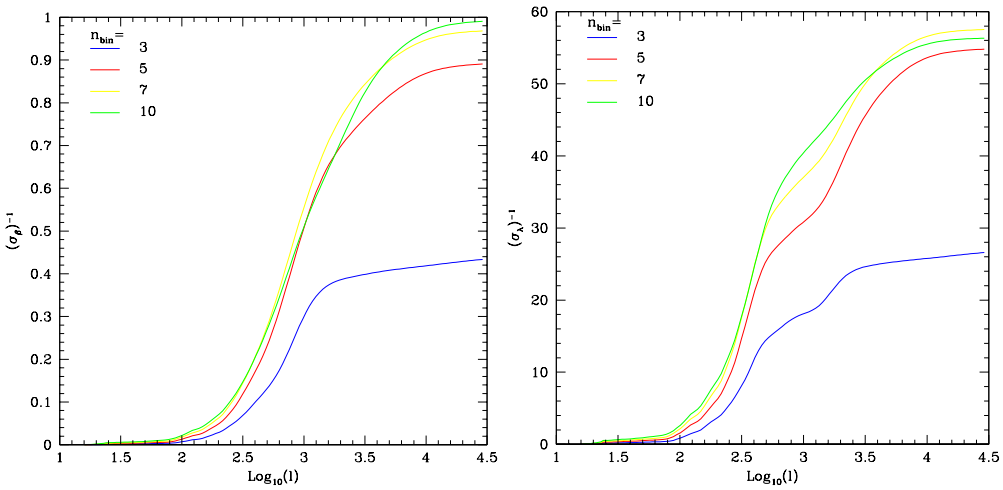

Figure 6.6: Inverse error as a function of the maximum multipole for the WL survey, for different numbers of redshift bins. Left panes show results for β, right panel refers to λ.

As expected, WL surveys perform significantly better than CMB experiments also with respect to parameters specifying the current matter density, Ω_m and σ_8. Moreover, constraints on these parameters are not significantly affected by the coupling degrees of freedom. Errors on the remaining parameters, instead, increase by a factor of ~ 2. Finally, we consider a combination of CMB and WL data. CMB and WL probe very different epoch of the Universe and are sensitive to different combination of cosmological parameters. Considering both CMB and WL data allows to constrain the DE parameters with a few percent accuracy, and significantly reduces the degeneracies introduced by DE coupling. In this case, the errors on the cosmological parameters are very similar in both models considered, with the exception of n_s.

Next we considered how our results depend on the characteristic assumed for the target survey. In fig. 6.5 the impact of mean surface density of galaxies on the determination of β and λ. With $n_g = 25\,\mathrm{arcmin}^{-2}$ constraints on β degrades by $\sim 50\%$, while $n_g = 50\,\mathrm{arcmin}^{-2}$ gives only a marginal improvement on expected errors; constraints on λ are similarly affected. However, even in the worst case considered here, next generations WL survey will provide an improvement over the information that we are likely to obtain from PLANCK data.

Lastly, we consider the dependence of our results on the number of bins and the multipoles range considered. In fig. 6.6 we plot the inverse of the expected variance on β and λ as a function of the maximum multipole considered in the analysis and for different number of bins. With 3 redshift bins, the precision on both parameters depends mostly on multipole up to a few thousands; smaller scales do not provide a significant contribution. Dividing the survey in 5 bins strongly improves the constraints on both parameters and allows to exploit

information from multipoles up to ~ 10000. For a DUNE–like survey, a further increase in the number of bins does not lead to significant improvements on the constrains on coupled models parameters.

It must be outlined that these results assume that the theoretical framework used to predict the matter power spectrum on intermediate ($1h\mathrm{Mpc}^{-1} \lesssim k \lesssim 20h\mathrm{Mpc}^{-1}$) and small ($k > 20h\mathrm{Mpc}^{-1}$) scales can accurately account for the effects of baryons on non–linear structures. In general, the fitting formulas used to predict the non–linear power spectrum are calibrated using dissipationless N–body simulations and, therefore, do not properly describe baryonic structures. While baryons make up $\simeq 15 - 20\%$ of the matter in the Universe and on large scales are expected to trace the DM field, their distribution inside halos is significantly different from DM. In turn, this alters the shape of the non–linear power spectrum on the corresponding scales, and the possibility of extracting precision constraints from $P_{\mathrm{NL}}(k)$ hinges on our capability of accurately modeling baryon physics [167]. However, simulations do not yet have the accuracy required for precision constraints and the problem is even more serious for the coupled models considered in this work. Modelling non linear stages though spherical growth, Mainini [170] showed that baryons and DM will be however differently distributed, even independently of the onset of gas dynamics. N–body simulations of cDE models were performed [171], by using a Ratra–Peebles [43] potential; hydro simulations, instead, were never produced. Should accurate prediction be still unavailable for the analysis of a DUNE–like experiment, a more conservative cutoff of $l \simeq 1000$ would be required. Figure 6.6 shows that in this case the expected errors on Λ and β would increase by a factor ~ 2.

6.4 Discussion

All previous analysis shows that, even if we admit quite a little DM–DE coupling, we open a Pandora's box, leading to a severe degradation in our capacity to deduce cosmological parameters from a given set of measures.

As a matter of fact, coupling destroys our trust that the period between the recombination and the start of DE relevance is under control. If coupling is absent, during such period SCDM is a fair approximation. Let us then remind what happens to the growth factor, as soon as coupling is onset: Figure 6.1 shows that: (i) deviations from SCDM are significant already when $a \sim 0.02$; (ii) they are then different for DM and baryons; (iii) they work in the opposite direction, in respect to the effects of a DE components.

As far as the growth factor is concerned, a tiny coupling is able to overwhelm a huge DE amount, with compensation occurring for $a \sim 0.3$–0.4 , however keeping always $g(a)$ at values greater by ~ 10–$15\,\%$. Altogether, growth is faster in coupled models. Hence, if we do not include the information that coupling is zero in the fit, we can find an agreement between data and a wider range of DE amounts.

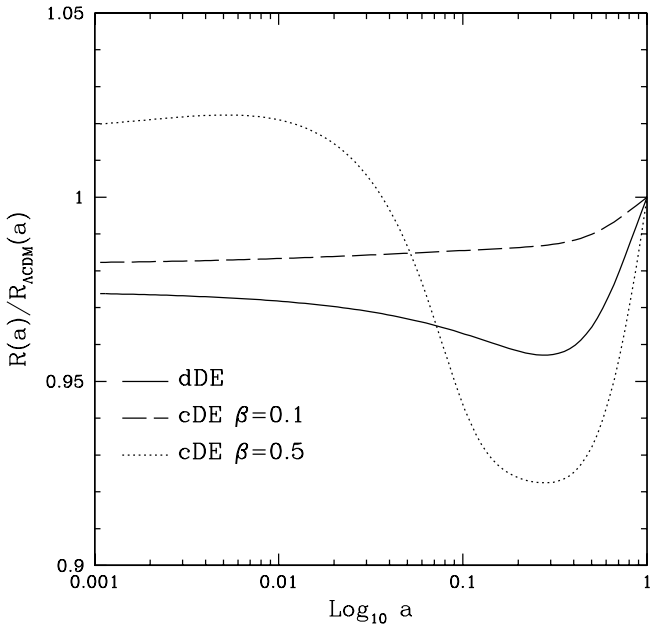

Figure 6.7: Scale dependence of comoving distances in coupled or uncoupled SUGRA cosmologies, compared with ΛCDM. The case $\beta = 0.5$, corresponding to a rather strong DM–DE coupling is also shown.

Similar points can be made for the comoving radial distance $R(z) \equiv r(0, z)$. In Figure 6.7 we compare comoving distances for ΛCDM with various cosmologies. The Figure shows that dDE, in the absence of other parameter shifts, sets the Last Scattering Band (LSB) closer to the observer. Once again, a mild coupling acts in the opposite direction and tends to re-set the LSB at the distance it had in ΛCDM. In the Figure we consider the behavior of distances also for a rather strong coupling, $\beta = 0.5$. Then the distance behavior is different in the period when DE density can be neglected, in respect to the epoch when DE and DM have similar densities. The key point, however, is that the LSB becomes then farther from the observer. When fitting CMB data to such models, in order to compensate such effect, the value of H_o tends to be increased. Strong coupling therefore yields a large Hubble parameter estimate.

Figures 6.8 finally show the scale dependence of the density parameters in the different models. Once again, when DE is mildly coupled, a behavior more similar to ΛCDM is recovered. On the contrary, when considering a greater coupling strength, we see that DE and DM keep similar densities up to a fairly large redshift. This was indeed the initial motivation of cDE cosmologies.

Altogether, these Figures indicate that adding a small coupling reduces the effects of the very passage from ΛCDM to dDE; owing to the excellent fit that ΛCDM cosmologies have with data, this tells us that only highly refined CMB data will be able to test the possibility that a mild DM–DE coupling exists.

On the contrary, a stronger coupling, although easing the coincidence problem, displaces several observables in a unacceptable way.

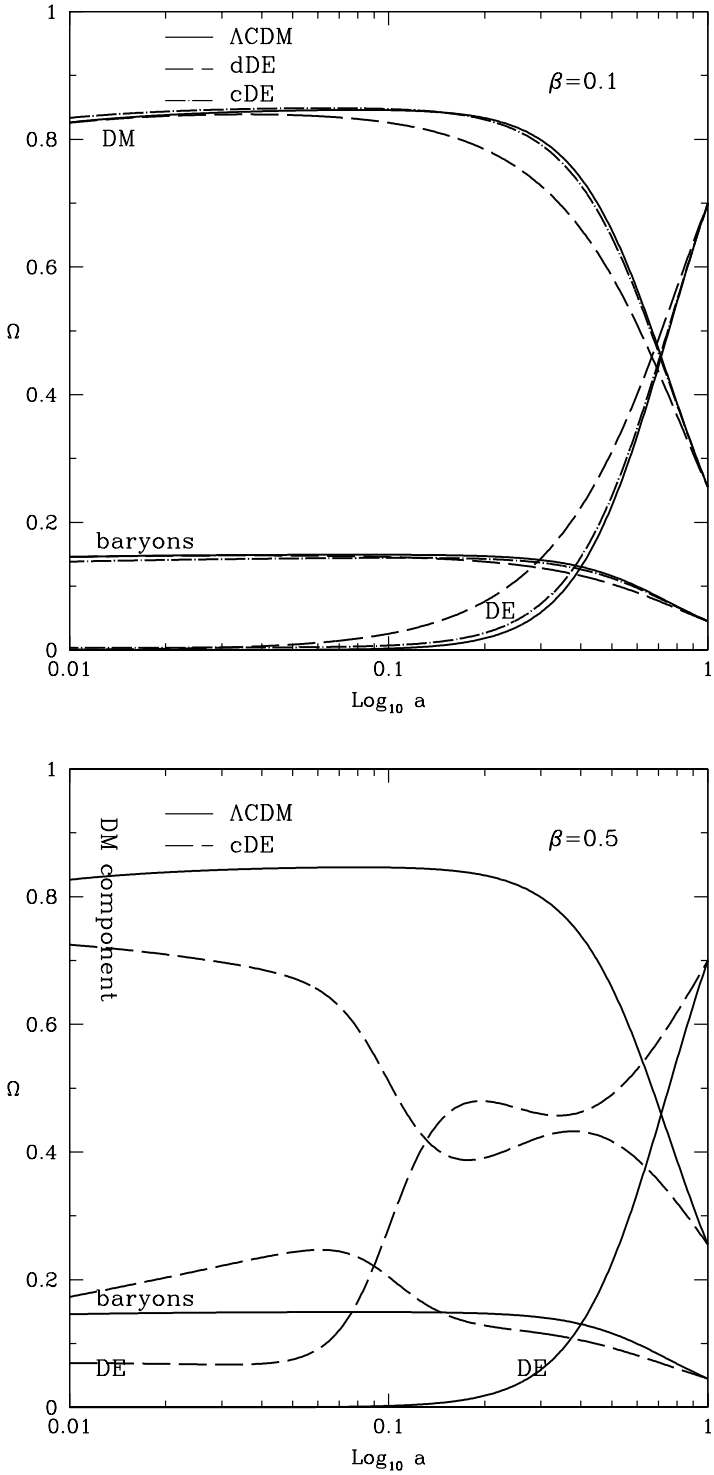

Figure 6.8: Scale dependence of the density parameters of the various components in ΛCDM. compared with other models. In the upper panel uncoupled and weakly coupled SUGRA models are considered. For the sake of comparison, in the lower panel we also show the effects of choosing a stronger coupling.

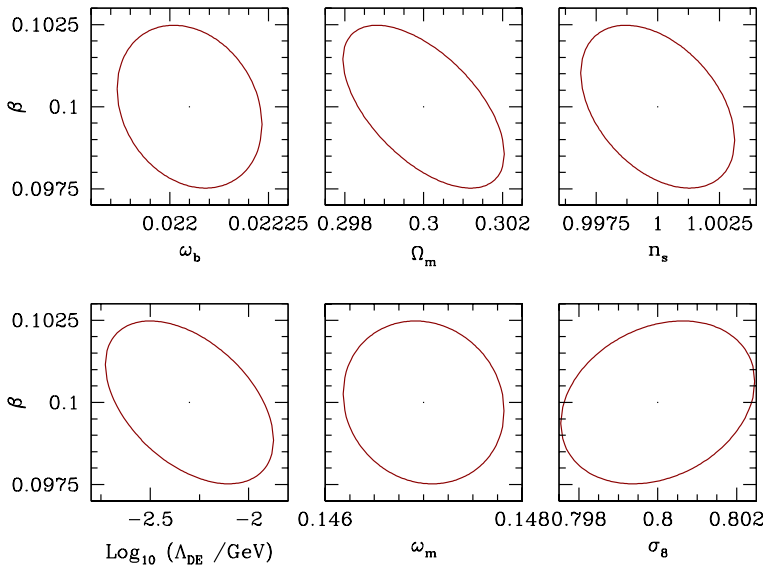

Figure 6.9: Forecasts of joint 1–σ confidence regions on the coupling parameter $\beta = 0.1$ and selected parameters, for a combination of a PLANCK–like and a DUNE–like experiment, after full marginalization over the remaining parameters.

6.5 Summary and Conclusions

Future WL surveys will certainly put more stringent constraints on cosmological parameters and will be crucial to break quite a few degeneracies between parameters.

Within this context, in this chapter we focused on coupled DE models with a twofold aim. Detecting a signal of DM–DE coupling would be certainly decisive to fix the nature of the dark components. Henceforth, determining the level of sensitivity needed to appreciate such an effect, is crucial in setting the appeal of forthcoming projects. There is however a complementary aspect which deserves much attention. In order to convert raw data into physical information, a set of parameters, spanning a variety of models, is to be fixed; a bias on parameter selection, however, can lead to an optimistic estimate of the confidence level for the best fitting model, far from reality.

In this work, we focused on this kind of danger, when we open the option of DM–DE coupling. Even if such coupling is absent or quite weak, we showed that just considering its possibility may widen the error bars for a number of parameters, also apparently unrelated to the coupling itself. In a sense, when a new degree of freedom is opened, such an effect is natural and expected. Coupling, however, has really a major impact, affecting different parameters for the different observables considered here; moreover, its impact is drastically reduced when we work out parameter values by using simultaneously both observables.

Before outlining our main conclusions it is however worth reminding a tech-

nical limit we had to face. While CMB predictions depend on linear spectra, the WL spectrum is limited to its non–linear shape. For the purpose of the present analysis, we assumed that prescription for ΛCDM models [96] can be trivially extrapolated to coupled models, so enabling us to estimate the non linear spectrum once the linear spectrum is known. Let us however remark that the shift was estimated from quite a wide set of ΛCDM simulations. Simulations of cosmological models with state parameters $w \neq 1$, although performed by several authors, are still not so extensively studied as ΛCDM; let alone coupled DE simulations: in this case the only available simulations are due to [171] and deal with a potential $V(\phi)$ different from SUGRA.

However, differences between prescriptions for ΛCDM and dDE are small [172] and it seems however clear that model differences can most affect the rate of evolution of halo concentration, slightly shifting the scale where non–linearity effects become significant. The use of more precise prescriptions can therefore only cause minor variation on the estimated errors and, although welcome, such simulations are not expected to interfere substantially with our conclusions.

Our estimates were based on assuming that a photometric survey is available, with $\sigma_z(z) = 0.05(1 + z)$ and a median redshift $z_m = 0.9$, covering half of the sky ($f_{sky} = 0.5$). These features are similar to the recently proposed DUNE experiment. We also compared and combined results from WL with the constraints expected for an ideal Planck–like experiment. The basic results of our calculations are quoted in table 6.1 which is one of the main results of this work.

A first set of conclusions concerns an ideal CMB experiment considered by itself. In this case, introducing coupling degrees of freedom is crucial for the error estimates on some of parameters, also apparently unrelated to coupling. In particular, while the error on ω_b keeps $\sim$1%, the errors on ω_m and σ_8 increase from 1.3% to 3.9% and from 9% to 16%, respectively.

From a physical point of view, the option opened by coupling is that expansion rate and fluctuation growth, from the last scattering band to the observer's site, is non–standard (*e.g.*, the proportionality law $\rho_m \propto a^{-3}$ could be mildly violated). Although CMB data themselves set stringent limits on such deviations, this widens the volume of the parameter space consistent with a given data set; in particular, it increases the likelihood of values of H_0 that would otherwise be negligible and, because of the intercorrelation amongst parameters, this reflects immediately on ω_m and Ω_m estimates.

Similar effects occur in WL experiments, although involving different parameters. Such experiments are a direct test of Ω_m, whose estimated error is reduced by a factor > 30 in respect to a CMB experiment. When the coupling option is opened, the error on Ω_m does not increase; on the contrary, it becomes easier to attribute raw data uncertainties to other parameters and, although marginally, the error on Ω_m becomes somehow smaller.

A completely new situation occurs if both CMB and WL measurements

are simultaneously used. In this case, the opening of the coupling option causes just a marginal increase of the errors on most parameters. This is a clear indication of the complementarity of the CMB and WL measurements, as described in [19] and one of our conclusion is that the combination of these observables, besides of providing parameter values independent of β, can set a (nearly–)final word on the coupling option.

As a matter of fact, by comparing fig. 6.2, 6.3 and 6.9, we see that, when joining CMB and WL results, the degeneracies, between β and σ_8, as well as between β and Ω_m, disappear. Breaking degeneracies is the main aim when different observables are simultaneously considered. We see that, from this point of view, the efficiency of using both CMB and WL measures can be hardly overestimated.

Let us then focus on the case of the spectral index of scalar fluctuations. When both CMB and WL data are used to constrain n_s, a sharp reduction of errors occurs. No surprise that CMB data, by themselves, reflecting the state of the universe before the onset of non linear processes, were more efficient to constrain n_s, with or without coupling, than WL measures. Joining together the two observables, we then see errors to decrease from 0.4% and 1.2% down to 0.16%, in the uncoupled case; in the presence of coupling we have a similar behavior, with errors passing from 0.5% and 1.8% down to 0.25%. The error level achieved, in both cases, is exceptional, even for precision cosmology, and clearly suggests to relieve the constraint of a single n_s value, so inspecting its possible scale dependence, with realistic possibilities to find a direct insight into the nature of the inflationary potential.

In conclusion, future WL surveys could really allow a significant step forward in the comprehension of the dark cosmic side; we can adfirm that, when they will be available, the endeavour to put the genie back inside the lamp will approach a full success.

Chapter 7

Conclusions

This thesis and my work during the PhD years were dedicated to the analysis of the Dark Side of the Universe. Its very existence is probably one of the main discoveries of the XX century.

One basic question, still unanswered, is whether the Dark Side is really made of physical *substance*, or its claimed existence just indicates that lab scale and planetary scale laws are to be modified when going to galactic or even greater scales.

Until the late Nineties, data required a Dark Side however made of *particles*, although related to physics beyond the standard model of elementary interactions. Neutralinos (χ) and invisible axions were considered the most likely candidates. In mixed models also a *hot* component was included, presumably arising from a tiny mass of some neutrino species; still a particle component.

Even at that time there were attempts to get ride of such weakly interacting massive particles (WIMP) by suitably modifying gravity. In spite of the efforts of a significant number of researchers, theories like MOND however failed to meet some of the observational data and are to be rejected.

Then SNIa data surprised the scientifical community, indicating that the whole cosmic contents have an *anti*–gravity effect, causing an acceleration of the expansion, rather than its slowing down. Incidentally, this made obsolete most of the discussions about the value of the spatial curvature K, in FRW metrics: indipendently of its value, the cosmic expansion is doomed to last forever. There was some difficulty to accept SNIa evidence. Their Hubble plot, setting apparent luminosity *vs.* redshift, could be drown only after suitably cleaning raw data by a significant burden of foreground contaminations. The "hope" that the key of the astonishing conclusion could be found in unappropriate data handling however vanished when CMB and deep sample data showed that the right cosmology should be (almost) spatially flat and have a matter density parameter $\Omega_{o,m} \sim 0.25$–0.3 . This does not tell us that cosmic expansion is accelerated, but leaves just the room for a DE unclustered component.

In this thesis I debated the *fine tuning* and the *coincidence* problems that

ΛCDM hardly avoids. Although no present data requires anyting more sophisticated than ΛCDM, it is hard to say that such models "explain" what we measure.

The ideas of a dynamical form of DE, after the discovery of cosmic acceleration, were also revisited. It became however soon evident that tests to discriminate ΛCDM from dDE require the acquisition of fresh data, through dear and highly sophisticated spatial experiments. As a matter of fact, this is the primary scope of theoretical research, motivating new technologies and the building of more and more efficient probes.

While experimental people are then making their plans, theoretical research put forward a number of further options, besides ordinary dDE. We briefly discussed about them, in this thesis.

Among them we should consider quite seriously the possibility that DE is due to a back–reaction of the formation of non–linear inhomogeneities. The coincidence between their growth and the arise of DE is striking and, even though theorists have not been able to give any credible proof of such option, no disproof exists and it must certainly be kept open.

Another kind of option concerns GR modifications, replacing the curvature scalar R, as gravity lagrangian, by a function $f(R)$ which, in ordinary conditions, should be observationally undistinguishable from R itself.

The very nature of these options is however showing which kind of new knowledge future space missions will concern. This is true also if the dDE option is suitable to account for data. A new field and a new interaction are then needed.

The basic aim of new projected missions is to measure in great detail the scale dependence of the expansion rate $H(a)$ and of the growth factor $G(a)$. In our opinion, a basic distinction to be operated among physical options is between those predicting a direct link between $H(a)$ and $G(a)$, *i.e.*, allowing atmost to fit one or a few theory parameters from their comparison, and those allowing for indipendent $H(a)$ and $G(a)$.

GR modifications, *e,g,*, belong to the former cathegory. Coupled DE theories, where the coupling strength may be a function of the DE field ($\beta(\phi)$), belong to the latter one, together with the backreaction option.

In a sense, a cDE theory fitting future data could also be seen as an *effective* description of deeper physics, allowing for independent $H(a)$ and $G(a)$. This very fact, in my opinion, increases the significance of deepening this kind of possibility.

As I showed in this thesis, when the option of a coupling in the Dark sector is opened, there can be a critical fallout in determing cosmological parameters.

In fact, in Chapter 3, I showed that current cosmological limits on neutrino masses are softened by a factor ~ 2, at least, if DM–DE coupling is allowed, thus partially recovering mixed DM models. At the same time, also current limits on DM–DE coupling are looser if ν's masses are slightly greater.

Moreover, in chapter 6, I verified that introducing coupling degrees of free-

dom in an ideal CMB experiment is crucial for the error estimates, even doubling in some cases. These effects are reduced if the WL observable is added, thanks to the complementarity between CMB and WL measurements.

In this conclusive chapter, I wish to add some further evidence, besides of the cases of lensing and neutrino mass, treated in previous chapters. In Table 7.1 I report some results from a work in progress [173]. Artificial CMB data are created with a SUGRA cosmology, considering either $\beta = 0$, $\beta = 0.05$ or $\beta = 0.1$. Standard MCMC are then used to analyse them, assuming DE to have a constant state parameter w. This is not far from what WMAP people did with their data. We do that both for *fiducial* data and for data *realizations*. In Table 7.1, input values for each parameter are compared with the outputs from the fits.

In the case of uncoupled SUGRA there is no real problem. Input data are nicely recovered. On the contrary, when a tiny coupling $\beta = 0.05$, quite consistent with any observational limit, is input, there is a serious fallout on the detectability of other parameters. The most critical case concerns $\omega_{o,c}$. The difference between the input value and the best fit value is 0.0065, approximately 6 % of the parameter value. In the esperiment we mimic, which assumes a "peximistic" PLANCK sensitivity level, the precision attained, in parameter estimates, is however $\mathcal{O}(1\,\%)$, and the above discrepancy is ~ 5 times the estimated standard deviation, in the case of fiducial data; even more than so in some realization. In the case of a stronger coupling $\beta = 0.1$ things are even worst.

This means that a neglect of the coupling option risks to cause inconsistencies in current data analysis. In our opinion, at least a constant coupling option should be left open in data analysis, which were often even too sophisticated in the description of the evolution of the DE state parameter.

The importance of opening such degree of freedom is not necessarely correlated to the actual nature of DE. As already outlined, a cDE theory could be a phaenomenological description for still ununderstood physics, *e.g.*, for a back–reaction picture. But we should not discard the alternative realistic possibility that we are studying real fields, providing a number of their characteristics, so possibly opening the way to fresh lab measures.

Let us then come back to the initial point of this chapter, that cosmological data have led to some of the major discoveries of the physics of the XX century. The meaning of a number of uncontroversial data, as we saw, is still matter of difficult inspections. Theory and experiments are travelling together in opening new ways to human knowledge. In my opinion this is perhaps the most significant fronteer of present research and, I believe, we shall be living in a century when our comprehension of the world where we live can make extraordinary steps forward.

Table 7.1: Results of an MCMC analysis, seeking the parameters listed in the first column, on artificial CMB data built with the parameter values also listed in the first column, but using a SUGRA cosmology, whose Λ and β are shown in the header. For each parameter, the first line yields results for the fiducial case, the next 3 lines for model realizations.

	Input model: *SUGRA* ($\Lambda = 1\,\mathrm{GeV}$) with		
Parameter &	$\beta = 0$	$\beta = 0.05$	$\beta = 0.1$
Input value	Av. value $\pm\sigma$	Av. value $\pm\sigma$	Av. value $\pm\sigma$
$10^2\,\omega_{o,b}$	2.274 ± 0.015	2.274 ± 0.015	2.277 ± 0.017
2.273	2.278 ± 0.015	2.275 ± 0.015	2.295 ± 0.017
	2.278 ± 0.015	2.261 ± 0.015	2.287 ± 0.017
	2.280 ± 0.015	2.278 ± 0.015	2.282 ± 0.017
$\omega_{o,c}$	0.1099 ± 0.0013	0.1164 ± 0.0014	0.1225 ± 0.0016
0.1099	0.1083 ± 0.0013	0.1166 ± 0.0012	0.1225 ± 0.0016
	0.1086 ± 0.0013	0.1171 ± 0.0014	0.1216 ± 0.0016
	0.1104 ± 0.0013	0.1163 ± 0.0014	0.1225 ± 0.0015
$10^2\,\theta$	1.0758 ± 0.0003	1.0736 ± 0.0003	1.0507 ± 0.0003
1.072	1.0759 ± 0.0003	1.0736 ± 0.0003	1.0509 ± 0.0003
	1.0760 ± 0.0003	1.0737 ± 0.0003	1.0507 ± 0.0003
	1.0759 ± 0.0003	1.0736 ± 0.0003	1.0507 ± 0.0003
τ_{opt}	0.088 ± 0.005	0.087 ± 0.005	0.085 ± 0.005
0.087	0.087 ± 0.005	0.903 ± 0.005	0.084 ± 0.005
	0.089 ± 0.005	0.083 ± 0.005	0.087 ± 0.005
	0.093 ± 0.005	0.079 ± 0.005	0.078 ± 0.005
w	$-0.79 - 0.12 + 0.49$	$-0.75 - 0.30 + 0.26$	$-0.85 - 0.43 + 0.38$
—	$-0.84 - 0.27 + 0.25$	$-0.76 - 0.30 + 0.26$	$-0.96 - 0.44 + 0.82$
	$-0.81 - 0.26 + 0.25$	$-0.79 - 0.29 + 0.26$	$-0.67 - 0.34 + 0.37$
	$-0.87 - 0.28 + 0.28$	$-0.54 - 0.15 + 0.16$	$-0.63 - 0.24 + 0.23$
n_s	0.963 ± 0.004	0.962 ± 0.004	0.960 ± 0.004
0.963	0.966 ± 0.004	0.962 ± 0.004	0.958 ± 0.004
	0.968 ± 0.004	0.962 ± 0.004	0.963 ± 0.004
	0.959 ± 0.004	0.961 ± 0.004	0.959 ± 0.004
$\ln(10^{10}\,A_s)$	3.3168 ± 0.0102	3.1695 ± 0.0101	2.8860 ± 0.0101
3.3144 if $\beta = 0$	3.3127 ± 0.0094	3.1699 ± 0.0106	2.8866 ± 0.0099
3.1634 if $\beta = 0.05$	3.3144 ± 0.0103	3.1565 ± 0.0095	2.8885 ± 0.0102
2.8902 if $\beta = 0.10$	3.3310 ± 0.0097	3.1486 ± 0.0105	2.8736 ± 0.0111
$100\,h$	$74.7 - 7.2 + 25.3$	$70.6 - 11.3 + 12.8$	$66.3 - 11.7 + 13.8$
71.9	$77.3 - 12.4 + 13.7$	$71.0 - 11.4 + 12.6$	$70.2 - 20.3 + 14.6$
	$75.7 - 12.3 + 13.3$	$71.9 - 11.0 + 12.6$	$60.9 - 11.1 + 10.5$
	$78.4 - 13.6 + 13.9$	$61.6 - 6.1 + 6.0$	$59.5 - 5.7 + 5.6$
$\Omega_{o,m}$	$0.255-0.084+0.169$	$0.300-0.100+0.095$	$0.360-0.133+0.127$
0.257	$0.235-0.105+0.077$	$0.296-0.096+0.096$	$0.325-0.123+0.140$
	$0.245-0.079+0.077$	$0.289-0.093+0.088$	$0.422-0.138+0.121$
	$0.233-0.101+0.084$	$0.379-0.074+0.073$	$0.431-0.103+0.097$

Acknowledgments

I am grateful to the teaching body of the PhD Course, and in particular to Francesco Miglietta, for allowing me to realize my PhD program.

I would particularly like to thank my supervisor, Silvio Bonometto, for introducing me to the fashinating study of Cosmology and for his precious advices during these three years of work.

My gratitude goes also to Luca Amendola for his constant interest towards my research activity and his useful suggestions.

My thanks go also to Loris Colombo, Roberto Mainini and Luciano Casarini for their friendly and fruitful collaboration.

Appendix A

Methods

In this appendix, we give some technical arguments about the methods used to get the results discussed in the thesis.

A.1 Fisher's formalism

The Fisher matrix formalism [76, 75, 77] provides lower limits to the error bars of the cosmological parameters one wishes to measure. The basic tool in Fisher's method is the likelihood function, yielding the probability that a model gives the set of data $\boldsymbol{x}$.

Suppose we want to test an hypothesis, *i.e.* a cosmological model set by M parameters $\boldsymbol{\theta} = (\theta_1, \theta_2, \ldots \theta_M)$. The likelihood function $L(\boldsymbol{x}|\boldsymbol{\theta}) = \exp[-\mathcal{L}(\boldsymbol{x}|\boldsymbol{\theta})]$ is often a complicated function of $\boldsymbol{\theta}$; the value $\hat{\boldsymbol{\theta}}$ corresponding to the peak of L defines the *maximum likelihood estimator* which, in the limit of large data sets, becomes the *best unbiased estimator* of the actual parameter set. Thus, the likelihood can be Taylor expanded to second order (the first non–vanishing term) around $\hat{\boldsymbol{\theta}}$, being so approximated with a multivariate Gaussian distribution

$$L(\boldsymbol{x}|\boldsymbol{\theta}) \propto \exp\left(-\frac{1}{2}\Delta\boldsymbol{\theta}^T \mathbf{C}(\boldsymbol{\theta})^{-1}\Delta\boldsymbol{\theta}\right) ; \tag{A.1}$$

here

$$\mathbf{C}(\boldsymbol{\theta})^{-1} = \left.\frac{\partial^2 \mathcal{L}(\boldsymbol{x}|\boldsymbol{\theta})}{\partial\theta_\alpha \partial\theta_\beta}\right|_{\boldsymbol{\theta}=\hat{\boldsymbol{\theta}}} \tag{A.2}$$

is a positive semi-definite non-singular matrix, dubbed *covariance matrix* of the θ_α. We remind that equation (A.1) holds just in a sufficiently small neighborhood around the maximum $\hat{\boldsymbol{\theta}}$. In turn, the *Fisher information matrix* reads

$$\mathbf{F}_{\alpha\beta}(\boldsymbol{\theta}) = \left\langle \frac{\partial \mathcal{L}(\boldsymbol{x}|\boldsymbol{\theta})}{\partial \theta_\alpha} \frac{\partial \mathcal{L}(\boldsymbol{x}|\boldsymbol{\theta})}{\partial \theta_\beta} \right\rangle_{\boldsymbol{\theta}=\hat{\boldsymbol{\theta}}} = \left\langle -\frac{\partial^2 \mathcal{L}(\boldsymbol{x}|\boldsymbol{\theta})}{\partial \theta_\alpha \partial \theta_\beta} \right\rangle_{\boldsymbol{\theta}=\hat{\boldsymbol{\theta}}} ; \tag{A.3}$$

the average $\langle \ldots \rangle = \int \mathcal{L}(\boldsymbol{x}|\boldsymbol{\theta}) \ldots d^N \boldsymbol{x}$ is taken over all possible data realizations, given the model parameters. The feature making Fisher's formalism so significant is the Cramér-Rao theorem. It states that the parameter variance about any unbiased estimator value owns a lower bound: $\Delta\theta_\alpha \geq \sqrt{(\mathbf{F}^{-1})_{\alpha\alpha}}$, if the other parameters are estimated from the data as well, $\Delta\theta_\alpha \geq 1/\sqrt{\mathbf{F}_{\alpha\alpha}}$, if all the other parameters are known. Therefore,the Fisher information matrix components are the expectation values of $\mathbf{C}^{-1}(\hat{\boldsymbol{\theta}})$. Accordingly, the inverse of the Fisher matrix is an estimate of the covariance matrix of the parameters $\mathbf{C}(\boldsymbol{\theta}) \approx \mathbf{F}^{-1}$.

A convenient way to re–write the Fisher matrix is computing the derivatives of the likelihood function using the following chain rule [174]:

$$\left.\frac{\partial \mathcal{L}(\boldsymbol{x}|\boldsymbol{\theta})}{\partial \theta_\alpha}\right|_{\boldsymbol{\theta}=\hat{\boldsymbol{\theta}}} = \sum_\ell \left.\frac{\partial \mathcal{L}(\boldsymbol{x}|\boldsymbol{\theta})}{\partial x_\ell}\right|_{\boldsymbol{x}=\boldsymbol{x}(\hat{\boldsymbol{\theta}})} \left.\frac{\partial x_\ell}{\partial \theta_\alpha}\right|_{\boldsymbol{\theta}=\hat{\boldsymbol{\theta}}} \tag{A.4}$$

Thus, the Fisher matrix (A.3) can be expressed as:

$$\begin{aligned}
\mathbf{F}_{\alpha\beta}(\boldsymbol{\theta}) &= \sum_{\ell\ell'} \frac{\partial x_\ell}{\partial \theta_\alpha} \frac{\partial x_{\ell'}}{\partial \theta_\beta} \left\langle -\frac{\partial^2 \mathcal{L}(\boldsymbol{x}|\boldsymbol{\theta})}{\partial x_\ell \partial x_{\ell'}} \right\rangle_{\boldsymbol{x}=\boldsymbol{x}(\hat{\boldsymbol{\theta}})} && \text{(A.5)} \\
&= \sum_{\ell\ell'} \frac{\partial x_\ell}{\partial \theta_\alpha} \mathbf{F}_{\ell\ell'}(\boldsymbol{\theta}) \frac{\partial x_{\ell'}}{\partial \theta_\beta} && \text{(A.6)} \\
&\approx \sum_{\ell\ell'} \frac{\partial x_\ell}{\partial \theta_\alpha} \mathbf{C}^{-1}_{\ell\ell'}(\boldsymbol{\theta}) \frac{\partial x_{\ell'}}{\partial \theta_\beta}, && \text{(A.7)}
\end{aligned}$$

where $\mathbf{F}_{\ell\ell'}$ and $\mathbf{C}_{\ell\ell'}$, respectively, are the Fisher and the covariance matrix for the observables $\boldsymbol{x}$. The region in the M–dimensional space of the parameters, defined by $Q(\theta, \hat{\theta}) = \Delta\theta_\alpha^T \mathbf{F}_{\alpha\beta} \Delta\theta_\beta = K^2$, is a hyper–ellipsoid of constant probability density for the function (A.1). Marginalizing over the other parameters, one can project this ellipsoid in the two–parameter subspace, yielding a two–dimensional ellipse. The analytical expression for the projected ellipse for the

two parameters θ_α and θ_β is given by [175]:

$$\left(\begin{array}{cc} \Delta\theta_\alpha & \Delta\theta_\beta \end{array} \right) \left[\begin{array}{cc} (\mathbf{F}^{-1})_{\alpha\alpha} & (\mathbf{F}^{-1})_{\alpha\beta} \\ (\mathbf{F}^{-1})_{\alpha\beta} & (\mathbf{F}^{-1})_{\beta\beta} \end{array} \right]^{-1} \left(\begin{array}{c} \Delta\theta_\alpha \\ \Delta\theta_\beta \end{array} \right) = \Delta\chi^2(N=2,\sigma) \quad \text{(A.8)}$$

This can be interpreted as an estimate of the confidence region within a given confidence level σ for the two parameters θ_α and θ_β.

A.2 Convergence power spectrum covariance

In order to determine the convergence power spectrum covariance, one can introduce the so called "flat-sky" approximation and treat the sky as flat, replacing spherical harmonic sums with Fourier transforms (FT). Of course, this approximation is acceptable just for small angular scales We also consider the tomographic case and use Greek letters as superscripts to denote quantities belonging to different redshift bins. The FT of the convergence field can be defined as:

$$\kappa^\alpha(\mathbf{l}) = \int \mathrm{d}^2\boldsymbol{\theta}\, \kappa^\alpha(\boldsymbol{\theta}) \exp(-i\boldsymbol{\theta}\cdot\mathbf{l}), \quad \text{(A.9)}$$

while the convergence power spectrum and trispectrum are, respectively:

$$\langle \kappa^\alpha(\mathbf{l}_1)\, \kappa^\beta(\mathbf{l}_2)\rangle = (2\pi)^2\, \delta_D(\mathbf{l}_1+\mathbf{l}_2)\, P_{l_1}^{\alpha\beta}, \quad \text{(A.10)}$$

$$\langle \kappa^\alpha(\mathbf{l}_1)\ldots\kappa^\delta(\mathbf{l}_4)\rangle_c = (2\pi)^2\, \delta_D(\mathbf{l}_1+\ldots+\mathbf{l}_4)\, T^{\alpha\beta\gamma\delta}(\mathbf{l}_1,\mathbf{l}_2,\mathbf{l}_3,\mathbf{l}_4)\,; \quad \text{(A.11)}$$

here δ_D is the Dirac function. The value of the lensing power spectrum in correspondence of a multipole l can be estimated as the mean over a multipole bin of width Δl, centered at l:

$$\mathcal{P}_l^{\alpha\beta} = \frac{1}{A}\int_{s_l} \frac{\mathrm{d}^2\mathbf{l}_1}{A_l} \kappa^\alpha(\mathbf{l}_1)\, \kappa^\beta(-\mathbf{l}_1)\,, \quad \text{(A.12)}$$

where $A_l = \int_{s_l} \mathrm{d}^2\mathbf{l} \cong 2\pi l\, \Delta l$ is the area of the shell of width Δl corresponding to l, while $A = 4\pi f_{sky}$ is the area of the survey. Quite in the same way, for the trispectrum we have:

$$\mathcal{T}_{ll'}^{\alpha\beta\gamma\delta} = \int_{s_l} \frac{\mathrm{d}^2\mathbf{l}_1}{A_l} \int_{s_{l'}} \frac{\mathrm{d}^2\mathbf{l}_2}{A_{l'}} T^{\alpha\beta\gamma\delta}(\mathbf{l}_1,-\mathbf{l}_1,\mathbf{l}_2,-\mathbf{l}_2)\,. \quad \text{(A.13)}$$

Let us then consider the following expression:

$$\langle \mathcal{P}_l^{\alpha\beta} \mathcal{P}_{l'}^{\gamma\delta} \rangle = \frac{1}{A^2} \int_{s_l} \frac{\mathrm{d}^2\mathbf{l}_1}{A_l} \int_{s_{l'}} \frac{\mathrm{d}^2\mathbf{l}_2}{A_{l'}} \langle \kappa^\alpha(\mathbf{l}_1)\, \kappa^\beta(-\mathbf{l}_1)\, \kappa^\gamma(\mathbf{l}_2)\, \kappa^\delta(-\mathbf{l}_2) \rangle. \quad \text{(A.14)}$$

The 4-point function at the r.h.s. can be decomposed in its connected parts:

$$\begin{aligned} \langle \kappa^\alpha(\mathbf{l}_1)\, \kappa^\beta(-\mathbf{l}_1)\, \kappa^\gamma(\mathbf{l}_2)\, \kappa^\delta(-\mathbf{l}_2) \rangle &= \langle \kappa^\alpha(\mathbf{l}_1)\, \kappa^\beta(-\mathbf{l}_1)\, \kappa^\gamma(\mathbf{l}_2)\, \kappa^\delta(-\mathbf{l}_2) \rangle_c + \\ &+ \langle \kappa^\alpha(\mathbf{l}_1)\, \kappa^\beta(-\mathbf{l}_1) \rangle \langle \kappa^\gamma(\mathbf{l}_2)\, \kappa^\delta(-\mathbf{l}_2) \rangle + \\ &+ \langle \kappa^\alpha(\mathbf{l}_1)\, \kappa^\gamma(\mathbf{l}_2) \rangle \langle \kappa^\beta(-\mathbf{l}_1)\, \kappa^\delta(-\mathbf{l}_2) \rangle + \langle \kappa^\alpha(\mathbf{l}_1)\, \kappa^\delta(-\mathbf{l}_2) \rangle \langle \kappa^\gamma(\mathbf{l}_2)\, \kappa^\beta(-\mathbf{l}_1) \rangle, \end{aligned} \quad \text{(A.15)}$$

Replacing their expression in eq. (A.14), one can easily recognize the contribution of the trispectrum, using eq. (A.11):

$$\begin{aligned} \langle \mathcal{P}_l^{\alpha\beta} \mathcal{P}_{l'}^{\gamma\delta} \rangle &= \frac{1}{A^2} \int_{s_l} \frac{\mathrm{d}^2\mathbf{l}_1}{A_l} \int_{s_{l'}} \frac{\mathrm{d}^2\mathbf{l}_2}{A_{l'}} (2\pi)^2\, \delta_D(\mathbf{0})\, T^{\alpha\beta\gamma\delta}(\mathbf{l}_1, -\mathbf{l}_1, \mathbf{l}_2, -\mathbf{l}_2) + \langle \mathcal{P}_l^{\alpha\beta} \rangle \langle \mathcal{P}_{l'}^{\gamma\delta} \rangle + \\ &+ \frac{1}{A^2} \int_{s_l} \frac{\mathrm{d}^2\mathbf{l}_1}{A_l} \int_{s_{l'}} \frac{\mathrm{d}^2\mathbf{l}_2}{A_{l'}} \langle \kappa^\alpha(\mathbf{l}_1)\, \kappa^\gamma(\mathbf{l}_2) \rangle \langle \kappa^\beta(-\mathbf{l}_1)\, \kappa^\delta(-\mathbf{l}_2) \rangle + \quad \text{(A.16)} \\ &+ \frac{1}{A^2} \int_{s_l} \frac{\mathrm{d}^2\mathbf{l}_1}{A_l} \int_{s_{l'}} \frac{\mathrm{d}^2\mathbf{l}_2}{A_{l'}} \langle \kappa^\alpha(\mathbf{l}_1)\, \kappa^\delta(-\mathbf{l}_2) \rangle \langle \kappa^\gamma(\mathbf{l}_2)\, \kappa^\beta(-\mathbf{l}_1) \rangle, \quad \text{(A.17)} \end{aligned}$$

where $(2\pi)^2\, \delta_D(\mathbf{0}) = A$. Owing to the definition of covariance,

$$\mathrm{Cov}\left[\mathcal{P}_l^{\alpha\beta}, \mathcal{P}_{l'}^{\gamma\delta} \right] \equiv \langle \mathcal{P}_l^{\alpha\beta} \mathcal{P}_{l'}^{\gamma\delta} \rangle - \langle \mathcal{P}_l^{\alpha\beta} \rangle \langle \mathcal{P}_{l'}^{\gamma\delta} \rangle, \quad \text{(A.18)}$$

and using (A.10), one can then argue that the integrals in (A.16) make sense only if they correspond to the same l–bin; the same can be claimed for (A.17). This property can be described introducing a Kronecker delta function $\delta_{ll'}$. Thus, the expression (A.18) becomes:

$$\begin{aligned} \mathrm{Cov}\left[\mathcal{P}_l^{\alpha\beta}, \mathcal{P}_{l'}^{\gamma\delta} \right] &= \frac{1}{A} \mathcal{T}_{ll'}^{\alpha\beta\gamma\delta} + \delta_{ll'} \frac{(2\pi)^2}{A^2} \int_{s_l} \frac{\mathrm{d}^2\mathbf{l}_1}{A_l^2} \left[P_{l_1}^{\alpha\gamma} \langle \kappa^\beta(-\mathbf{l}_1)\, \kappa^\delta(\mathbf{l}_1) \rangle + \right. \\ &\left. + P_{l_1}^{\alpha\delta} \langle \kappa^\gamma(\mathbf{l}_1)\, \kappa^\beta(-\mathbf{l}_1) \rangle \right] \\ &= \frac{1}{A} \mathcal{T}_{ll'}^{\alpha\beta\gamma\delta} + \delta_{ll'} \frac{(2\pi)^2}{A A_{s_l}} \int_{s_l} \frac{\mathrm{d}^2\mathbf{l}_1}{A_{s_l}} \left[P_{l_1}^{\alpha\gamma} P_{l_1}^{\beta\delta} + P_{l_1}^{\alpha\delta} P_{l_1}^{\gamma\beta} \right] \quad \text{(A.19)} \\ &\approx \frac{1}{4\pi\, f_{sky}} \mathcal{T}_{ll'}^{\alpha\beta\gamma\delta} + \frac{\delta_{ll'}}{2 l \Delta l f_{sky}} \left[P_l^{\alpha\gamma} P_l^{\beta\delta} + P_l^{\alpha\delta} P_l^{\gamma\beta} \right]. \quad \text{(A.20)} \end{aligned}$$

In the last line, we have supposed the lensing power spectrum to be smooth enough to treat it as a constant within each bin width.

Bibliography

[1] E. P. Hubble (1929), Astrophysical Journal, **69**, 103

[2] Issue 1860, New Scientist magazine, 1993, page 22

[3] E. Komatsu *et al.* [WMAP Collaboration], arXiv:0803.0547 [astro-ph].

[4] D.J. Bacon, A. Refregier, R. Ellis, *MNRAS*,**318**,(2000),625.

[5] D.J. Bacon, R. Massey, A. Refregier, R. Ellis, *MNRAS*,**344**,(2003),673.

[6] M. Brown, A.N. Taylor, D.J. Bacon, M.E. Gray, S. Dye, K. Meisenheimer, C. Wolf, *MNRAS*,**341**,(2003),100.

[7] T. Hamana, S. Miyazaki, K. Shimasaku, H. Furusawa, M. Doi, et al., *ApJ*,**597**,(2003),98.

[8] H. Hämmerle, J.M. Miralles, P. Schneider, T. Erben, R.A. Fosbury, *A&A*,**385**,(2002),743.

[9] H. Hoekstra, H.K.C. Yee, M. Gladders, *ApJ*,**577**,(2002),595.

[10] H. Hoekstra, H.K.C. Yee, M. Gladders, L. Felipe Barrientos, P.B. Hall, L. Infante, *ApJ*,**572**,(2002),55.

[11] M. Jarvis, G.M. Bernstein, P. Fisher, D. Smith, B. Jain, J.A. Tyson, D. Wittman, *ApJ*,**125**,(2002),1014.

[12] N. Kaiser, G. Wilson, G.A. Luppino, (2000), arXiv:astro-ph/0003338

[13] R. Maoli, L. van Waerbeke, Y. Mellier, P. Schneider, B. Jain, et al., *A&A*,**368**,(2001),766.

[14] A. Refregier, J. Rhodes, E. Groth, *ApJ*,**572**,(2002),L131.

[15] J. Rhodes, A. Refregier, E. Groth, *ApJ*,**552**,(2001),L85.

[16] L. van Waerbeke, Y. Mellier, M. Radovich, E. Bertin, M. Dantel-Fort, et al., *A&A*,**374**,(2001),757.

[17] L. van Waerbeke, Y. Mellier, R. Pelló, U.-L. Pen, H.J. McCracken, B. Jain, *A&A*,**393**,(2002),369.

[18] D.M. Wittman, J. Tyson, D. Kirkman, I. Dell'Antonio, G. Bernstein, *Nature*,**405**,(2000),143.

[19] Eisenstein D J Hu W and Tegmark M 1999 *Astrophys. J.* **518** 2

[20] Bartelmann M and Schneider P 2001 Phys.Rept. **340** 291

[21] Refregier A *Ann. Rev. Astron. Astrophys.* 2003 **41** 645

[22] Van Waerbeke L and Mellier Y *Preprint* astro-ph/0305089

[23] Schneider P *Preprint* astro-ph/0509252

[24] J.C. Mather *et al.* 1999,*Astrophys. J.* **512** 511

[25] G. Gamow, 1948, *Nature* **162** 680

[26] G. Steigman, D. N. Schramm, J. Gunn 1977, *Phys. Lett.* B **66**, 202

[27] de Bernardis P, Ade P A R, Bock J J, et al. 2000 *Nature* **404** 955

[28] Hanany S, Ade P., Balbi A. et al., 2000, ApJ, 545, L5

[29] Halverson, N.W. *et al.*, 2002, ApJ 568 38

[30] Percival W.J., Baugh C.M., Bland-Hawthorn J. et al., 2001, MNRAS, 327, 1297

[31] Netterfield C.B. et al. (Boomerang Collaboration), 2002, ApJ 571 604

[32] D.N. Spergel, L. Verde, H.V. Peiris, et al. *ApJ Suppl. Series*, 148:175, 2003.

[33] Tegmark M., Strauss, Blanton M., et al., 2004, Phys.Rev. D69, 103501

[34] Padin S, Cartwright J K, Mason B S, et al. 2001 *Astrophys. J.* **549** L1; Kovac J, Leitch E M, Pryke C, et al. 2002 *Nature* **420** 772; Scott P F, Carreira P, Cleary K, et al. 2003 *Mon. Not. R. Aston. Soc.* **341** 1076; Spergel D N, Bean R, Dorè et al. 2007 *Astrophys. J.* **170** 377 *Preprint* astro–ph/0603449

[35] Colless M M, Dalton G B, Maddox S J, et al. 2001 *Mon. Not. R. Aston. Soc.* **329** 1039; Colless M M, Peterson B A, Jackson C, et al. 2003 *Preprint* astro–ph/0306581; Loveday J (the SDSS collaboration) 2002 *Contemporary Phys.* **43** 437; Tegmark M, Blanton M, Strauss M et al. 2004 *Astrophys. J.* **606** 702–740; Adelman–McCarthy J K, Agueros M A, Allam S S, et al. 2006 *Astrophys. J. Suppl.* **162** 38–48

[36] Riess A G, Kirshner R P, Schmidt B P, Jha S, et al. 1998 *Astrophys. J.* **116** 1009

[37] Perlmutter S, Aldering G, Goldhaber G, et al. 1999 *Astrophys. J.* **517** 565

[38] Riess A G, Strolger L-G, Tonry J, et al. 2004 *Astrophys. J.* **607** 665

[39] Kolb E.W., Matarrese S. & Riotto A., 2005, astro-ph/0506534

[40] Kolb E.W., Matarrese S., Notari A. & Riotto A., 2005, Phys.Rev., D71, 023524

[41] Buchert T., 2000, Gen.Rel.Grav., 32, 105

[42] Buchert T., Kerscher M. & Sicka C., 2000, Phys.Rev., D62, 043525

[43] Ratra B. & Peebles P. J., 1988, Phys.Rev., D37, 3406

[44] Brax P and Martin J 1999 *Phys. Lett.* B**468** 40

[45] Ferreira, P.G. & Joyce M., 1998, Phys.Rev., D58, 023503

[46] Barreiro J., Copeland P. & Nunes F.G., 2000, Phys.Rev., D61, 127301

[47] Kim J.E., 1999, JHEP, 9905, 022

[48] Albrecht L. & Skordis R., 2000, Phys.Rev.Lett., 84, 2076

[49] Sahni L. & Wang, H., 2000, Phys.Rev., D62, 103517

[50] Brax P, Martin J and Riazuelo A 2000 *Phys. Rev.* D**62** 103505

[51] Brax P and Martin J 2000 *Phys. Rev.* D**61** 103502

[52] Amendola L., 1999, Phys.Rev., D60, 043501

[53] Damour T., Gibbons G. W. & Gundlach C., 1990, Phys.Rev., L64, 123D

[54] Damour T. & Gundlach C., 1991, Phys.Rev., D43, 3873

[55] Wetterich C., 1998, Nucl. Phys. B 302, 668

[56] Amendola L., 2000, Phys.Rev., D62, 043511

[57] Holden D.J. & Wands D., 2000, Phys.Rev., D61, 043506

[58] Gasperini M., Piazza F. & Veneziano G., 2002, Phys.Rev., D65, 023508

[59] Wetterich C., 1995, A&A 301, 321

[60] Rhodes C.S, van de Bruck C., Brax P. & Davis A.C., 2003, Phys.Rev., D68, 083511

[61] La Vacca, S. A. Bonometto and L. P. L. Colombo, arXiv:0810.0127 [astro-ph], submitted to New Astronomy

[62] Q. R.Ahmad et al., Physical Review Letters **89**, 011301 (2002); S. N.Ahmed et al., Physical Review Letters **92**, 181301 (2004).

[63] K. Eguchi et al., Physical Review Letters **90**, 021802h (2003); T. Araki et al., Physical Review Letters **94**, 081801 (2005).

[64] W. W. Allison et al., Physical Letters B**449**, 137 (1999); M. Ambrosio et al., Physical Letters B**517**, 59 (2001).

[65] M. H. Ahn et al., Physical Review Letters **90**, 041801h (2003); D. G. Michael et al., Physical Review Letters **97**, 191801 (2006).

[66] R. Valdarnini and S. Bonometto, Astronomy and Astrophysics **146**, 2 235 (1985); R. Valdarnini and S. Bonometto, Astrophysical Journal **299**, L71 (1985).

[67] A. G. Riess, R. P. Kirshner, B. P. Schmidt, S. Jha, et al., Astrophysical Journal **116**, 1009 (1998); S. Perlmutter, G. Aldering, G. Goldhaber, et al., Astrophysical Journal **517**, 565 (1999); A. G. Riess, L.G. Strolger, J. Tonry, et al., Astrophysical Journal **607**, 665 (2004).

[68] P. de Bernardis, P. Ade, J. Bock, et al., Nature **404**, 955 (2000); S. Padin, J. Cartwright, B. Mason, et al., Astrophysical Journal **549**, L1 (2001); J. Kovac, E. Leitch, c. Pryke, et al., Nature **420**, 772 (2002); P. Scott, P. Carreira, K. Cleary, et al., Monthly Notices of the Royal Astronomical Society **341**, 1076 (2003); D. Spergel, R. Bean, Dorè et al., Astrophysical Journal Preprint astro–ph/0603449

[69] M. Colless, G. Dalton, S. Maddox, et al., Monthly Notices of the Royal Astronomical Society **329**, 1039 (2001); M. Colless, B. Peterson, C. Jackson, et al., Preprint astro–ph/0306581; J. Loveday (the SDSS collaboration), Contemporary Physics **43**, 437 (2002); M. Tegmark, M. Blanton, M. Strauss et al., Astrophysical Journal **606**, 702 (2004); J. Adelman–McCarthy, M. Agueros, S. Allam, et al., Astrophysical Journal Supplement **162**, 38 (2004).

[70] A. Dolgov, Physical Report, **370**, 333 (2002); O. Elgaroy and O. Lahav, New Journal of Physics **7**, 61t (2005); J. Lesgourgues and S. Pastor, Physical Report **429**, 307 (2006).

[71] E. Komatsu et al. [WMAP Collaboration], Preprint arXiv:0803.0547 [astro-ph].

[72] A. Goobar, S. Hannestad, E. Mortsell and H. Tu, JCAP **0606**, 019 (2006); A. G. Sanchez and S. Cole, MNRAS, **385**, 830 (2008).

[73] J. Lesgourgues, M. Viel, M. G. Haehnelt and R. Massey, JCAP **0711**, 008 (2007): J. S. Bolton, M. Viel, T. Kim, M. G. Haehnelt, & R. F. Carswell, MNRAS, **386**, 1131 (2008).

[74] S. Hannestad, Phys. Rev. Lett. **95**, 221301 (2005).

[75] Fisher R A 1935 *J. Roy. Statist. Soc.* **98** 39

[76] Sivia D S 1996 *Data analysis: A Bayesian Tutorial* (Oxford: Oxford University Press)

[77] Tegmark M, Taylor A and Heavens A 1997 *Astrophys. J.* **480** 22

[78] M. C. Neyrinck and I. Szapudi, 2007, MNRAS, **375**, L51

[79] R. Scoccimarro, M. Zaldarriaga & L. Hui, 1999, ApJ,**527**, 1

[80] A. J. S. Hamilton, C. D. Rimes & R. Scoccimarro, 2006 MNRAS,**371**, 1188

[81] A. Einstein *Sitzungsber. preuss. Akad. Wiss.*, 831, 1915.

[82] F.W. Dyson, A.S. Eddington, C. Davidson *Phil. Trans. Roy. Soc.*, 220A, 291, 1920.

[83] Schneider, P., Ehlers, J., & Falco, E.E. *Gravitational Lenses* (Berlin: Springer Verlag), 1992.

[84] R. Narayan and R.D. Blandford, *Ann. NY. Acad. Sci.*,**647**,(1991),.

[85] L. L. R. Williams and P. L. Schechter, Measurement of the Hubble Constant Via Gravitational Lensing— A Review of the Jodrell Bank "Golden Lenses" Workshop, arXiv:astro-ph/9709059.

[86] N. Kaiser, G. Squires, *ApJ*,**404**,(1993),441.

[87] P. Schneider, *Gravitational Lensing: Strong, Weak and Micro*, Lecture Notes of the 33rd Saas-Fee Advanced Course, G. Meylan, P. Jetzer & P. North (eds.), Springer-Verlag: Berlin, (2006), p.273, arXiv:astro-ph/0509252

[88] J. Miralda-Escude, *ApJ*,**380**,(1991),1.

[89] Y. Mellier, *ARA&A*,**37**,(1999),127.

[90] M. Bartelmann, P. Schneider, *Phys. Rep.*,**340**,(2001),291.

[91] A. Refregier, *ARA&A*,**41**,(2003),645.

[92] L. van Waerbeke, Y. Mellier, (2003), arXiv:astro-ph/0305089.

[93] Y. Mellier, G. Meylan, (eds), *Impact of Gravitational Lensing on Cosmology*, IAU S225, Cambridge university press, (2004)

[94] N. Kaiser, *ApJ*,**439**,(1995),L1.

[95] P. Schneider, *A&A*,**408**,(2003),829.

[96] Smith R E, et al. 2003 *Mon. Not. R. Aston. Soc.* **341** 1311

[97] Bacon, D. J., Réfrégier, A., & Ellis, R. 2000, MNRAS, 318, 625

[98] Kaiser N, Wilson G, Luppino GA arXiv:astro-ph/0003338 (2000)

[99] van Waerbeke, L., Mellier, Y., Erben, T., et al. 2000, A&A, 358, 30

[100] Wittman, D. M., Tyson, J., Kirkman, D., Dell'Antonio, I., & Bernstein, G. 2000, Nature, 405, 143

[101] Maoli, R., van Waerbeke, L., Mellier, Y., et al. 2001, A&A, 368, 766

[102] Van Waerbeke, L., Mellier, Y., Radovich, M., et al. 2001, A&A, 374, 757

[103] Van Waerbeke, L., Mellier, Y., Pelló, R., et al. 2002, A&A, 393, 369

[104] Hamana, T., Miyazaki, S., Shimasaku, K., et al. 2003, ApJ, 597, 98

[105] Hoekstra, H., Yee, H. K. C., & Gladders, M. D. 2002, ApJ, 577, 595

[106] Hoekstra, H., Yee, H. K. C., & Gladders, M. D. 2002b, ApJ, 577, 595

[107] Taylor A.N., 2001, arXiv:astro-ph/0111605

[108] D.J. Bacon, A.N. Taylor, 2003, MNRAS, 344, 1307

[109] W. Hu, C. Keeton, *Phys. Rev. D*,**66**,(2003),3506.

[110] W. Hu, *ApJ*,**522**,(1999),21.

[111] W. Hu, *Phys. Rev. D*,**62**,(2000),3007.

[112] Huterer D 2002 *Phys. Rev.* D **65** 063001

[113] B. Jain, A. N. Taylor, *Phys. Rev. Lett.* 2003911302

[114] Hu W and Jain B 2004 *Phys. Rev.* D **70** 043009

[115] G. Bernstein, B. Jain, *ApJ*,**600**,(2004),17.

[116] J. Zhang, L. Hui, A. Stebbins, *ApJ*,**635**,(2005),806.

[117] A.F. Heavens, *MNRAS*,**343**,(2003),1327.

[118] P.G. Castro, A.F. Heavens, T.D. Kitching, *Phys. Rev. D*,**72**,(2005),3516.

[119] A.F. Heavens, T.D. Kitching, A.N. Taylor, *MNRAS*,,(2006),., in press, arXiv:astro-ph/0606568.

[120] Ma Z M, Hu W and Huterer D 2005 *Astrophys. J.* **636** 21

[121] Kaiser N 1998 *Astrophys. J.* **498** 26

[122] M. Zaldarriaga and U. Seljak. *Phys. Rev. D*, 55:1830, 1997.

[123] U. Seljak and M. Zaldarriaga. *Phys. Rev. Lett.*, 78:2054, 1997. *Phys. Rev. Lett.*, 78:2054, 1997.

[124] M. Kamionkowski, A. Kosowsky, and A. Stebbins. *Phys. Rev. D*, 55:7368, 1997.

[125] E.F. Bunn. *Phys. Rev. D*, 65:043003, 2002.

[126] N. Turok A. Lewis, A. Challinor. *Phys. Rev. D*, 65:023505, 2002.

[127] E.F. Bunn, M. Zaldarriaga, M. Tegmark, and A. de Oliveira-Costa. *Phys. Rev. D*, 67:023501, 2003.

[128] M. Kamionkowski and A. Loeb. *Phys. Rev. D*, 56:4511, 1997.

[129] N. Seto and M. Sasaki. *Phys. Rev. D*, 62:123004, 2000.

[130] C. Skordis and J. Silk. astro-ph/0402744, 2004.

[131] C. Ma and E. Bertschinger. *ApJ*, 455:7, 1995.

[132] L. Knox and M.S. Turner. *Phys. Rev. Lett.*, 73:3347, 1996.

[133] S. Dodelson, L. Knox, and E.W. Kolb. *Phys. Rev. Lett.*, 72:3443, 1994.

[134] U. Seljak and M. Zaldarriaga. *ApJ*, 469:437, 1996.

[135] A. Lewis, A. Challinor, and A. Lasenby. *ApJ*, 538:473, 2000.

[136] R.K. Sachs and A.M. Wolfe. *ApJ*, 147:73, 1967.

[137] W. Hu and N. Sugiyama. *ApJ*, 471:542, 1996.

[138] M. Bucher, K. Moodley, and N. Turok. *Phys. Rev. D*, 62:083508, 1999.

[139] R.A. Sunyaev and Ya.B. Zel'dovich. *Comm. Astrophys. Space Phys*, 4:173, 1969.

[140] A. Kosowsky. *Annals. Phys*, 246:49, 1996.

[141] P. Cabella and M. Kamionkowski. *Lectures given at the 2003 Villa Mondragone School of Gravitation and Cosmology: The Polarization of the Cosmic Microwave Background, Rome, Italy, September 6–11, 2003*, 2004.

[142] M. Zaldarriaga and D.D. Harari. *Phys. Rev. D*, 52:3276, 1995.

[143] W. Hu, M.H. Hedman, and M. Zaldarriaga. *Phys. Rev. D*, 67:043004, 2003.

[144] H.V. Peiris, E. Komatsu, L. Verde, et al. *ApJ Suppl. Series*, 148:213, 2003.

[145] W.H. Kinney. *Phys. Rev. D*, 58:123506, 1998.

[146] M. Zaldarriaga and U. Seljak. *Phys. Rev. D*, 58:023003, 1998.

[147] G. La Vacca and L. P. L. Colombo, 2008, JCAP **0804**, 007

[148] Caldwell R R, Dave R and Steinhardt P J 1998 *Phys. Rev. Lett.* **80** 1582; Wetterich C 1988 *Nucl. Phys.* B**302** 668

[149] Zlatev I, Wang L and Steinhardt P J 1999 *Phys. Rev. Lett.* **82** 896–899; Steinhardt P J, Wang L and Zlatev I 1999 *Phys. Rev.* D**59** 123504

[150] Schimd C et al A&A **463** (2007) 405 Colombo L P L and Gervasi M JCAP **10** (2006) 001

[151] Ellis J., Kalara S., Olive K.A. & Wetterich C., 1989, Phys. Lett. B228, 264; Comelli, D. Pietroni M. amd Riotto, Phys. Lett. B **571** (2003) 115; Chimento L.P., Jakubi A.S., Pavon D. & Zimdahl W.,2003, Phys.Rev D67, 083513 Guo Z K, Ohta N and Tsujikawa S 2007 Phys. Rev. D **76** 023508; Abdalla E, Abramo L R W, Sodre L J and Wang B *Preprint* arXiv:0710.1198 [astro-ph]; Manera M and Mota D F 2006 *Mon. Not. R. Aston. Soc.* **371** 1373

[152] J. Khoury and A. Weltman , Phys.Rev.Lett. **93** (2004) 17110; S.S. Gubser and J.Khoury, Phys.Rev.D **70** (2004) 104001; P. Brax et al., Phys.Rev.D **70** (2004) 123518

[153] Majerotto E, Sapone D and Amendola L (200) astro-ph/0410543 Amendola L, Campos G.C. and Rosenfeld R (2006) astro-ph/0610806

[154] Wei H and Zhang S N 2006 Phys. Lett. B**644** 7 Wei H and Zhang S N 2007 Phys. Lett. B**654** 139 *Preprint* astro-ph/0704.3330

[155] Mainini R, Colombo L P L and Bonometto S A *Astrophys. J.* **632** (2005) 691

[156] Di Porto C and Amendola L (2007) astro-ph/0707.2686

[157] M. Doran, J. Jaeckel, Phys.Rev. D **66** (2002) 043519; Amendola L, Quartin M, Tsujikawa S, and Waga I, Phys.Rev. D **74** (2006) 023525

[158] Amendola L Phys.Rev. D **69** (2004) 103524

[159] Huey G and Wandelt B D Phys.Rev. D **74** (2006) 023519; Das S, Corasaniti P S and Khoury J, Phys.Rev. D **73** (2006) 083509

[160] Amendola L and Quercellini C Phys.Rev. D**68** (2003) 023514 Olivares G, Atrio-Barandela F and Pavon D (2007) astro-ph/0706.3860

[161] Das S, Corasaniti P S and Khoury J Phys.Rev. D**73** (2006) 083509

[162] Mainini R and Bonometto S A JCAP (2007) astro-ph/0703303

[163] Mainini R Phys.Rev.D 72 (2005) 083514

[164] Amendola L, Kunz M and Sapone D (2007) astro-ph/0704.2421

[165] Refregier A et al. *Preprint* astro-ph/0610062

[166] Amara A and Refregier A *Preprint* astro-ph/0610127

[167] Rudd D H, Zentner A R and Kravtsov A V *Preprint* astro-ph/0703741. Zentner A R, Rudd D H and Hu W 2008 *Phys. Rev.* D **77** 043507

[168] Cooray A and Hu W 2001*Astrophys. J.* **554** 56

[169] Takada M and Jain B 2004 *Mon. Not. R. Aston. Soc.* **348** 897

[170] Mainini R 2005 *Phys. Rev.* D **72** 083514

[171] Maccio A V Quercellini C Mainini R Amendola L and Bonometto S A 2004 *Phys. Rev.* D **69** 123516

[172] Ma Z M *Preprint* arXiv:astro-ph/0610213.

[173] L. Vergani, L. P. L. Colombo, G. La Vacca and S. A. Bonometto, submitted to APJ [arXiv:0804.0285 [astro-ph]]

[174] Oh S P, Spergel D N and Hinshaw G 1999 *Astrophys. J.* **510** 551

[175] Matsubara T and Szalay A S *Preprint* astro-ph/0203358.

Ringrazio sentitamente Silvio per tutto quello che mi ha insegnato in questi anni e per i suoi consigli (scientifici e non). Un ringraziamento particolare va anche a Luciano, per le nostre chiacchierate sul Senso Religioso della Vita, e a Loris e Roberto, per quello che ho imparato lavorando con loro.

Ringrazio di cuore i miei genitori che con il loro esempio rappresentano per me un punto di riferimento in ogni circostanza. Insieme a Vincenzo & Raffy ed il piccolo Luca (ad oggi ancora nella pancia di sua mamma), mi siete sempre vicino, dandomi coraggio nelle mie scelte.

Dominga, mio caro amore, ti ringrazio per tutta la pazienza che in questi anni hai avuto nei miei confronti. Io spero, anzi, sono certo, che presto tutti i nostri sacrifici avranno il desiderato compimento.

Ringrazio, infine, tutti gli amici che in questi anni mi hanno sostenuto nella nuova vita milanese: Loredana, Sara, Marta & Dario e le loro ragazze.